université
PARIS-SACLAY

Thèse de doctorat

Search of the $0\nu\beta\beta$ decay with the SuperNEMO demonstrator

Thèse de doctorat de l'Université Paris-Saclay
préparée à l'Université Paris Saclay au sein du Laboratoire Irène-Joliot Curie
(anciennement Laboratoire de l'Accélérateur Linéaire)

École doctorale n°576 Particles, Hadrons, Energy, Nuclei, Instrumentation,
Imaging, Cosmos et Simulation (PHENIICS)
Spécialité de doctorat : Physique des particules

Thèse présentée et soutenue à Orsay, le ***, par

CLOÉ GIRARD-CARILLO

Composition du Jury :

***
***   Président

***
***   Rapporteur

***
***   Rapporteur

Christine Marquet
CENBG - Bordeaux-Gradignan   Examinateur

***
***   Examinateur

***
***   Examinateur

Laurent Simard
LAL - Orsay   Directeur de thèse

Mathieu Bongrand
LAL - Orsay   Co-directeur de thèse

Contents

Introduction

Phenomenology of particle physics

1.1 The Standard Model of particle physics

1.1.1 Bosons

1.1.2 Fermions

1.1.3 $2\nu\beta\beta$ decay

1.1.4 Where the Standard Model ends

1.2 Going beyond the Standard Model with neutrinos

1.2.1 Neutrino flavors and oscillations

1.2.2 Neutrino masses and nature

1.2.3 Other searches beyond the Standard Model with neutrinos

1.3 $0\nu\beta\beta$ experiment status

1.3.1 Experimental design criteria

As no neutrinos are emitted in a $0\nu\beta\beta$ decay, the minimal observable in direct searches for $0\nu\beta\beta$ decay is the total energy of the two emitted electrons. Depending on experiment designs and purposes (detailed in Sec. 1.3.2), individual electron energies and tracks also represent interesting observables. The signature of a $0\nu\beta\beta$ signal is an excess of events, compared to the expected background noise, in the total energy spectrum, near the $Q_{\beta\beta}$ released energy. How large is this peak depends on the energy resolution of the detector. Research for this signal involves optimising a *region of interest* (ROI), also depending on the energy resolution. The total number of events $N^{0\nu}$ occuring in the ROI and in the measurement time

t, for a detector with an detection efficiency ϵ, using a source isotope of W atomic molar mass and a isotopic abundance, is defined as

$$N^{0\nu} = \ln(2)\frac{\mathcal{N}_A}{W}\left(\frac{a\epsilon Mt}{T_{1/2}^{0\nu}}\right) , \tag{1.1}$$

where $\mathcal{N}_A$ is the Avogadro number. If no excess of events is observed, the limit set on the $0\nu\beta\beta$ decay half-life is

$$T_{1/2}^{0\nu,\mathrm{lim}} = \ln(2)\frac{\mathcal{N}_A}{W}\left(\frac{a\epsilon Mt}{N_{\mathrm{exc}}}\right) , \tag{1.2}$$

N_{exc} being the number of $0\nu\beta\beta$ events excluded at a given confidence level in the ROI. Then, this sensitivity to the $0\nu\beta\beta$ decay would depend on the number of total counts in the ROI, some of them possibly being background events:

$$T_{1/2}^{0\nu,\mathrm{lim}} \propto \begin{cases} aM\epsilon t & \text{if no background is expected,} \\ a\epsilon\sqrt{\frac{Mt}{B\Delta E}} & \text{with background.} \end{cases} \tag{1.3}$$

Here B is the background rate usually expressed in counts.keV^{-1}.kg^{-1}.y^{-1} (when normalised to the width of the ROI, the source mass, and the observation time) and ΔE is the energy resolution. The advantage of a background free experiment clearly comes out: the $0\nu\beta\beta$ half life would increase linearly with the time of exposure t (as opposed to $\sqrt{t}$ for an experiment with a large number of background events). Then, it is clear that the control and the discrimination of background is of high priority for such $0\nu\beta\beta$ direct search experiments. We will discuss in Chap. 2 some important point to reduce the backgrounds for the $0\nu\beta\beta$ decay detection. Next to that, the previous expression fixes the choices that experimenters can make in designing a detector. An ideal isotope would have a high natural abundance and would be deployed with the higest mass possible in a detector with a high detection efficiency, a good energy resolution (small ΔE) under low-background conditions (small B). Of all the 35 isotopes capable of disintegrating through $2\nu\beta\beta$, none meets all the previous conditions. Expermimenters will then have to find compromises, which are at the origin of the different detection strategies. Detector can ether use an active or passive source. In the first case, the source is also the detection medium (detector technologies detailed in Sec. 1.3.2.1, 1.3.3 and 1.3.5). In the second case, the source is decoupled from the detection part of the experiment (see Sec. 1.3.4 and 1.3.6). In the next section, we provide a review of the current and future experiments that aim to discover the neutrinoless double beta decay.

1.3.1.1 Aspects of the nuclear matrix elements

1.3.1.2 Quenching

1.3.2 $0\nu\beta\beta$ direct search experiments

1.3.2.1 Semiconductors

Various semiconductor technologies are employed in the detection of $0\nu\beta\beta$ decay. The ^{76}Ge $\beta\beta$ emitter ($Q_{\beta\beta} = 2039$ keV) is historically important as it has been

Experiment	Isotope	M (kmol)	$T_{1/2}^{0\nu}$ (90 % C.L.)	$m_{\beta\beta}$ (meV)
GERDA [1]	^{76}Ge	0.41	$9\,10^{25}$	$104 - 228$
MAJORANA [2]	^{76}Ge	0.34	$2.7\,10^{25}$	$157 - 346$
CUPID-0 [3]	^{82}Se	0.063	$0.24\,10^{25}$	$394 - 810$
CUORE [4]	^{130}Te	1.59	$1.5\,10^{25}$	$162 - 757$
EXO-200 [5]	^{136}Xe	1.04	$1.8\,10^{25}$	$93 - 287$
KamLAND-Zen [6]	^{136}Xe	2.52	$10.7\,10^{25}$	$76 - 234$

adopted since the 1960s in $0\nu\beta\beta$ decay searches, acting as active source, which enhances the detection efficiency. ^{76}Ge-enriched high purity Germanium detectors (HPGe) offer both high energy resolution and extremely high radiopurity (as impurities are removed in the crystal growing process). These characteristics allow, once external background contribution is minimised, to reach high sensitivity on $0\nu\beta\beta$ decay, which makes this category of detectors one of the most promising for ton-scale experiments. Since the last generation (IGEX and Heidelberg-Moscow), HPGe detectors had been improved to reach an ultra low background rate, making way for the current generation of $0\nu\beta\beta$ detectors – GERDA, MAJORANA demonstrator and LEGEND.

The **GERDA** experiment (GERmanium Detector Array) is located at the Laboratori Nazionali del Gran Sasso (LNGS), Italy. GERDA phase I was running from 2011 to 2013 with 17.8 kg of enriched active source detectors from the HEIDELBERG-MOSCOW and IGEX experiments. Its first aim was to put to the test the controversial result of HEIDELBERG-MOSCOW experiment given in 2001, announcing the first evidence for $0\nu\beta\beta$ signal at a 4.2σ confidence level. With an exposure of 21.6 kg.y, the absence of signal in the GERDA-I experiment refuted the previous result, setting a limit $T_{1/2}^{0\nu} > 2.1\,10^{25}$ y. Since 2015, the GERDA experiment is in the second phase (see Fig. 1.1), with a total of 35.8 kg enriched detectors, 20 kg of which is Broad Energy Germanium (BEGe) detectors that have been deployed for GERDA-II, providing a better energy resolution and pulse shape discrimination. The active source is deployed inside a liquid Argon (LAr) augmented with light sensors, acting as an active external shield as well as a cooling down system. The total is surrounded by a water tank. The aim is to reach a 10^{26} y sensitivity with 100 kg.y exposure, and a background rate less than 10^{-3} counts.keV^{-1}.kg^{-1}.y^{-1}. The underground laboratory of INFN provides 3500 m water equivalent to reduce the external cosmic background. In 2019, a combined analysis for GERDA phases I and II has resulted in a half-life limit of $T_{1/2}^{0\nu} > 0.9\,10^{26}$ y (90% C.L., sensitivity assuming no signal is $1.1\,10^{26}$), corresponding to an effective neutrino mass of $m_{\beta\beta} < 0.07$-0.16 eV (90% C.L.)[1].

MAJORANA demonstrator
LEGEND

---

[1]This result depends on the nuclear matrix elements used for the calculations. See Sec. 1.3.1.1.

roof of cleanroom
plastic muon veto
lock
glove box
floor of clean room
cryostat (Ø 4m, 64m³)
Ge detector array &
LAr veto system
PMT of muon veto
water tank (Ø 10m, 590m³)
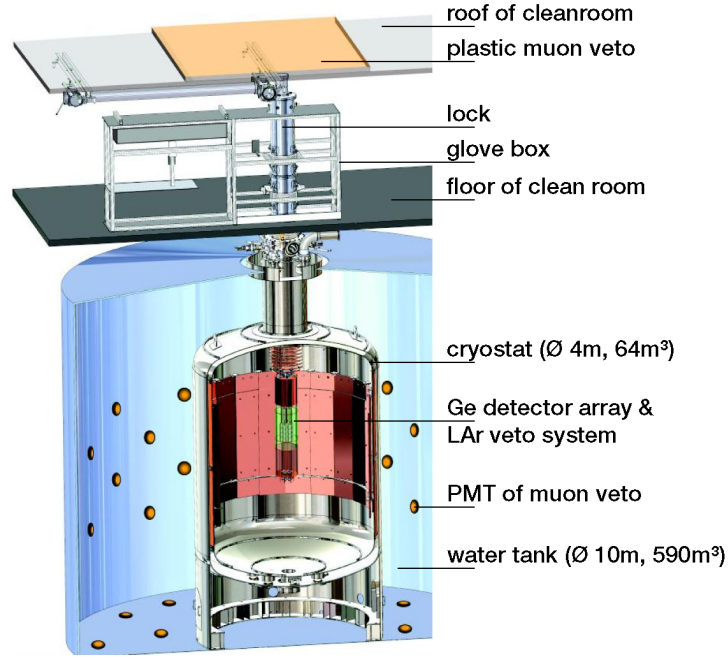
Figure 1.1

1.3.3 Bolometers

Bolometers are high energy resolution and high detection efficiency calorimeters operating at low temperatures ($\simeq 10-20$ mK). This type of detector is particularly suitable for $0\nu\beta\beta$ searches, with the possibility of building large-scale experiments.

CUORE
CUPID
AMoRE

1.3.4 Time projection chambers

Time Projection Chambers (TPC) detectors use a medium producing two ways to measure the electron energies: a *scintillation* (ultra-violet light) prompt signal, and a *ionisation* delayed signal. When a particle crosses the detector, a scintillation light is emitted, the energy of the scintillation peak depending on the medium. Scintillation photons, travelling at speed of light in the medium, are detected by photosensors, giving the *zero-time* of the event. The crossing particle ionises the medium all along its way, creating electrons drifting to a collection system (an electric field is applied between cathode and anode), allowing the precise measurement of the electron production location in a 2D plane. The drift time measurement gives access to the third coordinate of the interaction point. Therefore, combining the two consecutive signals allows precise position and energy reconstruction. An discriminating observable is the ionisation-to-scintillation ratio (see Fig. 1.2) as it provides particle discrimination between α particles (low ratio) and γ radiations and β particles (high ratio). For $0\nu\beta\beta$ searches, ^{136}Xe-enriched isotope in liquid phase is used, offering a maximal source density (more compact
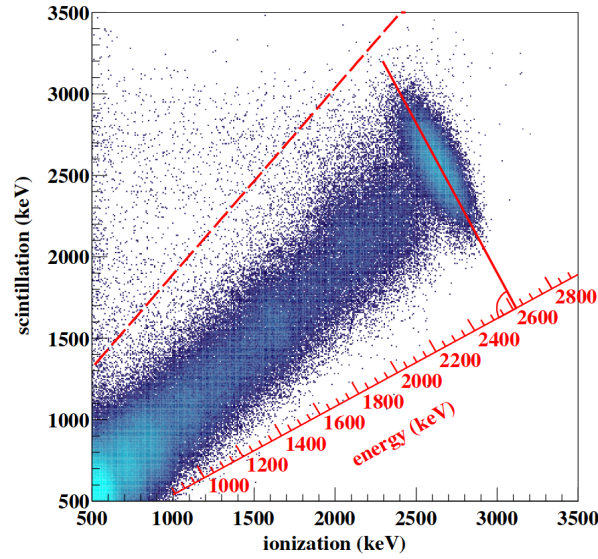
Figure 1.2

detecors) and a good position resolution. Unfortunately, the energy resolution is worse than that of the gas-phase TPCs detectors[2]. Noble elements are natural radiation detectors, avoiding the need for excess materials that could generate extra radioactive backgrounds. ^{136}Xe-enriched is the only noble element capable to $2\nu\beta\beta$ decay, with $Q_{\beta\beta} = 2457.8$ keV. This isotope has a relatively high natural abundance (9%), can be enriched to highly pure concentrations, and does not have other long-lived radioactive isotopes, making it interesting for large-scale TPCs $0\nu\beta\beta$ experiments.

The **EXO-**200 experiment is a prototype of the Enriched Xenon Observatory (EXO) project, currently operating in a room under an overburden of 1624 m.w.e, at the Waste Isolation Pilot Plant (WIPP), USA. The detector is shaped as a cylinder, with two back-to-back cylindrical TPCs. A high negative voltage grid cathode helds at the mid plane of the detector (40 cm diameter), and two anodes are located on both sides, at ground potential. A cross-section of the detector is displayed in Fig. 1.3. With 110 kg of enriched ^{136}Xe in liquid phase (the detector is held at 167 K in a cryongenic bath), the phase I of this TPC detector has measured for the first time the Xenon $2\nu\beta\beta$ decay with $T^{0\nu}_{1/2} = 2.165 \times 10^{21}$ y. Between phase I and IIa, the detector was upgraded with improved low-noise electronics, a Radon suppression system, and the impurities contents of the Xenon were reduced by a factor ten. The current detector performance shows an energy resolution of 2.90% (FWHM) at the decay Q-value and a background rate of $(1.6) \times 10^{-3}$counts.keV^{-1}.kg^{-1}.y^{-1}. EXO-200 phase IIa data placed a new limit of $T^{0\nu}_{1/2} > 1.8 \times 10^{25}$ y (90% C.L.). The final analysis of data is in progress.

nEXO

NEXT

---

[2]Two-phase liquid-Xenon detectors are developed for Dark Matter searches and could be exploited for $0\nu\beta\beta$ direct searches with the DARWIN project.

HV FEEDTHROUGH
COPPER VESSEL
CATHODE
VUV TEFLON
REFLECTOR TILES
U AND V
WIRE PLANES
WELDED
BULKHEAD
Xe AND
CABLE DUCT
APD
WIRING
SYSTEM
30cm
FIELD
SHAPING RINGS
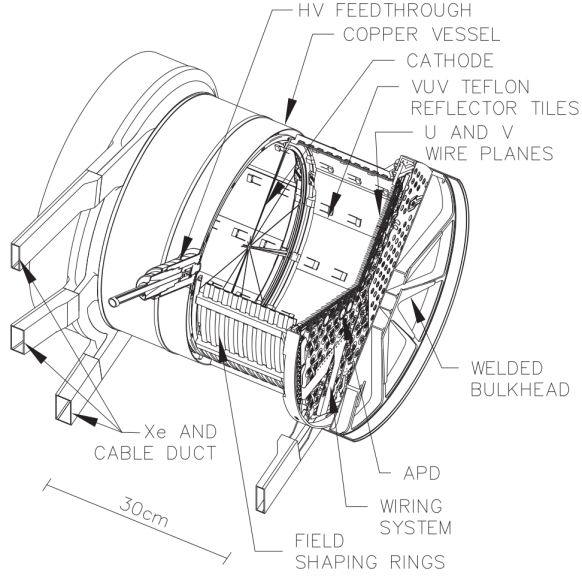
Figure 1.3

PandaX-III

1.3.5 Scintillators

KamLAND-ZEN and KamLAND2-ZEN
ZICOS
CANDLES

1.3.6 Tracking calorimeters

Tracking calorimeters technology, instead of using a *source-as-detector*, employ a passive source shaped as thin source foils of enriched $\beta\beta$ emitters. Sources are placed at the detector centre, surrounded by two trackers allowing for particle identification (between electrons, positrons, γ and α particles) and vertex reconstruction to improve the background rejection. The whole is sandwiched between calorimeters enabling individual particle energy reconstruction. In case of a discovery, this passive source tracking calorimeter technology provides topological information on angular emissions of the two electrons from $\beta\beta$ decay, making possible to distinguish between underlying mechanisms for $0\nu\beta\beta$ decay (see Sec. 1.2.2).

The **SuperNEMO** experiment is a next-generation of detector, inheriting the lineage of the NEMO (Neutrino Ettore Majorana Observatory) experiments, which successfully studied multiple isotopes as enriched Molybdenum ^{100}Mo.

The SuperNEMO demonstrator

2.1 Demonstrator design

2.1.1 Comparison with NEMO3 experiment

2.1.2 Expermimental design

2.1.3 Sources

- Choice of source material

2.1.4 Tracker

2.1.5 Calorimeter

2.1.5.1 Scintillator

2.1.5.2 Photomultiplier

2.1.6 Calibration systems

2.1.7 Control Monitoring system

2.1.8 Electronics

2.2 The backgroung of SuperNEMO

2.2.1 Internal background

Trace quantities of naturally-occurring radioactive isotopes can occasionally produce two-electron events and thus can mimic $\beta\beta$-decay events. The largest contributions come from isotopes of decay chains of ^{238}U, ^{232}Th and ^{40}K, which disintegration occur inside the source foils, as well as inside the tracking volume.

Décire la contamination mesurée des sources, et du radon dans la partie suivante
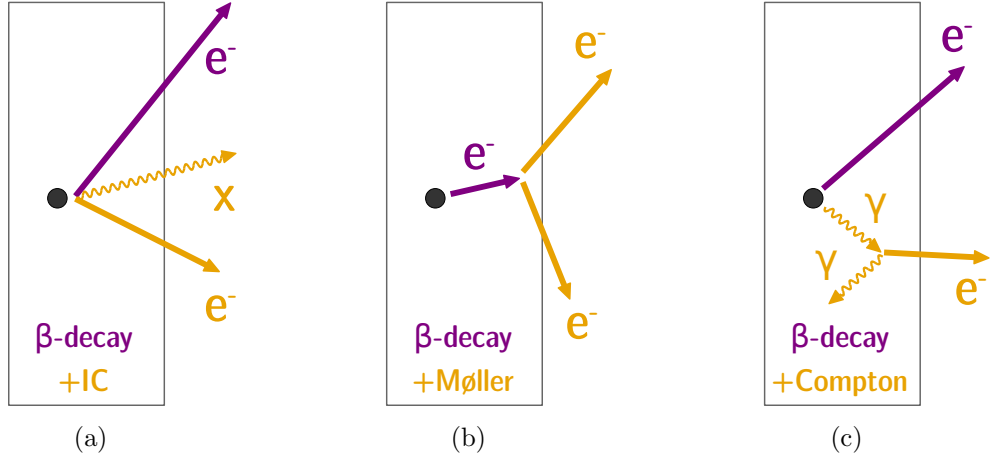
Figure 2.1: (a) β decay + internal conversion: radioactive nucleus performs a β decay, then an electron is emitted after internal conversion of photon (b) β decay + Møller: (c) β decay + Compton diffusion: radioactive nucleus β decays to an excited state, then the photon perfoms a Compton diffusion.

2.2.1.1   Measurement of ^{208}Tl in the one electron and $n\gamma$ channel

The ^{208}Tl contamination inside the source foils is one of the main backgrounds for the neutrinoless double beta decay, with the internal ^{214}Bi, as well as the Radon gas in the tracker. One of the key features of the SuperNEMO demonstrator remain its ability to measure its own background in dedicated channels, which are independent from the main signal channels.

As explained before, ^{208}Tl emits one electron and between 1 and 3 γ's. Consequently, the $1e1\gamma$, $1e2\gamma$ and $1e3\gamma$ channels can be used to discriminate internal ^{208}Tl events, and measure the activity of the source. However, since the particles share the same fixed energy, the more particles there are, the less energy they will carry. It is therefore less likely for three γ to be detected at the same time. A significant contribution to the $1e1\gamma$ and $1e2\gamma$ channels is also expected from other radio contaminants, like ^{214}Bi, and from radon events.

Specified contamination levels have been established in order to achieve the $0\nu\beta\beta$ half-life target of $\sim 1 \times 10^{26}$ years for the final detector. The ^{82}Se demonstrator source is segmented in 34 foils, whose production was the responsibility of different laboratories (Dubna, LAPP and Tomsk). The sources have undergone different purification treatments, in order to investigate new techniques, and to compare them with those of NEMO-3. After the sources production and purification, preliminary measurements have been performed with the BiPo-3 detector to determine the actual ^{208}Tl and ^{214}Bi contamination levels inside the foils [27]. The level of radon emissions inside the tracker was also measured by the collaboration, for each of the four sections of the chamber, using a concentration line. We summarise all these contamination levels in Tab. 2.1, and give a comparison with the detector initial specifications. The targeted ^{208}Tl level is not reached, being almost 27 times higher than expected, and 3.0×10^4 internal Thallium events are expected in 2.5 years. Nevertheless, on average, the activity of the sources was improved by a factor of 2 compared to the ^{100}Mo sources

	Specified activities	Measured activities
^{208}Tl	$2\,\mu$Bq.kg^{-1}	$54\,\mu$Bq.kg^{-1} [26 - 102]
^{214}Bi	$10\,\mu$Bq.kg^{-1}	$< 290\,\mu$Bq.kg^{-1}
^{222}Rn	0.15 mBq.m^{-3}	0.15 ± 0.02 mBq.m^{-3}

Table 2.1: Measured and specified activities for the SuperNEMO demonstrator. The ^{222}Rn tracker contamination is measured with a concentration line [28], extrapolated with a 2 m^3/h flow rate. The limit on ^{214}Bi contamination is provided by BiPo measurements for a 90% CL [27].

of NEMO-3. In addition, valuable information has been accumulated on the different production techniques, which are of great importance for the final detector construction. In particular, the two best ^{208}Tl sources activities were reached by inverse chromatography, reaching a 20 ± 10 μBq/kg level, an improvement by a factor 5 compared to NEMO-3. This encourages for further investigations in this direction. The sensitivity of BiPo detector only allowed to give an upper limit on the level of internal ^{214}Bi (an activity of 290 μBq/kg would correspond to 1.6×10^5 internal Bismuth events in 2.5 years). Precise measurements are expected from the demonstrator calibration. Radon emissions from the tracker were also measured, and extrapolated with an air flow rate of 2 m^3/h inside the chamber, showing the targeted level of 0.15 mBq.m^{-3} was reached.

2.2.2   External background

Radon:
Radon is a noble gas which occurs as an indirect decay product of uranium and thorium. Due to its chemical properties, radon has a long diffusion length in solids, making it difficult to remove. Radon contaminations inside the tracker volume is a major background to the rare event experiments such as SuperNEMO. Simulations show that, to achieve the designed sensitivity, the level of radon must not exceed 0.15 mBq/m^3 since its decay daughter ^{214}Bi, $Q_{\beta\beta} = 3.2$ MeV can mimic a $0\nu\beta\beta$ event. Radon concentration measurements inside the demonstrator tracker have been performed by the SuperNEMO collaboration, revealing an activity of 0.15 ± 0.02 mBq/m^3, through the combination of an anti-radon tent and an air-flushing method.

They are outgased in the air from the rock walls of the experimental hall and can enter the detector either through tiny gaps between sectors or through gas pipe joints. The progeny of radon and thoron produces γ-rays and β decays accompanied by internal conversion (IC), Møller or Compton scattering.

2.2.3   Background specifications

2.2.4   Measured demonstrator background levels

2.3   Magnetic field

It is, however, not high enough to impact significantly neither the few muons nor the α particles expected to be detected by the tracker. Due to their much higher momenta, they will instead leave straight tracks in the wire chamber.

2.4   The SuperNEMO software

2.4.1   Simulation

As described in Sec. 2.4 of Chapter 2, the SuperNEMO collaboration developed its own simulation, reconstruction and analysis environment. The Falaise software, specifically designed by and for the SuperNEMO collaboration, holds the `C++` library for the event reconstruction and analysis of simulated and real data. Especially, it contains the geometry, the detector material, the event data model, the reconstruction algorithms and the data analysis. Finally, the SNFee software is a tool package for the configuration, control and monitoring of the SuperNEMO front-end electronics.

2.4.2   Reconstruction

Particle identification with detector scheme

2.4.3   Modifications of simulation software

2.5   Analysis tools

2.5.1   Internal probability

Internal probability is a mathematical tool used to quantify the probability that two particles were emitted simultaneously and at the same location in the source foils. This tool is based on the particle Time-Of-Flight computation. Firstly, we define, for two particles, the internal χ^2

$$\chi^2_{int} = \frac{((t_1^{exp} - t_1^{th}) - (t_2^{exp} - t_2^{th}))^2}{\sigma^2_{tot}} \, . \tag{2.1}$$

t_i^{th} is the theoretical time of arrival of the particle i inside the calorimeter, t_i^{exp} the arrival time experimentally measured, c is the speed of light, and σ_{tot} is the quadratic sum of all uncertainties. The theoretical time, is defined as

$$t_i^{th} = \frac{L_i}{\beta_i \, c} \, , \tag{2.2}$$

where L_i is the reconstructed track length, and β_i corresponds to

$$\beta_i = \frac{\sqrt{E_i(E_i + 2m_i)}}{E_i + m_i}\,, \tag{2.3}$$

E_i being the energy of the particle and m_i its mass. The total uncertainty, σ_{tot}, is defined as

$$\sigma_{tot} = \sqrt{\sigma_{t_1}^2 + \sigma_{t_2}^2 + \sigma_{\beta_2}^2 + \sigma_{\beta_1}^2 + \sigma_{l_1}^2 + \sigma_{l_2}^2}\,. \tag{2.4}$$

We compare the experimental time difference to the theoretical time difference, to see if it can be explained only by the difference in track lengths. If it is compatible, which means of the order of the experimental uncertainties, the associated χ^2 will be low i.e. close to 1 or lower.

The uncertainty σ_t on the time measurement This term is directly related to the phenomenon of absorption and re-emission of scintillation photons detailed in Chapter 6. It is defined as

$$\sigma_t = \sqrt{\frac{\tau_{\mathrm{SC}}^2 + \left(\dfrac{\mathrm{FWHM_{TTS}}}{2\sqrt{2\ln 2}}\right)^2}{\mathrm{N_{PE}}}}\,, \tag{2.5}$$

where τ_{SC} is the scintillator characteristic time, due to the scintillator de-excitation time: it corresponds to the time emission of the scintillation photon responsible for the creation of the photoelectron on the photocathode. $\mathrm{FWHM_{TTS}}$ is the temporal dispersion linked to the photomultiplier: the transit time of the photoelectrons inside the photomultiplier can evolve, according to its point of creation on the photocathode. This transit time is unique for each photomultiplier, and has to be characterise experimentally. For the SuperNEMO scintillators, $\tau_{\mathrm{SC}} = 2.5$ ns [?] and $\mathrm{FWHM_{TTS}} = 2.25$ ns [?]. $\mathrm{N_{PE}}$ is the number of photo-electrons emitted after a particle has deposited all its energy E in the scintillator:

$$\mathrm{N_{PE}} = E \times \left(\frac{2\sqrt{2\ln 2}}{\mathrm{FWHM_E}}\right)^2\,, \tag{2.6}$$

where $\mathrm{FWHM_E}$ is the energy resolution of the PM, 8 % at 1 MeV for the SuperNEMO calorimeter. Therefore, for a particle of 1 MeV depositing all its energy inside a scintillator, $\mathrm{N_{PE}} \sim 866$ photo-electrons are emitted, an improvement of ? % compared with NEMO-3. Finally, the uncertainty σ_t on the time measurement can be estimated thanks to a relative calibration of the PMs, and depends on the incomming particle nature (photon or electron). Preliminary studies gave a first estimation of this paramater [?] and found $\sigma_t = 342 \pm 10$ ps for 1 MeV gammas entering the front face of the scintillator, and $\sigma_t = 248 \pm 6$ ps for 1 MeV electrons. On the occasion of the SuperNEMO detector commissioning, we finalise this study and characterise the calorimeter time resolution in Chapter 5.

The uncertainty σ_β on the particle energy This term is derived from Eqs. (2.2) and (2.3):

$$\sigma_{\beta_i} = \frac{t_i^{th} \times m_i^2}{E_i \times (E_i + m_i) \times (E_i + 2m_i)} \times \sigma_E \,, \tag{2.7}$$

where $\sigma_E = \text{FWHM}_E \times \sqrt{E_i}$ represents the energy resolution of the PM for the energy E_i.

The uncertainty σ_L on the reconstructed track length This corresponds to the typical uncertainty due to particles track reconstructions, due to the uncertainty on the interaction point inside the scintillator block. This uncertainty is greater for γ particles than for electrons. Indeed, thanks to the gas chamber and the trajectory fitting, valuable informations on the impact point inside the scintillator are provided for electrons crossing the tracker, while photons only deposit their energy inside the calorimeter, without ionising the tracker gas. In the framework of the optimisation of γ reconstruction in the superNEMO detector, a previous study has evaluated the uncertainty on the track length for γ's, by simulating monokinetic γ's, and estimated $\sigma_L = 0.9$ ns [9]. The value used in the simulation/reconstruction pipeline, for the case of electrons, is inherited from the NEMO-3 analysis with $\sigma_L = 0.1$ ns. An optimisation of this parameter is given in Chapter 4.

We would translate the internal χ^2 distribution into the so-called *internal probability* through

$$P_{int} = \frac{1}{N} \int_{\chi^2_{int}}^{+\infty} x^{-\frac{1}{2}} e^{-\frac{x}{2}} dx \,, \tag{2.8}$$

with N the normalisation factor. This formula transforms the χ^2 Gaussian distribution into a flat distribution between 0 and 1. One of the benefits of using the probability distribution rather than the χ^2 distribution is that it brings extra qualitative information, especially useful to check the estimation of the uncertainties. The shape of the probability distribution can bring out an overestimation or, a contrario, an underestimation of the uncertainties, which would translate into a positive or a negative slope, respectively. On the other hand, a flat distribution signifies an appropriate estimation of the errors and confirms the Gaussian distribution of the original quantity measured.

2.5.2 External probability

Sensitivity of the SuperNEMO demonstrator to the $0\nu\beta\beta$

We present a study aiming to evaluate the SuperNEMO sensitivity to the $0\nu\beta\beta$ decay, and the corresponding effective neutrino mass. Studies of this kind have already been conducted, and the final detector, based on the NEMO-3 technology, is expected to exclude half-lives up to 1.2×10^{26} y (90% CL), with an exposure of 500 kg.y with Selenium sources[1] [8]. The SuperNEMO demonstrator were designed in order to assess the technical feasibility of such a large-scale detector. Its installation started in early 2015, at the Laboratoire Souterrain de Modane. With a reduced exposure of 17.5 kg.y, this demonstrator is expected to reach a sensitivity on the $0\nu\beta\beta$ process of 5.3×10^{24} y (90% CL) [9].

As was the case with its predecessor, a copper coil was designed to deliver a magnetic field inside the wire chamber, to bend the charged particles trajectories, hence making it possible to discriminate between electrons and positrons. However, studies lead by the collaboration determined that this field could be impacted by the detector material (especially by the calorimeter magnetic shields), producing notable variations in intensity and a loss of energy resolution [9][10]. We aim to explore the impact, on both the demonstrator and final detector sensitivity, of the presence of this magnetic field. The findings of this study participate in better understanding the detector performances. In a context of investigating the demonstrator and final detector's capabilities, different internal source contamination levels are considered. The topology of interest is the two electrons topology, and we use the total energy sum to discriminate the signal from the background events. Thanks to SuperNEMO tracking capabilities, extra topological informations are exploited to improve the final sensitivity. To go further, we also explore the possibility of studying the $0\nu\beta\beta$ decay of other $\beta\beta$ isotopes.

3.1 The $0\nu\beta\beta$ signal and background model

A full simulation of the demonstrator was performed, to determine the upper limit on $0\nu\beta\beta$ half-life that can be probed with SuperNEMO. Due to the time it would

---

[1]Supposing the $0\nu\beta\beta$ decay of ^{82}Se occurs through the exchange of a light Majorana neutrino.

take to simulate every background contribution, we choose a simplified model. Indeed, in addition to signal simulations, only the most harmful backgrounds to the $0\nu\beta\beta$ decay search were simulated.

3.1.1 The $0\nu\beta\beta$ signal

The SuperNEMO detector was designed to search for the never-observed $0\nu\beta\beta$ decay. In the following, we assume the underlying mechanism for this decay is the exchange of a light Majorana neutrino, the so-called mass mechanism (MM), as it is the most widespread. The hypothetical $0\nu\beta\beta$ signal would be detected as an excess of events in the region of interest, with respect to the predicted background contamination levels. Some 10^7 $0\nu\beta\beta$ events were simulated inside the source foils, using the DECAY0 software [13].

3.1.2 Inside detector backgrounds

We simulated numerous types of backgrounds that could mimic and hinder the search of the $0\nu\beta\beta$ signal.

3.1.2.1 Internal backgrounds

The so-called *internal backgrounds* stand for decays occurring inside the source foils, presenting the same signature as the $0\nu\beta\beta$ signal. These backgrounds are mainly the $2\nu\beta\beta$ decay undergone by the source isotope, as well as disintegrations of ^{208}Tl and ^{214}Bi inside the source foils.

The $2\nu\beta\beta$ process

In the full energy range, the allowed $2\nu\beta\beta$ decay stands as the dominant internal background type. The corresponding two-electrons energy sum spectrum is a continuum, whose ending point should stands at $Q_{\beta\beta} = 2.99$ MeV, but is subtly shifted by the detector's energy resolution. We simulated 10^7 events of this decay inside the source foils, in the full energy window. However, above a certain energy value, the number of $2\nu\beta\beta$ events decreases, which can lead to a lack of statistics in a energy region favourable for the search of $0\nu\beta\beta$ signal. To offset this effect, we simulated additional 10^7 of this decay on a slightly reduced energy range, that is to say above 2 MeV. The second set of simulations is normalised with the first one. In this way, the lack of $2\nu\beta\beta$ simulated events in the high-energy tail is avoided, without requiring too high computational resources.

Source foils contamination by natural isotopes

As described in Sec. 2.2.1, after sources purification, remaining natural isotopes such as ^{208}Tl or ^{214}Bi can still be present inside the foils, constituting the principal internal source of background, with the $2\nu\beta\beta$ decay. We simulated 10^7 decays for each of the two isotopes, inside the source foils.

3.1.2.2 Tracker contamination by natural isotopes

The presence of gaseous ^{222}Rn inside the tracker, mainly deposited on the tracker wires, can produce events similar to internal ones. In fact, one of the progeny of ^{222}Rn, the ^{214}Bi, can decay on (or near) a foil, and appear with a two-electron topology, becoming hard to distinguish from a double beta decay candidate. As this isotope is distributed throughout the whole tracking detection volume, we simulated a large quantity of this decay, that is to say 10^8 decays on the tracker wires.

3.1.3 External backgrounds

This background category was described in detail in Sec. 2.2.2. As a reminder, it is populated by the external γ-ray flux produced by radioactive isotope decays (mostly ^{40}K, ^{214}Bi and ^{208}Tl) in detector components or surrounding laboratory rocks, as well as neutron interactions in the external iron shield. As simulating external backgrounds would be very consuming in terms of computing ressources due to their very low probability to produce two electrons ($2e$) topologies, let us check that these simulations are indispensable. The NEMO-3 experiment set a limit on the external background number of counts, of < 0.2 events in the $2e$ topology, for the energy range [2.8;3.2] MeV (two electrons energy sum), for an exposure of 34.3 kg·y, with ^{100}Mo sources [14]. Recent radiopurity measurements of the SuperNEMO PMTs allow to conclude that the PMT ^{214}Bi activity is 35% lower than for those of NEMO-3 [15], which is encouraging. Unfortunately, these measurements also revealed that the PMT budget in ^{208}Tl isotope is 150% higher than NEMO-3. This could lead us to think that the external background contribution for SuperNEMO could be higher than that of NEMO-3. However, on that level, the most notorious difference between the two detectors is the fact that the SuperNEMO scintillator blocks are thicker than those of NEMO-3. Therefore, a gamma emitted from a PMT glass is more likely to be detected before crossing the source foils, such that it would be rejected and would not contribute to the background in the $2e$ channel. Even if the regions of interest are slightly different between these two experiments, it produces a negligible increase on the external background contribution[2]. After all, given the fact that SuperNEMO is expected to be better than NEMO-3 at rejecting external background events, we consider that all external backgrounds from outside the foil, apart from ^{222}Rn in the tracking volume, are expected to be negligible, and were not simulated.

3.1.4 Amount of simulation

The number of natural isotope decay events expected in the $2e$ topology depends on their activities inside the source foils (for ^{208}Tl and ^{214}Bi), or on the tracker's wires (for ^{222}Rn decaying in ^{214}Bi). Therefore, it is mandatory to constrain

---

[2]A study conducted by the SuperNEMO collaboration shown that at most 0.73 additional external background events would have been expected for the NEMO-3 detector, if instead of taking the [2.8;3.2] MeV energy range, we would have considered the [2.7;3.15] MeV region of interest.

the maximal tolerable activities for the detector [11]. The collaboration then established recommendations for maximum levels of the internal backgrounds, expressed in number of disintegrations per second, for a unit mass of $\beta\beta$ isotope, or for a unit volume of gas. These *specified activities* have been calculated in order to achieve the expected sensitivity of the final detector.

The amount of expected double β decays is driven by its half-life value: the higher the half-life, the lower its contribution in the total number of expected background. For this analysis, we consider the $2\nu\beta\beta$ half-life of ^{82}Se measured by NEMO-3, $T_{1/2}^{2\nu} = 9.39 \pm 0.17$ (stat) ± 0.58 (syst) $\times 10^{19}$ years [12]. For the $0\nu\beta\beta$ process, we also take the best limit set by the NEMO-3 detector, $T_{1/2}^{0\nu} > 2.5 \times 10^{23}$ y [12]. This value is given for illustration purposes only, as it is not used to estimate the sensitivity of the detector.

Tab. 3.1 gives the expected number of signal and background events, for the demonstrator and final detector exposures. We also summarise the amount of

Process	Expected decays		Simulated decays
	Demonstrator	Final detector	
$0\nu\beta\beta$ ($T_{1/2}^{0\nu} = 2.5 \times 10^{23}$ y)	3.6×10^2	1.0×10^4	1.0×10^7
$2\nu\beta\beta$ ($T_{1/2}^{2\nu} = 9.39 \times 10^{19}$ y)	9.5×10^5	2.7×10^7	1.0×10^7
^{208}Tl ($\mathcal{A}^{\text{Tl}} = 2\ \mu$Bq/kg)	1.1×10^3	3.1×10^4	1.0×10^7
^{214}Bi ($\mathcal{A}^{\text{Bi}} = 10\ \mu$Bq/kg)	5.5×10^3	1.6×10^5	1.0×10^7
^{222}Rn ($\mathcal{A}^{\text{Rn}} = 0.15$ mBq/m^3)	1.8×10^5	7.2×10^6	1.0×10^8

Table 3.1: Expected number of events for signal and background, for the demonstrator (17.5 kg.y) and for the final detector (500 kg.y). We assume target background activities are reached: $\mathcal{A}^{\text{Tl}} = 10\ \mu$Bq/kg, $\mathcal{A}^{\text{Bi}} = 2\ \mu$Bq/kg, $\mathcal{A}^{\text{Rn}} = 0.15$ mBq/m^3. The measured half-life $T_{1/2}^{2\nu} = 9.39 \times 10^{19}$ y for ^{82}Se is considered, and we assume $T_{1/2}^{0\nu} = 2.5 \times 10^{23}$ y [12]. The total amount of simulation is also given.

simulated decays for this analysis. The expected number of disintegrations do not take into account any technique to reject background, and are given for the full energy range. Indeed, they are expected to be extremely reduced, notably by the application of event selections aimed at maximising the sensitivity to the $0\nu\beta\beta$ half-life. Moreover, for the current sensitivity analysis, we focus on a narrow energy window, called *region of interest*, whose usefulness is described in detail in Sec. 3.2. This is also one of the reasons why we have chosen to simulate a large number of events, so that the signal and backgrounds are correctly represented in the region of interest.

3.2 Event selection

For SuperNEMO, the $0\nu\beta\beta$ signature is two-electrons events, emitted simultaneously from the same vertex on the source foils, with an energy sum compatible with $Q_{\beta\beta} = 2.99$ MeV for ^{82}Se sources. Therefore, we conducted this analysis selecting only events matching the $2e$ topology.

3.2.1 Electron definition

To define what a two-electrons topology is, we should first define how an electron is defined. A reconstructed particle is tagged as an electron if it has

- a vertex on the source foil,

- a reconstructed track inside the wire chamber,

- an associated calorimeter hit,

- and a final criterion depending on the charged particle curvature. In fact, as announced, we aim at studying the influence of the magnetic field on the final sensitivity results. To this end, we are led to consider two separate cases, one where the magnetic field is switched on, aligned with the Z (vertical) axis of the detector, with a uniform value of 25 Gauss, and one where it is switched off (see details in Sec. 3.5). In the first case, particles such as electrons and positrons of a few MeV have a curved trajectory in the tracker. In the second case, the tracks of the particles may be similar to straight lines (not to mention the possible multiple scattering on the wires of the tracker). It is then necessary to adapt the selection of events to each case. When the magnetic field is on, we consider a fourth criterion: a particle is identified as an electron if its track has a negative curvature[3]. In the following, we present results where the magnetic field is turned on. The off-field study is addressed in Sec. 3.5.

All these selections represent the so-called *first-order* cut-offs.

3.2.2 Total energy spectrum

In Fig. 3.1, we present the total energy spectra for each simulated process in the $2e$ topology, after application of the first-order cut-offs. The distributions are given for the demonstrator (^{82}Se sources, 17.5 kg.y exposure), considering the specified activities are reached.

- If the $0\nu\beta\beta$ decay is detected, the two-electrons energy sum distribution would be a peak, located at the end-point of the $2\nu\beta\beta$ energy distribution, that is to say at the total available energy, $Q_{\beta\beta} = 2.99$ MeV. As the two electrons of this decay would share the total available energy, this peak should be infinitely thin. However, a widening of this distribution is expected, due to energy losses inside the dense source material. Indeed, the path of an electron in the source is more or less long, depending on the disintegration location, and the emission angle, leading to a degradation of the measured energy. This peak is also expected to be shifted towards small energies, by the calorimeter energy resolution and the straggling of energy losses inside the wire chamber. Consequently, the $0\nu\beta\beta$ energy distribution is expected to be asymmetrical, as displayed in the figure.

---

[3]A trajectory is said to be negative if it has the same curvature as that of an electron moving from the source to the calorimeter, in a magnetic field oriented according to $+Z$.
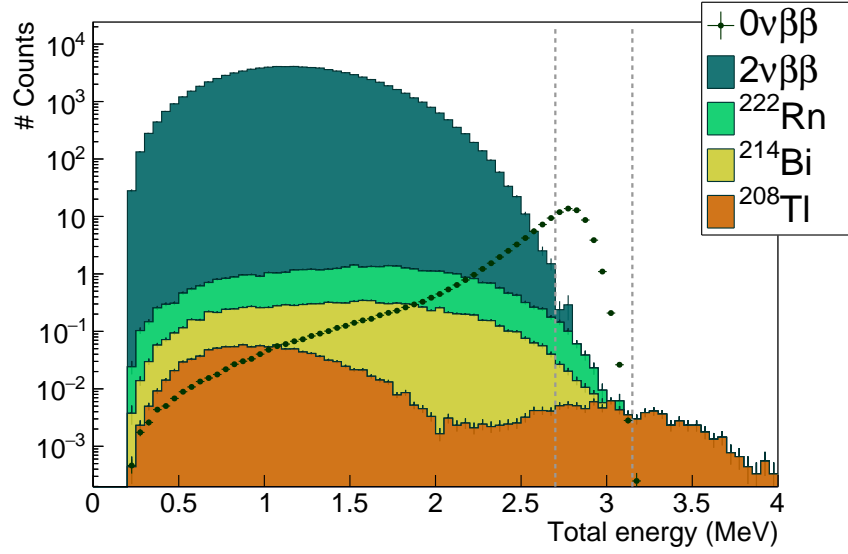
(a) Full energy range.
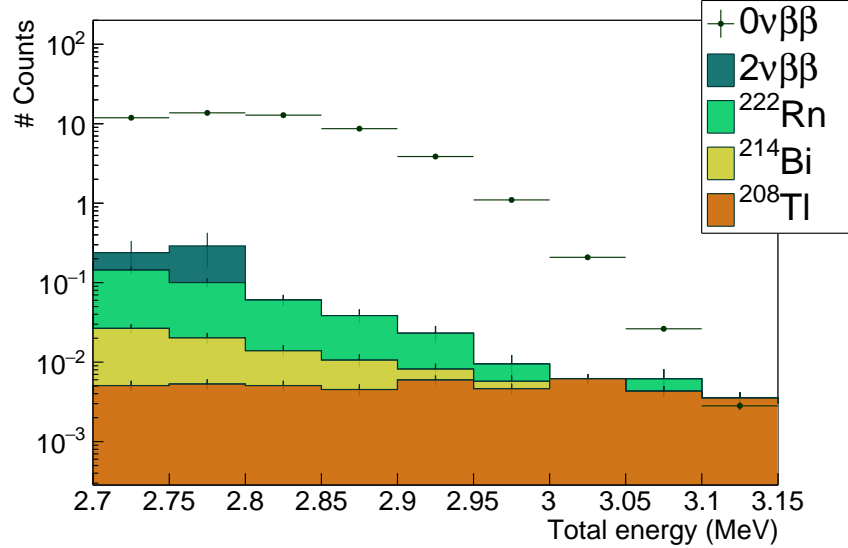
(b) Zoom on ROI.

Figure 3.1: Total energy spectra for the $0\nu\beta\beta$ signal and main backgrounds, for (a) the full energy range, and (b) for the [2.7;3.15] MeV energy range, whose optimisation is discussed in Sec. 3.3. The $2\nu\beta\beta$ spectrum is normalised to $T_{1/2}^{2\nu} = 9.39 \times 10^{19}$ y, and the specified activities are considered for ^{208}Tl,^{214}Bi and ^{222}Rn. The amplitude of the $0\nu\beta\beta$ is arbitrarily set at the limit obtained with NEMO-3.

- As explained in Sec. 3.1, we simulated two sets of $2\nu\beta\beta$ events: one on the full energy range, and one for which the two-electrons energy sum is greater than 2 MeV. After the normalisation of these two sets, we get the complete $2\nu\beta\beta$ energy spectrum displayed in the figure.

- The ^{208}Tl total energy spectrum extends up to high energies. It reveals two

distinct peaks, one corresponding to a low-energy β particle, the other to the internal conversion of the 2.614 MeV gamma, emitted after ^{208}Tl β^- disintegrations (Sec. 2.2.1).

- Whatever their origin, either ^{222}Rn contaminations inside the tracker gas, or internal contaminations of the source foils, the two ^{214}Bi energy distributions have nearly the same shapes.

These energy spectra confirm the $2\nu\beta\beta$ background is dominant in the total energy range. Therfore, a widespread technique consists in constraining the $0\nu\beta\beta$ decay searches to a narrow energy range, the so-called *region of interest* (ROI). It allows to reduce the total number background decays, while maximising the chances of observing the signal decay. A typical ROI is materialised in the figure by two vertical dashed lines, revealing ^{208}Tl, ^{214}Bi and ^{222}Rn could be harmful for the search of the $0\nu\beta\beta$ decay. The influence of the sources contamination by these natural isotopes, as well as optimised background rejection techniques are presented in Sec. 3.4.

In the following, we expose general principles leading to the determination of the best limit on $T^{0\nu}_{1/2}$, in the appropriate region of interest. We illustrate the reasoning by applying it on the demonstrator case, with specified activities, and on-magnetic field condition. However, the technique presented remain valid for all exposures, internal contamination levels and field conditions.

3.3   Demonstrator sensitivity to the $0\nu\beta\beta$ decay of ^{82}Se

The SuperNEMO demonstrator is designed to measure $\beta\beta$ decays of radiaoctive emitters. In case a the non-obervation of the $0\nu\beta\beta$ process, the collaboration would set an upper-limit on the half-life $T^{0\nu}_{1/2}$, and on the effective neutrino mass $m_{\beta\beta}$.

3.3.1   Sensitivity to the $0\nu\beta\beta$ half-life

In case of the non-observation of a $0\nu\beta\beta$ signal, the expected upper limit on the half-life is provided for a given energy range $[E_{\min};E_{\max}]$ on the two electrons energy sum, and depends on the characteristics of the detector. Firstly, it depends on the signal detection efficiency, $\epsilon_{0\nu}$, in this energy window. It also depends on the source isotope nature, as well as on the detector exposure $m \times t$, with m the mass of source material in the foils and t the data acquisition time period. It follows

$$T^{0\nu}_{1/2} > \frac{\mathcal{N}_A \ln 2}{M} \times \frac{\epsilon_{0\nu} \times m \times t}{N^{\text{excl.}}_{0\nu}}, \qquad (3.1)$$

with $\mathcal{N}_A$ the Avogadro number and M the $\beta\beta$ emitter molar mass. $N^{\text{excl.}}_{0\nu}$ is the number of signal events excluded, calculated with the Feldman-Cousins statistics from the total expected number of background events. The Feldman-Cousins statistics [16] is a wide-used method in rare events search experiments, providing

confidence intervals for upper limits in the case of background events following a Poissonian probability law. We use this method in the framework of this analysis to provide a limit, at 90% CL, on the number of excluded signal events $N_{0\nu}^{\mathrm{excl.}}$, on the basis of the expected number of background events, given below.

- The $2\nu\beta\beta$ background
  Eq. (3.1) defines the upper limit on $T_{1/2}^{0\nu}$ from the number of excluded signal events, and the signal selection efficiency $\epsilon_{0\nu}$. In a similar manner, we can define the number of expected $2\nu\beta\beta$ events, $N_{2\nu}$, from the half-life $T_{1/2}^{2\nu}$ and the $2\nu\beta\beta$ selection efficiency, $\epsilon_{2\nu}$, as

$$N_{2\nu} = \frac{\mathcal{N}_A \ln 2}{M} \times \frac{\epsilon_{2\nu} \times m \times t}{T_{1/2}^{2\nu}} \,. \tag{3.2}$$

- Natural radioactive backgrounds
  We consider the background massic activities $A_{\mathrm{rad.}}$, and $\epsilon_{\mathrm{rad.}}$ their selection efficiencies in a given energy window. The number of background events is therefore given, for the ^{208}Tl and ^{214}Bi internal contaminations, as

$$N_{\mathrm{rad.}}^m = A_{\mathrm{rad.}}^m \epsilon_{\mathrm{rad.}}^m \times m \times t \,, \tag{3.3}$$

where $A_{\mathrm{rad.}}$ is given in Bq/kg. Similarly, for the ^{222}Rn background,

$$N_{\mathrm{rad.}}^V = A_{\mathrm{rad.}}^V \epsilon_{\mathrm{rad.}}^V \times V \times t \,, \tag{3.4}$$

with $V = 15.3$ m^3 the total tracker volume, and $A_{\mathrm{rad.}}$ represents here a volumic activity, given in Bq/m^3.

As we said, all equations from Eq. (3.1) to (3.4), are valid for a given energy range $[E_{\min};E_{\max}]$. To find the optimal energy interval for the search of the $0\nu\beta\beta$ decay, that is to say the one maximising the limit on $T_{1/2}^{0\nu}$, we must study the influence of the variations of $E_{\min}$ and $E_{\max}$ bounds on the final sensitivity. On Fig. 3.1, we observe that beyond the energy sum of 3 MeV, the total number of background events is highly reduced, and the ^{208}Tl background dominates, with 0.03 count expected for E> 3.2 MeV. This is why the upper limit $E_{\max}$ of the energy interval has only a limited impact on the search for the best ROI. It is then natural to study mainly the influence of the upper limit $E_{\min}$. In that purpose, the selection efficiencies, entering in the calculation of the $T_{1/2}^{0\nu}$ upper limit, are presented in Fig. 3.2, as a function of the lower bound $E_{\min}$. We remind the selection efficiency ϵ is the ratio of the number of selected events, to the number of simulated ones. As a matter of fact, the ROI would correspond to an energy range where $\epsilon_{0\nu}$ is high, and where selection efficiencies for the background are low, in order to maximise the $T_{1/2}^{0\nu}$. The variations of the limit set on $T_{1/2}^{0\nu}$ (at 90 % CL) as a function of $E_{\min}$ and $E_{\max}$ are presented in Fig. 3.3. We found that, for the demonstrator exposure, with ^{82}Se sources, with a 25 Gauss magnetic field, and for the specified background activities, the best ROI is [2.7;3.15] MeV. As expected, the upper bound does not impact the results for $E_{\max} > 3.15$ MeV, so this value is kept, in order to enter into a future more general study, taking
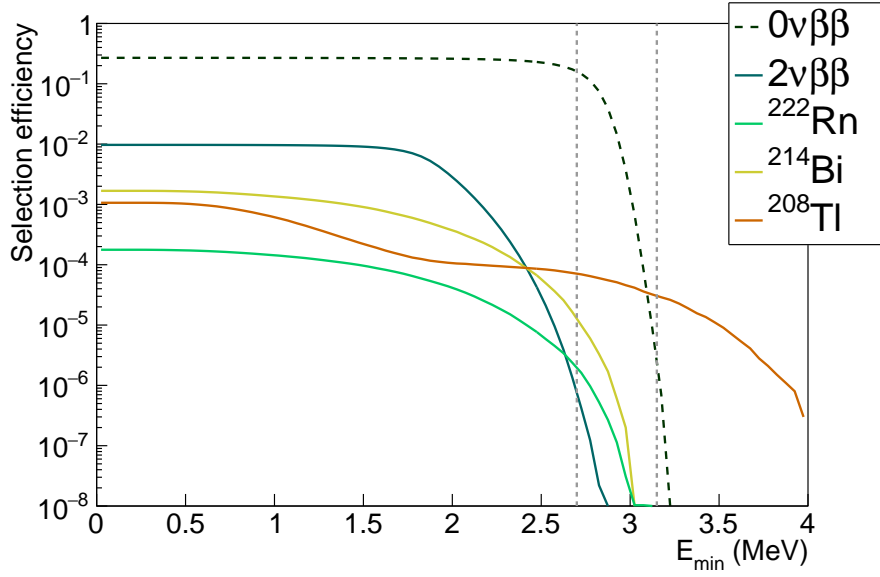
Figure 3.2: Efficiency spectra as a function of E > E$_{min}$, for the $0\nu\beta\beta$ signal (dashed black line) and for the main backgrounds (plain lines). The two vertical grey lines represent the final ROI optimised for the case of the demonstrator, taken the specified isotope activities.

into account the external background of the experiment, which extend at high energies. In the optimised [2.7;3.15] MeV energy range, the sensitivity expected for the SuperNEMO demonstrator stands at

$$T_{1/2}^{0\nu} > 5.7 \times 10^{24}\,\text{y} \qquad (90\%\text{CL})\,. \tag{3.5}$$

This result is compatible with previous SuperNEMO analysis [9].

3.3.2 Limit on the effective neutrino mass

The decay rate for the light Majorana exchange mechanism is given by:

$$(T_{1/2}^{0\nu})^{-1} = g_A^4 G^{0\nu} |M^{0\nu}|^2 \left| \frac{m_{\beta\beta}}{m_e} \right|^2 . \tag{3.6}$$

where $G^{0\nu}$ is the two particles phase space factor, depending on $Q_{\beta\beta}$ and Z the number of protons, $M^{0\nu}$ is the nuclear matrix elements for the $0\nu\beta\beta$ process, and $m_{\beta\beta}$ is the effective Majorana neutrino mass, defined as

$$\langle m_{\beta\beta} \rangle = \left| \Sigma_i m_i U_{ei}^2 \right| , \tag{3.7}$$

where m_i are the neutrino masses, and U_{ei}^2 is the mixing matrix. Therefore, the effective mass takes into account the neutrino mixing. Consequently, observing the $0\nu\beta\beta$ decay would not only prove the Majorana nature of neutrinos but, assuming the mass mechanism, could also help constraining the absolute neutrino masses. Given g_A, $G^{0\nu}$ and $M^{0\nu}$ [17][18][19][20][21][22][23][24][25][26], we find the SuperNEMO demonstrator could reach a limit on the effective neutrino mass of

$$\langle m_{\beta\beta} \rangle = [0.24 - 0.47]\,\text{eV}\,. \tag{3.8}$$

29

x 10^{24} (y)

E$_{max}$ (MeV)

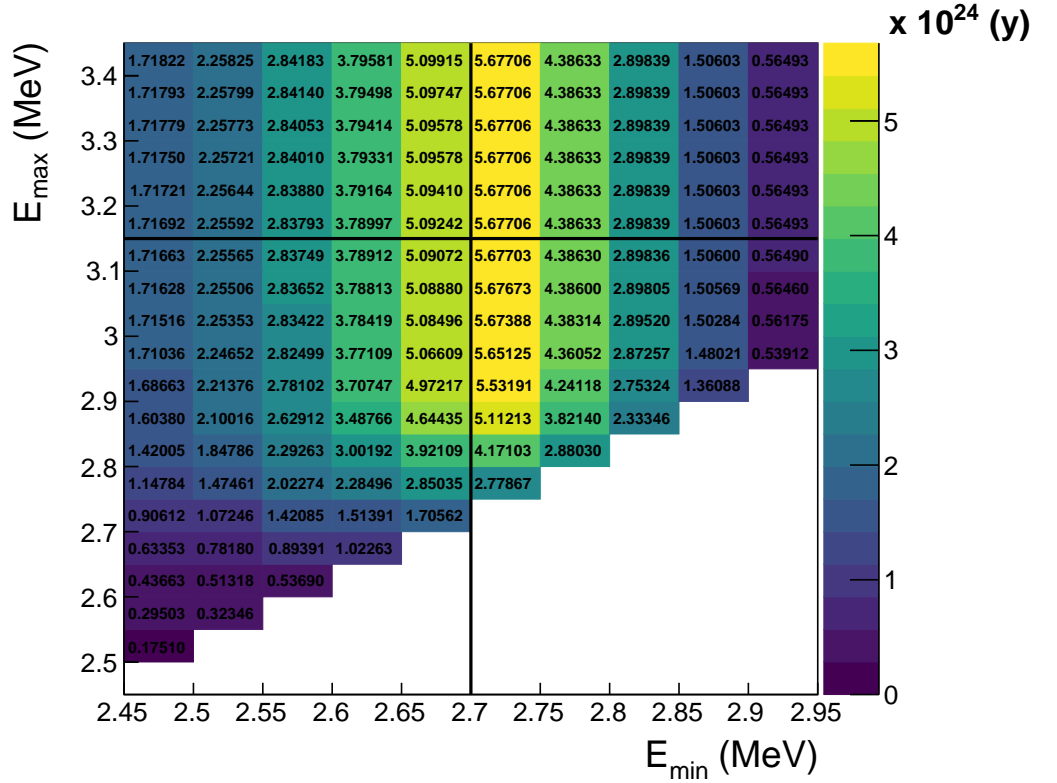|									
1.71822	2.25825	2.84183	3.79581	5.09915	5.67706	4.38633	2.89839	1.50603	0.56493
1.71793	2.25799	2.84140	3.79498	5.09747	5.67706	4.38633	2.89839	1.50603	0.56493
1.71779	2.25773	2.84053	3.79414	5.09578	5.67706	4.38633	2.89839	1.50603	0.56493
1.71750	2.25721	2.84010	3.79331	5.09578	5.67706	4.38633	2.89839	1.50603	0.56493
1.71721	2.25644	2.83880	3.79164	5.09410	5.67706	4.38633	2.89839	1.50603	0.56493
1.71692	2.25592	2.83793	3.78997	5.09242	5.67706	4.38633	2.89839	1.50603	0.56493
1.71663	2.25565	2.83749	3.78912	5.09072	5.67703	4.38630	2.89836	1.50600	0.56490
1.71628	2.25506	2.83652	3.78813	5.08880	5.67673	4.38600	2.89805	1.50569	0.56460
1.71516	2.25353	2.83422	3.78419	5.08496	5.67388	4.38314	2.89520	1.50284	0.56175
1.71036	2.24652	2.82499	3.77109	5.06609	5.65125	4.36052	2.87257	1.48021	0.53912
1.68663	2.21376	2.78102	3.70747	4.97217	5.53191	4.24118	2.75324	1.36088	
1.60380	2.10016	2.62912	3.48766	4.64435	5.11213	3.82140	2.33346		
1.42005	1.84786	2.29263	3.00192	3.92109	4.17103	2.88030			
1.14784	1.47461	2.02274	2.28496	2.85035	2.77867				
0.90612	1.07246	1.42085	1.51391	1.70562					
0.63353	0.78180	0.89391	1.02263						
0.43663	0.51318	0.53690							
0.29503	0.32346								
0.17510									

E$_{min}$ (MeV)

Figure 3.3: Two-dimensional histogram showing the evolution of the $T_{1/2}^{0\nu}$ value as a function of the lower and upper energy bounds. The maximal upper limit of $T_{1/2}^{0\nu} > 5.7 \times 10^{24}$ y (90% CL) is retained, in the [2.7;3.15] MeV region of interest.

Although this limit is not competitive with other current $0\nu\beta\beta$ experiments, it proves that SuperNEMO's technology would benefit from being adapted to larger scales.

In this section, we presented the general procedure leading to an optimised result on the $T_{1/2}^{0\nu}$ limit, and gave a result for the SuperNEMO demonstrator compatible with the previous studies led by the collaboration. Thereafter, we discuss the results obtained for different detector exposures (demonstrator and final detector), and different internal background activities. Also, and this is the main purpose of this study, we discuss the influence of the presence of the magnetic field on the final detector's sensitivity.

3.4   Impact of sources contamination levels on the sensitivity

We study the impact of the isotope contamination levels (inside the source foils, as well as on the tracker's wires) on the $0\nu\beta\beta$ sensitivity. We also optimise additional event selections aimed at improving it.

3.4.1 Contamination levels

From BiPo and SuperNEMO collaboration measurements (Sec. 2.2.1), we know that the targeted ^{208}Tl level is not reached, being almost 27 times higher than expected, with $\mathcal{A}^{\mathrm{Tl}} = 54\ \mu$Bq/kg [26 - 102]. We also know that the ^{214}Bi contamination is not greater than 290 μBq/kg. If, unfortunately, this upper limit was reached, we would expect 1.6×10^5 internal Bismuth events in the total energy range. Fortunately, the Radon contamination inside the wire chamber does not exceed the specifications. In Sec. 3.3, we developed the general procedure allowing to set a 90% confidence interval limit on $T_{1/2}^{0\nu}$. For the demonstrator, supposing the specified activities are reached, the demonstrator would achieve a sensitivity of 5.7×10^{24} years on the searched decay, in 2.5 years of data acquisition, with 7 kg of ^{82}Se. This sensitivity could be affected by the higher-than-specified levels of internal contaminations measured by BiPo.

In this sub-section, four distinct levels of internal contaminations are considered:

- the *zero activities* case, a hypothetical case where the source foils and the tracker are non contaminated at all by natural isotopes,

- the *specified activities* case, were the targeted level of contaminations would have been reached,

- and two *measured* cases, that takes into account the measured levels and limits on the contaminations at 90% CL. Indeed, as the ^{214}Bi activity is provided by BiPo measurements as an upper limit, it is possible for this level to be lower than 290 μBq/kg. We therefore choose to present the results either for sources that would not be contaminated by this isotope (the *without ^{214}Bi* case), or considering that the activity reached is 290 μBq/kg (*with ^{214}Bi*).

The fact that we are showing results for a hypothetical zero isotope contamination is to illustrate an important phenomenon about the Feldman-Cousins statistics employed to determine the number of excluded signal events, $N_{0\nu}^{\mathrm{excl.}}$, given the number of observed background events (defined from Eq. (3.2) to Eq. (3.4)).

Clarifications on Feldman-Cousins statistics When the expected number of background events is negligible (which is the case for the zero and specified levels), the probability p to observe n_s signal events, expecting s events, is given by the Poisson distribution

$$p = \frac{e^{-s}s^{n_s}}{n_s!}\,. \tag{3.9}$$

Let's now put ourselves in the situation where no signal event is observed - that is what we assume to put an upper limit on the $0\nu\beta\beta$ half-life. Then $n_s \to 0$, and $p \to e^{-s}$. If zero signal event is *observed*, it is uncorrect to assume that zero signal events were *produced* during the experiment. We only can say that no signal event has been observed *a priori*. To account for this particular case, the quantity s should no longer be viewed as the number of expected signal events, but as the

number of excluded signal events, $N_{0\nu}^{\text{excl.}}$. In the end, for a negligible expected number of background events, and no signal event observed, we can set an upper limit on the number of excluded signal events, excluding values for which $p < \alpha$. Taking a 90% confidence interval, that is to say $\alpha = 10\%$, we obtain $s \leq 2.303$.

We show in Fig. 3.4 the 90 % CL $T_{1/2}^{0\nu}$ limit for the four contamination levels condidered, as well as the corresponding chosen regions of interest. As
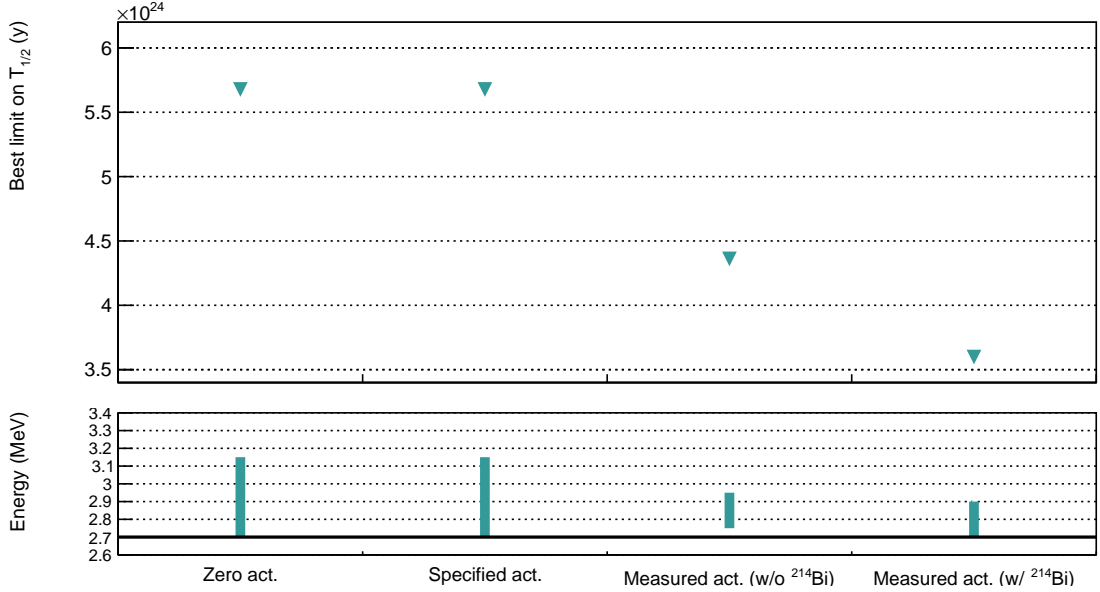

Figure 3.4: The 90% CL limit on the $0\nu\beta\beta$ half-life (top pad), and the corresponding ROI (bottom pad), as a function of the contamination level considered. For the *zero activities* case, we consider hypothetical contamination levels where $\mathcal{A}^{\text{Bi}} = \mathcal{A}^{\text{Tl}} = 0$ Bq/kg. The *specified activities* are presented in Tab. 2.1. The *measured activities*, provided by the BiPo detector [27], are presented in the same table. We consider successively a null ^{214}Bi contamination (*measured act. w/o ^{214}Bi*), or equals to the 290μ Bq/kg upper limit (*measured act. w/ ^{214}Bi*).

expected from the previous conclusions given on the Feldman-Cousins statistics, no difference is observed in terms of half-life limits, or ROI, between the zero and specified activity cases. Now considering the two measured activity cases, the sensitivity is decreased compared with the specified case. Indeed, the number of background events in the ROI is no more negligible, and influence significantly the value of $T_{1/2}^{0\nu}$, decreasing the experiment's sensitivity by 23% (without ^{214}Bi) and 37% (with ^{214}Bi).

Tab. 3.2 summarises the expected number of background for each non-zero contamination case presented in Fig. 3.4. The ROI chosen for each activity is optimised, following the technique explained in Sec. 3.3. A direct consequence of the statement on Feldman-Cousins statistics is that, considering the background levels for the two first cases are negligible (or null) in the region of interest, they both reach this limit of 2.303 on the excluded number of signal events. For the two mesaured activities cases considered, the expected number of background events increases, although the narrow ROI for the case without ^{214}Bi limits it. Indeed,

Activity ROI	Specified [2.7;3.15] MeV	Measured (w/o ^{214}Bi) [2.75;2.95] MeV	Measured (w/ ^{214}Bi) [2.7;2.9] MeV
$\epsilon_{0\nu}$ (%)	14.7	11.3	14.3
$2\nu\beta\beta$	0.418	0.122	0.418
^{208}Tl	0.0475	0.688	0.699
^{214}Bi	0.0546	0	1.55
^{222}Rn	0.292	0.173	0.287

Table 3.2: Expected number of background events in the $2e$ topology, in the optimised ROI, for the SuperNEMO demonstrator (17.5 kg.y). The selection efficiency of $0\nu\beta\beta$ events, $\epsilon_{0\nu}$, is also given.

both region of interests are highly reduced, especially for the case without ^{214}Bi, where the lower bound is increased from 2.7 to 2.75 MeV. As this 50 keV wide energy region is populated with a non-negligible number of background events, this change in E_{min} usefully reduces the $2\nu\beta\beta$ background contribution, thereby limiting the increase of total expected number of background.

The degradation of the limit on the $0\nu\beta\beta$ half-life with the level of contamination remains acceptable. However, we can try improving the situation by exploring new background rejection techniques. This would be especially useful for the final detector case, where a slight increase in internal contaminations could be highly harmful, all the more so as the upper limit given for ^{214}Bi turns out to be the true contamination level.

3.4.2 Optimisation of the event selection

The measured level of ^{208}Tl isotope inside the source foils is greater than the specifications. Moreover, an upper limit, higher than the specified level for SuperNEMO, has been set by the BiPo detector, regarding the internal ^{214}Bi level. Consequently, we can imagine implementing a tighter selection to reject more background. Most of the double beta experiments are only sensitive to the total electron energy sum. The unique SuperNEMO tracko-calo technology confers the experiment the ability to characterise single particles (individual energies, emission angles...). Based on previous studies [9] [29], *topological cuts*, relying on these additional observables, have been set up. They are especially designed to reject events where the two electrons are not emitted simultaneously, or from the same location on the source foils.

The internal probability Based on time-of-flight (TOF) computation, the internal probability (P_{int}) is derived from the internal χ^2 (see details in Sec. 2.5.1). In Fig. 3.5 are presented the internal probability spectra for the $0\nu\beta\beta$ signal and all background processes, after the first-order selections. These distributions are normalised to the double beta half-lives, and the nominal activities. Equivalent distributions, but with different ^{214}Bi and ^{208}Tl contamination levels, can be derived for the case of measured activities. The internal probability distributions for the $0\nu\beta\beta$ and $2\nu\beta\beta$ processes follow the expected flat distribution for electrons
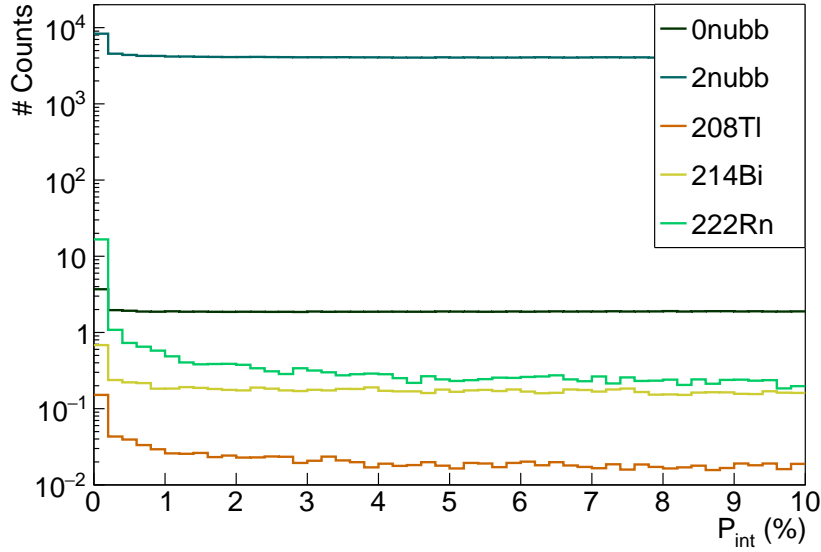
Figure 3.5: Internal probabilities for all processes. First-order cuts have been applied. $\beta\beta$ distributions are normalised to the half-lives, and background processes are normalised to the specified activities.

emitted simultaneously from the source. As internal Bismuth disintegration actually takes place inside the sources, the ^{214}Bi distribution is also flat. The same could have been assumed for Thallium, however, the distribution is distorted at low internal probabilities. This might be explained by the existence of a metastable excited state ($\tau_{1/2} = 294ps$) of the daughter nuclei, which would slightly delay the second electron emitted via internal conversion. This feature is addressed in detail in Chap. 4. The Radon, being a non-internal background, presents a peak at low internal probabilities.

We want to evaluate the influence of a cut-off on the simulations using internal probability as a rejection criterion: simulated events are selected for P_{int} values upper than a given limit. The standard value applied in NEMO-3 analyses was $P_{int} > 4$ %. We wish to establish the most adequate P_{int} selection level for the SuperNEMO demonstrator. For each internal probability cut-off applied to the simulations, we evaluate the $T^{0\nu}_{1/2}$ at a 90 % confidence interval, as well as the best ROI. The internal probability value that will be chosen will be the one that maximises the sensitivity, and depends on the internal level of contamination. To better understand this optimisation, let us present the $\epsilon_{0\nu}$ values for each P_{int} selection case, in Fig. 3.6a, both for the specified and measured contamination levels. For the latter, we assume the Bismuth upper limit of 290 μBq/kg activity is reached. As expected, in both cases, the $\epsilon_{0\nu}$ selection efficiency globally decreases with the P_{int} cut-off applied. However, for the measured contamination case, we observe a slight increase of the $0\nu\beta\beta$ selection efficiency, for $P_{int} > 1$ %. Fig. 3.6b, showing the variations of the regions of interest as a function of the P_{int} rejection criterion, allow to understand this observation. For the measured activities case, when the minimal acceptable P_{int} is changed from 0 to 1 %, then the ROI upper bound increases from 2.9 to 3.05 MeV. Usually, the variation of

(a) $0\nu\beta\beta$ selection efficiency.

(b) ROI optimisation.

(c) Limit on $T_{1/2}^{0\nu}$.

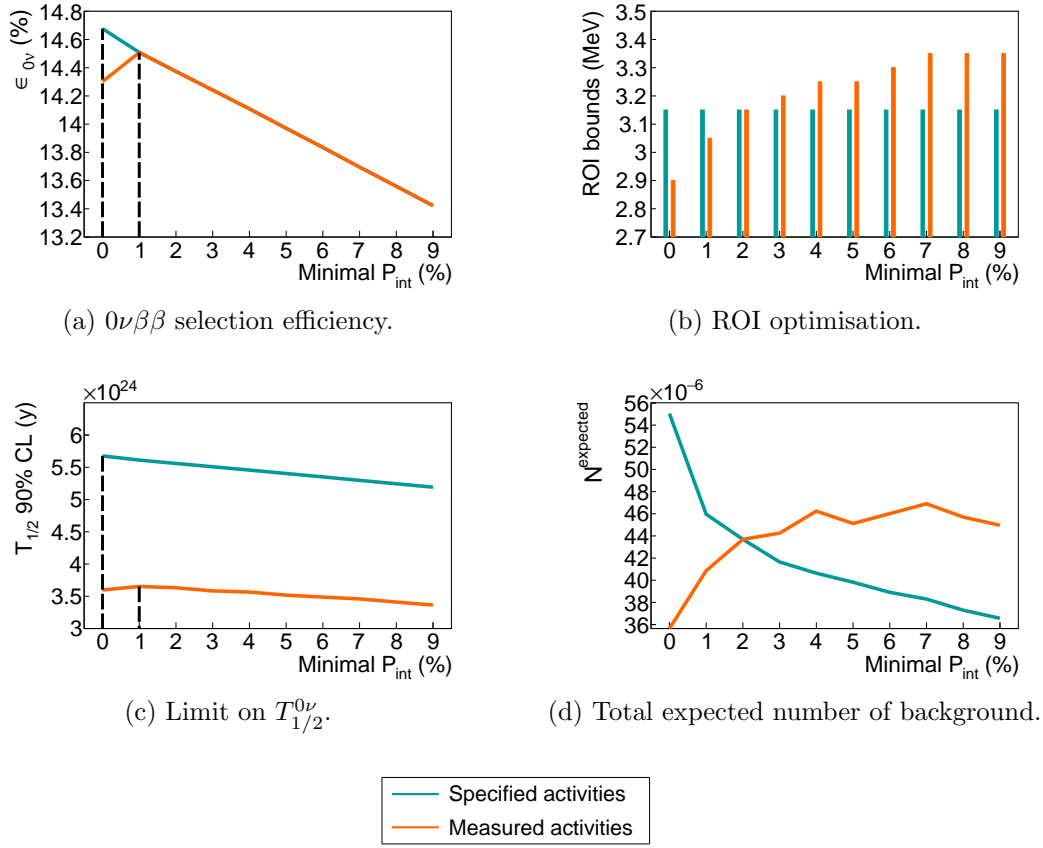(d) Total expected number of background.

Figure 3.6: The $0\nu\beta\beta$ selection efficiency, $\epsilon_{0\nu}$ (a), evolution of the region of interests (b), best limits set on $T_{1/2}^{0\nu}$ at 90% CL (c), and total number of expected background (d), as a function of the cut-off applied on internal probability, P_{int}. The ROI is optimised for each P_{int} value. Results are displayed for two contamination levels: the specified (blue) and the measured (orange) activities (taking into account the upper limit provided for ^{214}Bi). An exposure of 17.5 kg.y is considered. Two vertical dashed lines in (a) and (c) display the best P_{int} selections to be applied in order to improve the $T_{1/2}^{0\nu}$ sensitivity of the experiment.

this bound does not have such a great impact on the event selection. Nevertheless, in the measured activities case, for a $P_{int} > 0$ % level, the ROI is optimised at the narrow [2.7;2.9] MeV interval, where the upper bound is located in an energy region still populated by signal and bakground (see Fig. 3.4). Therefore, even small variations in this ROI has a great impact on the results, explaining the local increase in efficiency. For P_{int} selections greater than 1 %, we come back in cases where the upper limit of the ROI no longer has an impact on $\epsilon_{0\nu}$. For the specified ativities case, the ROI bounds are stable, not impacting the selection efficiency. In Fig. 3.6d, the total expected number of background is displayed. For specified activities, this number decreases with the P_{int} cut-off, as the ROI is stable. However, this number tends to reach a plateau after increasing, again explained by the ROI variations.

As the limit set on $T_{1/2}^{0\nu}$ depends directly on $\epsilon_{0\nu}$, the variations presented in Fig. 3.6a fully explain the results displayed in Fig. 3.6c, presenting the evolution

of $T_{1/2}^{0\nu}$ with the internal probability selection level. The sensitivities displayed for a 0% cut-off on P_{int} of course correspond to the results given in Fig. 3.4. The main conclusion is that this rejection criterion has only a limited impact on the improvement of $T_{1/2}^{0\nu}$ sensitivity, because of the very low contamination levels considered. Indeed, paradoxically, the selection on internal probability worth it only if there is enough background events to be rejected. The former 4 % value recommended by the NEMO-3 analysis is then too high for the SuperNEMO source contamination.

NEMO-3 analyses also used the distance between the reconstructed vertices on the source foils as a background rejection criterion. As we shown that the additional P_{int} cut-off is poorly adapted for the low activities of SuperNEMO sources, it is interesting to know if we can improve the results by using this second selection.

Vertices distance As discussed in Sec. 3.2, an electron is defined as a reconstructed track inside the wire chamber, with one extremity on a calorimeter block, and another on a source foil. Therefore, the $2e$ topology involves two distinct calorimeter hits, two reconstructed tracks, and two foil vertices. Thanks to the trajectory fitting algorithm, we have access to the (Y, Z) coordinates of the latter, and by extension, to the distance between them. In the previous studies, the choice was made to look at the effect of this selection, separately on the Y (perpendicular to the wires) and Z (parallel to the wires) directions. We choose to follow the same approach, and we give the results for a cut along the Z axis, but the conclusions would remain valid for the Y direction. Fig. 3.7 shows the distributions of the absolute value of the distance between foil vertices for each process studied. We would use this information in order to maximise the double β decays to be selected, while rejecting natural isotope disintegrations.

Fig. 3.8 displays the limit set on $T_{1/2}^{0\nu}$ as a function of this event selection, allowing to study the impact of the vertices distance cut-off on the final sensitivity. In the same way as previous paragraph, we study the influence of the level of contaminations by showing results for the two specified and measured activities. The two distributions reach a plateau, corresponding to the sensitivities achieved with the first-order cuts (Fig. 3.4). Regardless of the level of contamination, the number of background events is too low in the ROI for the $|\Delta Z|$ cut-off to be worthwhile. Therefore, the cut-off only degrades the sensitivity, as does the selection on internal probability. The same conclusions apply to the $|\Delta Y|$ cut-off.

However, such a cut-off could be useful for rejecting unexpected background (coincidence between independent events, for instance). For example, we note that a cut-off at $|\Delta Z| < 80$ mm does not significantly degrade sensitivity. In practice, a selection on vertex distance will always be applied, even if it is very loose.

The idea of having implemented these two selections (on the internal probability and on the distance between vertices) comes from a previous NEMO-3 analysis on the background rejection. For the SuperNEMO demonstrator case, the levels of contaminations we are dealing with is remarkably low for most of the topological cut-offs to be worth applying. However, in practice, appling loose topological
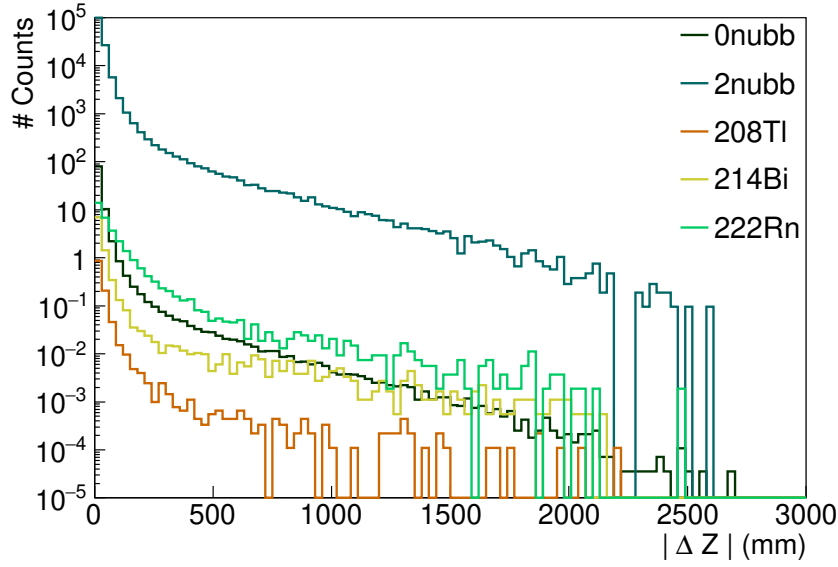
Figure 3.7: Distance along the Z direction between the vertices of the 2 reconstructed electrons, for each process considered. The $2\nu\beta\beta$ spectrum is normalised to $T_{1/2}^{2\nu} = 9.39 \times 10^{19}$ y, and ^{208}Tl, ^{214}Bi and ^{222}Rn backgrounds are normalised to the nominal activities. The amplitude of the $0\nu\beta\beta$ is arbitrarily set at the limit obtained with NEMO-3. No energy cut is applied.
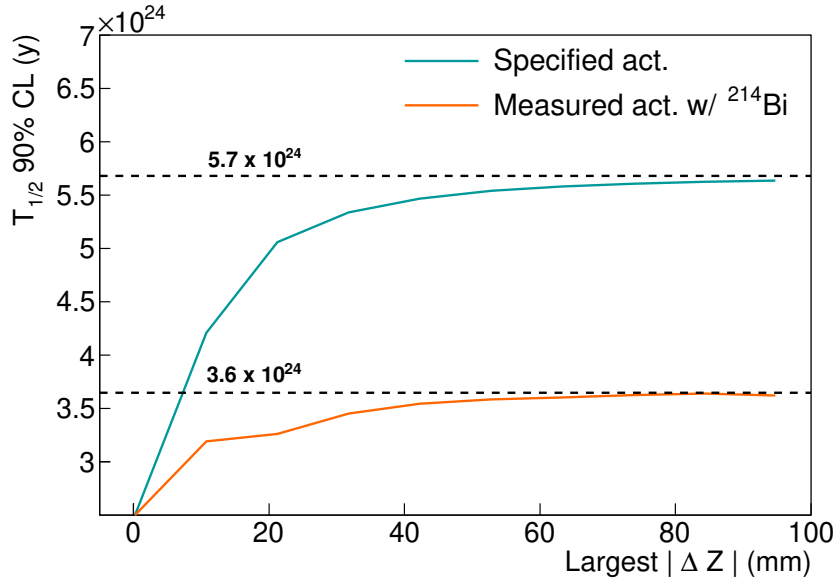

Figure 3.8: Limit reached for $T_{1/2}^{0\nu}$ (90% CL), as a function of the cut-off applied on the Z distance between vertices, $|\Delta Z|$. Results are displayed for specified (blue), and measured contaminations taking into account the upper limit for ^{214}Bi activity (orange). The ROI is optimised for each P_{int} value. No improvement in sensitivity is obtained with this event selection.

selections on the data remains necessary, especially to reject external background

events. The minimal cut-off level to be applied is $P_{int} > 4\%$ and $|\Delta Z| < 80$ mm (samely for $|\Delta Y|$).

For future studies, it is useful to give the efficiencies of these loose selections, for the signal and for each background considered (Tab. 3.3a), as well as the expected number of background in the ROI (Tab. 3.3b).

Cut-off	First-order cuts (%)	Internal probability (%) $P_{int} > 4\%$	Vertex distance (%) $|\Delta Z| < 80$ mm
$0\nu\beta\beta$	26.9	25.3	24.7
$2\nu\beta\beta$	9.15	8.56	8.21
^{208}Tl	0.106	0.0889	0.0846
^{214}Bi	0.168	0.151	0.144
^{222}Rn	0.0177	7.91×10^{-3}	5.34×10^{-3}

(a) Selection efficiencies (number of selected $2e$ topologies compared with the total number of simulated decays), for the three levels of selection (first-order, P_{int} and vertex distance), in the full energy range.

Activity	Specified		Measured (w/ ^{214}Bi)	
Cut-off	$P_{int} > 4\%$	$|\Delta Z| < 80$ mm	$P_{int} > 4\%$	$|\Delta Z| < 80$ mm
ROI (MeV)	[2.7;3.15]	[2.7;3.15]	[2.7;3.25]	[2.7;3.3]
$\epsilon_{0\nu}$ (%)	14.1	13.9	14.1	13.9
$2\nu\beta\beta$	0.392	0.383	0.392	0.383
^{208}Tl	0.0338	0.0323	1.08	1.09
^{214}Bi	0.0491	0.0491	1.42	1.42
^{222}Rn	0.115	0.0782	0.115	0.0782

(b) Expected number of background events in the optimised ROI, for successive application of topological selections. The selection efficiency of $0\nu\beta\beta$ events in the ROI, $\epsilon_{0\nu}$, is also given. Specified and measured activities (taking into account the upper limit for ^{214}Bi contamination) are considered. The SuperNEMO demonstrator exposure of 17.5 kg.y is taken.

Table 3.3:   The selection efficiencies and expected number of background events for the topological selections.

Regions of interest are optimised for each selection. The topological cuts have a huge impact on Radon, as they are especially designed to reject non-internal events. They are also efficient in rejecting Thallium internal events, because of the existence of a metastable exited state, described earlier. A special technique to reject efficiently ^{208}Tl bacground is also addressed in Chapter 4.

After the topological cut-off optimisation, the SuperNEMO demonstrator would reach a sensitivity of $T_{1/2}^{0\nu} > 5.6 \times 10^{24}$ y, and a corresponding effective neutrino mass of $\langle m_{\beta\beta} \rangle < [0.25 - 0.48]$ MeV. After looking at the effect of contaminations on the sensitivity, we review the influence of the magnetic field inside the detector.

3.5 Impact of the magnetic field on the sensitivity

The SuperNEMO demonstrator was originally designed with a copper coil, similarly to NEMO-3, delivering a magnetic field inside the tracker volume, aiming to provide an electron/positron discrimination. This 25 Gauss magnetic field is high enough to bend the trajectory of the few MeV electrons and positrons of interest for SuperNEMO, without too strongly preventing them from reaching the calorimeter. In practice, this magnetic field is mainly used to identify and reject the electron-positron pairs created by high energy γ's, themselves emitted after a neutron capture. However, as explained in sub-section 3.1.3, we choose to not consider the contribution of this external background. We therefore focus on evaluating the influence of the presence of the magnetic field on the rejection of internal and wire chamber backgrounds.

3.5.1 Simulations of the magnetic field inside the demonstrator and reconstructed track fit

In order to study the influence of the magnetic field on the ^{82}Se $0\nu\beta\beta$ sensitivity, the simulations and reconstructions of decays described in Sec. 3.1 have been performed in two different conditions.

- Simulations with a uniform 25 Gauss magnetic field (following recommendations [9]). Results about the final sensitivity achieved in this condition have already been presented earlier in this chapter. The possible variations of the field intensity, mainly due to the calorimeter magnetic shields, are not taken into account for these simulations. This will be discussed in sub-section 3.5.4.

- Simulations where the magnetic field is turned off.

Each magnetic field condition has the same number of simulated events, as summed up in Tab. 3.1. Depending on the case considered, the electrons do not have the same trajectory curvature. In the first uniform on-field case, the best track fit is performed by an helix. In the second off-field case, the trajectory of an electron is modelised by a straight line. The fitting algorithm is thus modified to match line trajectories.

3.5.2 Impact of the magnetic field on signal and background selections

Among the various event selection criteria considered in Sec. 3.2, the one on the trajectory curvature is of primary importance with regard to the influence of the magnetic field on the final sensitivity of the detector. Indeed, when the magnetic field is switched on, the charged particles of few MeV (as electrons and positrons) have curved trajectories. A particle is then identified as an electron when the trajectory fitting results in a negative curvature. When the magnetic

field is switched off, the trajectory of the charged particles takes place in a straight line[4]. This last selection criterion on the track curvature is then no longer applied. Consequently, the number of identified $2e$ topologies, selected by the first-order cuts, are increased, for the signal and background simulated events. To illustrate this effect, we give in Fig. 3.9 the selection efficiencies of signal and background as a function of the $2e$ total energy, for the two cases of magnetic field presented above. The two coloured stripes represent the corresponding region of interests,
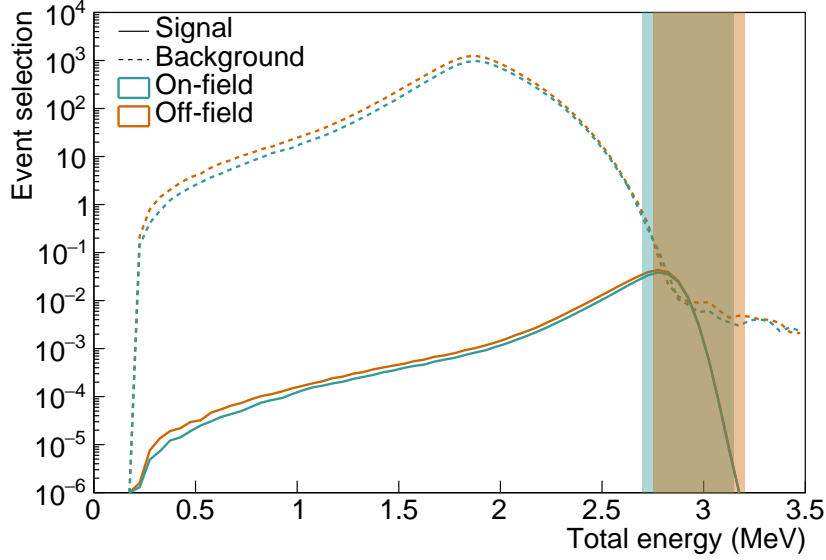

Figure 3.9: The $0\nu\beta\beta$ selection efficiency (plain line), and expected number of background events (dashed line), as a function of the $2e$ energy, for the on-field (blue) and the off-field (orange) cases. Results are presented for a 17.5 kg.y exposure, for the specified isotope activities. The two corresponding region of interests are also displayed by coloured stripes. Here no optimised topological cut-offs have been applied.

of [2.7;3.15] MeV for the *on-field* case, and [2.75;3.2] MeV for the *off-field* case. These results are presented for the specified contamination levels, but remain valid in all cases. We clearly notice that, for the total energy interval [0;4] MeV, the number of signal and background selected events is higher in the off-field case, which confirms what we were saying above.

Following Eq. (3.1), the ratio $\epsilon_{0\nu}/N_{0\nu}^{\text{excl.}}$ in the ROI impacts the final sensitivity. Nevertheless, as we explained in the previous section, the low contamination level considered causes $N_{0\nu}^{\text{excl.}}$ to reach the 2.303 limit. Thus, only variations of $\epsilon_{0\nu}$ in the ROI, between on-field and off-field cases, are the source of modifications on the final sensitivity. Integrating $\epsilon_{0\nu}$ over the ROI, we obtain $\epsilon_{0\nu}^{\text{on-field}} = 0.15\% > \epsilon_{0\nu}^{\text{off-field}} = 0.12\%$. The selection efficiency for the on-field case is favoured by the lower bound of the ROI. In fact, the further this lower bound is shifted towards lower energies, the greater the selection efficiency. Besides, slight variations of the

---

[4]In saying this, we do not take into account possible deviations in the trajectory of the particles, due in particular to multiple scattering in the tracker.

upper bound have almost no impact. As expected, this results in a decrease in sensitivity when the field is switched off, giving

$$T_{1/2}^{0\nu} > 4.80 \times 10^{24} \, \mathrm{y} \qquad (90\%\mathrm{CL}) \, (\text{off-field}). \qquad (3.10)$$

We present in Tab. 3.4 the selection efficiencies of the signal and backgrounds, in the ROI, for the two field cases. We principally notice that the ^{208}Tl and ^{222}Rn

Process	On-field [2.7;3.15] MeV	Off-field [2.75;3.2] MeV
$\epsilon_{0\nu}$ (%)	14.7	12.4
$2\nu\beta\beta$	0.418	0.0653
^{208}Tl	0.0475	0.0600
^{214}Bi	0.0546	0.0452
^{222}Rn	0.292	0.553

Table 3.4: Expected number of background events in the optimised ROI, for the SuperNEMO demonstrator (17.5 kg.y), for specified activities. The selection efficiency of $0\nu\beta\beta$ events, $\epsilon_{0\nu}$, is also given. The two on- and off-field cases are compared.

contributions are higher in the second case. As concluded in Sec. 3.4, topological selections are especially efficient in rejecting these two backgrounds. Therefore, the application of these additionnal cut-offs, for the off-field case, could be interesting, in order to increase the sensitivity. Following the work presented in the previous section, we optimise these selections for the particular off-field case, both for the specified and measured contamination levels[5]. The results in the sensitivity are summarised in Fig. 3.10. The left part of the panel gives information on the evolution of sensitivity, when only the first-order cut-offs are applied. We come back to the conclusions given above: when the magnetic field is switched-off, we lose sensitivity, regardless of the level of contamination considered. On the right side of the figure, we present the results when the topological cuts are applied. For the on-field case, the addition of these selections have almost no effect on the sensitivity, as concluded in sub-section 3.4.2. However, as predicted, we are beginning to see the usefulness of these selections in the off-field case, as a higher number of ^{208}Tl and ^{222}Rn events passed the first-order selections. For instance, for the specification case, $T_{1/2}^{0\nu}$ goes from 4.80×10^{24} y to 6.1×10^{24} y, an improvement of $\sim$ 30%. In Tab. 3.5 are presented the expected number of background events in the ROI for the off-field condition. The influence of topological cut-offs is presented, for the specified and measured activities (taking into accouont the upper limit for the ^{214}Bi contamination).

Finally, even if the absence of the magnetic field has the effect of reducing the sensitivity to the $0\nu\beta\beta$ decay, topological cuts allow this effect to be compensated for, making it possible to reach higher values of $T_{1/2}^{0\nu}$.

---

[5]As done in sub-section 3.4.2, for the Bismuth measured contamination, we consider here the upper limit where $\mathcal{A}^{\mathrm{Bi}} = 290 \, \mu\mathrm{Bq/kg}$.
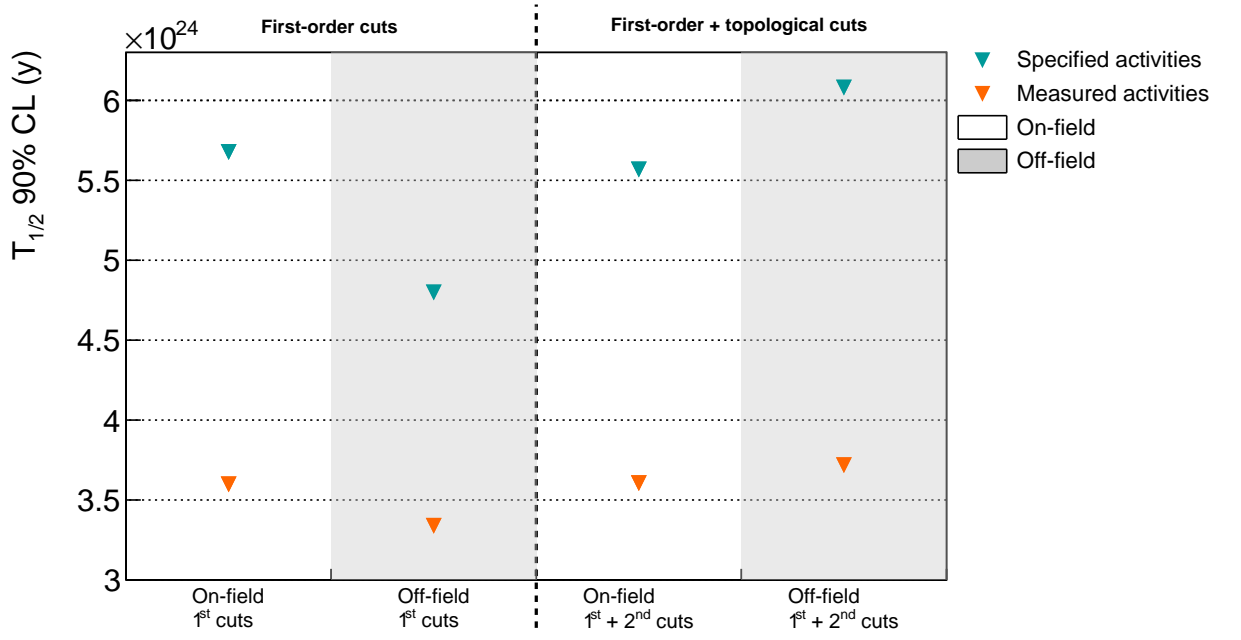
Figure 3.10: $T_{1/2}^{0\nu}$ (90% CL) considering various conditions: on- and off-field (white and gray stripes), first-order and addition of topological cut-offs (left/right parts of the panel), specified and measured activities (blue and orange triangle markers). The measured activities are $\mathcal{A}^{\text{Tl}} = 54~\mu\text{Bq/kg}$, $\mathcal{A}^{\text{Bi}} = 290~\mu\text{Bq/kg}$ and $\mathcal{A}^{\text{Rn}} = 0.15~\text{mBq/m}^3$.

Activity	Specified		Measured (w/ ^{214}Bi)	
Cut-off	First-order	Topological	First-order	Topological
ROI (MeV)	[2.75;3.2]	[2.7;3.2]	[2.65;2.9]	[2.7;2.9]
$\epsilon_{0\nu}$ (%)	12.4	15.7	19.1	14.8
$2\nu\beta\beta$	0.0653	0.453	1.56	0.440
^{208}Tl	0.0600	0.0506	1.01	0.613
^{214}Bi	0.0452	0.0706	2.94	1.84
^{222}Rn	0.553	0.0894	1.42	0.0689

Table 3.5: Expected number of background events in the optimised ROI, with off-field condition. The selection efficiency of $0\nu\beta\beta$ events in the ROI, $\epsilon_{0\nu}$, is also given. Exposure of the SuperNEMO demonstrator (17.5 kg.y). Specified and measured (with ^{214}Bi) activities are considered. Topological cut-offs are optimised: $\text{P}_{int} > 1\%$ and $|\Delta Z| < 80\text{mm}$ (specified activities), $\text{P}_{int} > 5\%$ and $|\Delta Z| < 80\text{mm}$ (measured activities)

3.5.3 Influence of the magnetic field on optical modules and reconstruction efficiency

In the previous sub-section, a comparative study has been lead to evaluate the influence of the presence of a magnetic field on the event selection, and thus on the final sensitivity. However, as things stand now, some features of the demonstrator are not yet implemented in the simulation software, and could have

a great impact on the results presented above. In particular, studies have been lead by the collaboration to evaluate the influence a 25 Gauss magnetic field on the optical modules, as well as on the event reconstruction [9][10].

SuperNEMO PMTs are protected from the external magnetic field by individual, cylindrical, iron shields. Unfortunately, the latter do not perfectly protect the PMTs, and a residual magnetic field is measured inside the shieldings, leading to losses in charge collected by PMTs close to 8%. This study also revealed the energy resolution would be worsened with a relative decrease of 3% of the initial value of 8% at 1 MeV. Moreover, the PMTs shieldings could themselves severely impact the shape of the field lines, as well as its strength. In fact, with a 25 Gauss magnetic field generated by the copper coil, the magnetic shields are responsible for the field strength decreasing, and barely 10 G is expected near the source foils. Worse, the magnetic field strength decreases very quickly as we get closer to the calorimeter walls where nearly 0G could be expected. The reconstruction efficiency could therefore be greatly impacted: the magnetic field intensity varying from the source foils to the calorimeter wall, electrons trajectory curvatures are not constant, and the track-fitting algorithm is less performing. A non correct description of the distribution of the magnetic field would more strongly impact low-energy electrons.

In the light of these conclusions, it could be interesting to study the evolution of the sensitivity, considering field simulations with more realistic variations inside the detector.

3.5.4 Simulations with a non-uniform magnetic field

Simulations with a 25 Gauss *mapped* magnetic field have been performed, taking into account more realistic variations of the field inside the detector [30]. Unfortunately, not all isotopes could be simulated with this magnetic field configuration. In particular, Radon, as it is present in the entire wire chamber, would have required too many additional storing resources. Thus, final conclusions on the sensitivity can't be given. However, it is possible to assess the selection efficiencies of the different processes, and thus get an idea of the influence of realistic variations of the field on the final results. Tab. 3.6 compares the selection efficiencies, for the three field cases (uniform field, mapped field and off-field), in the total energy range [0;4] MeV. The mapped field case has lower selection efficiencies, compared with uniform field simulations. As announced in the previous sub-section, the magnetic shields distorts the field intensity accross the detector. Therefore, the fitting algorithm is less performant in identifying particles with a negative curvature inside the tracker.

Tab. 3.7 presents the expected number of background events in the energy range [2.7;3.2] MeV, for simulations using the realistic mapped field. As expected, the $0\nu\beta\beta$ selection efficiency is drasticly decreased compared with the on-field case, as well as the expected number of background events.

Even if Radon simulation with such field conditions are not available, it would be interesting to have an order og magnitude for the limit that could be set on the $0\nu\beta\beta$ process, taking into account realistic variations of the field. To do so,

Field P_{int}	On $P_{int} > 4\%$	Off $P_{int} > 1\%$	Mapped $P_{int} > 4\%$
$0\nu\beta\beta$	24.7	29.3	19.1
$2\nu\beta\beta$	8.21	9.93	6.39
^{208}Tl	0.0846	0.140	0.0774
^{214}Bi	0.144	0.211	0.125

Table 3.6: Signal and background selection efficiencies of on-field, off-field and mapped-field cases, in the energy range [0;4] MeV. Specified activities are considered. The first-order and optimised topological cut-offs have been applied. For all field conditions, the selection $|\Delta Z| < 80$ mm have been applied.

	Mapped field
$\epsilon_{0\nu}$ (%)	10.4
$2\nu\beta\beta$	0.245
^{208}Tl	0.0279
^{214}Bi	0.0535

Table 3.7: Expected number of background events in the optimised energy range [2.7;3.2] MeV, for mapped field simulations. The $2\nu\beta\beta$ half-life taken as $T_{1/2}^{2\nu} = 9.39 \times 10^{19}$ y, and the nominal background activities are considered. We assume a 17.5 kg.y exposure. First-order and optimised topological cuts have been applied.

we extrapolate the expected number of Radon events in the [2.7;3.2] MeV energy range, from the ^{214}Bi one. Indeed, we postulate the ratio between these two numbers is a constant, and the on-field simulations give $N_{\text{Bi}}/N_{\text{Rn}} \sim 5$. Taking this into consideration, a limit of $T_{1/2}^{0\nu} > 4 \times 10^{24}$ y (90 % CL) would be reached with the demonstrator.

- mettre aussi un tableau du Nexp dans la ROI et préciser que ROI pas optimisée car pas de radon

- Dans le Mapped field comment sont reconstruits les trajectoires des électrons? Comme des hélices? Comme des lignes droites? Le préciser clairement dans le corps du texte. D'ailleurs tu pourrais comparer les deux.

3.6 Searching for the Neodymium-150 $0\nu\beta\beta$ decay

This study was conducted jointly with the PhD student Axel Pin, from CENBG [31]. Although we both worked on the whole of the analysis, I presented in detail, in the previous sections, the results regarding the influence of the magnetic field. Meanwhile, Axel Pin presents the possibility of changing the Selenium material by other $\beta\beta$ isotopes. Indeed, on the model of the NEMO-3 detector, which housed, among others, 6.914 kg of ^{100}Mo and 0.932 kg of ^{82}Se,

the SuperNEMO detector has the technical possibility of exchanging the source material and study several $\beta\beta$ isotopes. Especially, in the case SuperNEMO demonstrates the feasibility of a large-scale tracko-calo experiment, it would be natural to evaluate the sensitivity of SuperNEMO to the $0\nu\beta\beta$ decay of other isotopes than ^{82}Se.

3.6.1 Searching for the $0\nu\beta\beta$ of other isotopes

One of the special features of NEMO detectors is the gas chamber, designed to track charged particles. Unfortunately, this advantage is also a great inconvenience when it comes to Radon contamination. Indeed, Radon enters by diffusion or emanates from the detector materials. It is then important to select $\beta\beta$ candidates with an energy transition value above the Q_β of Radon (Q_β = 3.27 MeV). The natural isotopic abundance is another useful criterion, and typically considering only isotopic abundances greater than 2% is a good basis for making a choice. Two nuclei satisfy these two criteria: ^{96}Zr and ^{150}Nd (with respective $Q_{\beta\beta}$ values of 3.35 and 3.36 MeV and respective isotope abundance values of 2.8 and 5.6 % [32]). As the ^{150}Nd isotope has the highest $Q_{\beta\beta}$ value, the current section focuses on evaluating the SuperNEMO sensitivity to the $0\nu\beta\beta$ decay of this isotope, supposing we have several kg at our disposal.

3.6.2 Sensitivity to the $0\nu\beta\beta$ of ^{150}Nd

Until recently, Neodymium was not enrichable in large quantities by centrifugation. Recent developments have resulted in the production of several grams of enriched Neodymium, making this $\beta\beta$ isotope interesting for the search of $0\nu\beta\beta$. Thanks to that, NEMO-3 had available 37 g of ^{150}Ndwhich were recovered by the collaboration, for a possible reuse in the SuperNEMO demonstrator. The best limit for the seach for neutrinoless double β decay of ^{150}Nd was reached by the NEMO-3 detector, using 36.6 g of enriched material for 5.25 years of data acquisition. The collaboration achieved $T_{1/2}^{0\nu}$ > 2.0×10^{23} y (90 % CL), corresponding to an upper limit on the effective neutrino mass of $\langle m_{\beta\beta} \rangle$ < [1.6 − 5.3] eV. The collaboration also measured the $2\nu\beta\beta$ half-life, with $T_{1/2}^{2\nu}$ = [9.34 ± 0.22 (stat.) ± $^{0.62}_{0.60}$ (syst.)]× 10^{18} y [34].

We wish to determine the limit on the $0\nu\beta\beta$ of the ^{150}Nd that could be reached by the SuperNEMO demonstrator. We lead this study considering the specified activities given for the ^{82}Se sources are reached. We use simulations with the 25 Gauss uniform magnetic field. Fig. 3.11 presents the normalised energy distributions for the $2e$ topologies selected after application of first-order and topological selections. Signal and background selection efficiencies for ^{150}Nd sources, in the total energy range, are given in Tab. 3.8. In this energy range, the background is dominated by the $2\nu\beta\beta$ decay. The selection efficiencies of backgrounds are lower for ^{150}Nd sources than for ^{82}Se sources. This is caused by the higher number of protons in the Neodynium nucleus which induces a stronger Coulombian effect. Indeed, internal electrons are more likely to interact with the source material by Coulombian interactions, which is particularly true for
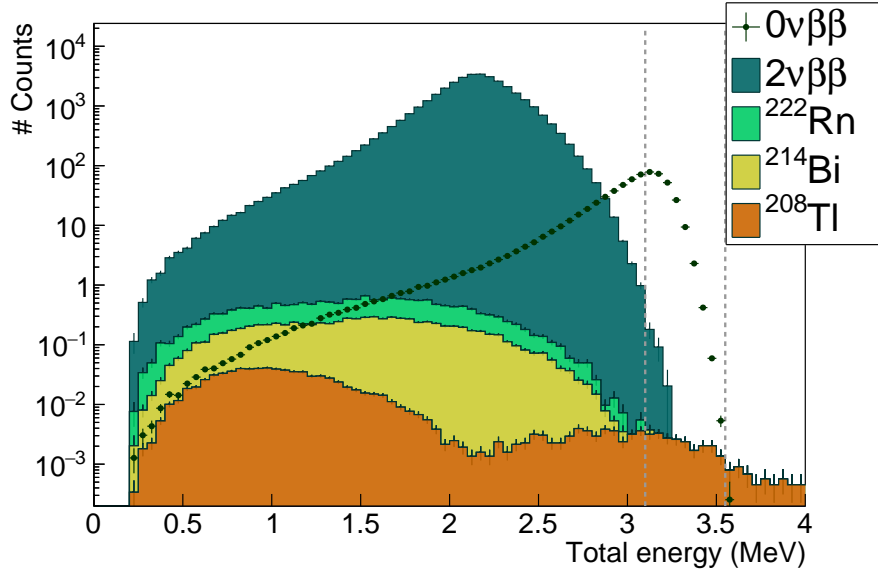
Figure 3.11: Total energy spectra for the $0\nu\beta\beta$ signal and main backgrounds, for ^{150}Nd sources. The $2\nu\beta\beta$ spectrum is normalised to $T_{1/2}^{2\nu}$ = 9.39×10^{19} y, and ^{208}Tl, ^{214}Bi and ^{222}Rn backgrounds are normalised to the nominal activities. The amplitude of the $0\nu\beta\beta$ is arbitrarily set at the limit obtained with NEMO-3. We assume a 17.5 kg.y exposure. First-order and optimised topological cuts have been applied. The ROI of [3.1;3.55] MeV is represented by to vertical dashed lines.

Process ROI	Selenium [2.7;3.15] MeV	Neodynium [3.1;3.55] MeV
$0\nu\beta\beta$	25.8	25.5
$2\nu\beta\beta$	8.21	8.11
^{208}Tl	0.0846	0.0749
^{214}Bi	0.144	0.138
^{222}Rn	5.34×10^{-3}	5.34×10^{-3}

Table 3.8: Selection efficiencies in the full energy range [0;4] MeV, for ^{82}Se and ^{150}Nd sources. First-order and optimised topological cuts have been applied.

low energy electrons. We used the same Radon simulations as for ^{82}Se sources, neglecting possible effects due to a higher proton number.

In Tab. 3.9 we give the expected number of background events in the optimised ROI [3.1;3.55] MeV. The selection efficiency of the $0\nu\beta\beta$ decay in this energy range is also given. Although the $2\nu\beta\beta$ half-life of the ^{150}Nd is lower than that of the ^{82}Se, the number of $2\nu\beta\beta$ events in the ROI remains low. Indeed, thanks to the Coulombian effects described above, this process has a limited contribution at high energy. The high energy of transition $Q_{\beta\beta}$ = 3.36 MeV of ^{150}Nd implies that the contributions of ^{214}Bi and ^{222}Rn are very small, or even zero. The $2\nu\beta\beta$ and ^{208}Tl events are therefore the majority contributors to the background. Consequently, if the choice of changing the source material with ^{150}Nd isotope, it would be

Material	Selenium	Neodynium
ROI	[2.7;3.15] MeV	[3.1;3.55] MeV
$\epsilon_{0\nu}$ (%)	14.4	10.3
$2\nu\beta\beta$	0.39	0.28
^{208}Tl	0.044	0.029
^{214}Bi	0.053	5.6×10^{-4}
^{222}Rn	0.20	0.0

Table 3.9: Expected number of background events in the optimised region of interests, for ^{82}Se and ^{150}Nd sources. The $2\nu\beta\beta$ half-life taken as $T_{1/2}^{2\nu} = 9.39 \times 10^{19}$ y, and the nominal background activities are considered. We assume a 17.5 kg.y exposure. First-order and optimised topological cuts have been applied.

conceivable to release the specifications on ^{214}Bi and ^{222}Rn backgrounds.

The SuperNEMO demonstrator, with 7 kg of material and 2.5 years of data acquisition, would achieve a $T_{1/2}^{0\nu} > 2.2 \times 10^{24}$ y sensitivity, one order of magnitude higher than the best limit ever reached. The corresponding limit on the effective neutrino mass is $\langle m_{\beta\beta} \rangle = [0.15 - 0.50]$ eV. This is a better result than for ^{82}Se sources, as the ^{150}Nd has a c.

- relire conclusion sur comparaison nb bdf attendu Se/Nd

3.7 The final detector sensitivity

The ultimate goal of the SuperNEMO demonstrator is to show that the NEMO technology is scalable to probe unprecedented half-life on the $0\nu\beta\beta$ decay. The final detector would consist in building 20 modules similar to the demonstrator. In this context, we would estimate the final detector sensitivity to the $0\nu\beta\beta$ decay.

We suppose the specified activities of $\mathcal{A}^{\text{Tl}} = 2$ μBq/kg, $\mathcal{A}^{\text{Bi}} = 10$ μBq/kg and $\mathcal{A}^{\text{Rn}} = 0.15$ mBq/m^3 are reached. The simulations with an uniform magnetic field are used.

In Tab. 3.10 present the number of expected events in the optimised ROI [2.75;3.1] MeV. The expected number of background events in the region of interest [2.75;3.1] MeV is high enough for the optimised cut-offs to be worth it, with $P_{int} > 4$ % and $|\Delta Z| < 80$ mm (samely for $|\Delta Y|$). They allow primarily to reduce the Radon background by a factor 3. Due to the optimisation of the ROI, especially to the raising of the upper bound, the ^{208}Tl backrgound is a little increased, without important consequences, as the $2\nu\beta\beta$ and ^{222}Rn dominate the total number of background in this energy range.

With an exposure of 500 kg.y, the SuperNEMO final detector should reach a sensitivity $T_{1/2}^{0\nu} > 5.4 \times 10^{25}$ y, with ^{82}Se sources, corresponding to $\langle m_{\beta\beta} \rangle = [0.079 - 0.15]$ eV. By comparison, with the same exposure and background specifications but with ^{150}Nd sources, the final detector would achieve a sensitivity of $T_{1/2}^{0\nu} > 2.2 \times 10^{25}$ y, in the [3.1;3.75] MeV ROI, corresponding to $\langle m_{\beta\beta} \rangle = [0.046 - 0.15]$ eV.

Cut ROI	First-order [2.75;2.95] MeV	Topological [2.75;3.1] MeV
$\epsilon_{0\nu}$ (%)	11.3	10.7
$2\nu\beta\beta$	3.48	3.36
^{208}Tl	0.728	0.756
^{214}Bi	0.945	0.835
^{222}Rn	6.93	2.16

Table 3.10: Expected number of background events in the optimised energy range [2.75;3.1] MeV, for the SuperNEMO final detector (500 kg.y exposure). The $2\nu\beta\beta$ half-life taken as $T_{1/2}^{2\nu} = 9.39 \times 10^{19}$ y, and the nominal background activities are considered. First-order and optimised topological ($P_{int} > 4\%$ and $|\Delta Z| < 80$ mm) cuts have been applied.

- résultat final sans champ

3.8 Conclusion

Assuming the target background levels are reached, the SuperNEMO demonstrator, running for two and half years with 7 kg of ^{82}Se would be able to a set a limit on the $0\nu\beta\beta$ process $T_{1/2}^{0\nu} > 5.6 \times 10^{24}$ years, translating into a limit on the neutrino effective mass $\langle m_{\beta\beta}\rangle < [0.25-0.48]$ eV (depending on the Nuclear Matrix Elements)[6]. Latest measurements of source activities show that the specified background level for ^{208}Tl isotope is not reached, although it is improved in average by a factor of 2, compared to NEMO-3. To offset this, topological selections, designed to reject non-internal and non-simultaneous $2e$ events, have been optimised. The calorimeter time resolution plays an important role on the cut-off efficiencies, especially on the internal probability. Future studies would investigate the influence of this resolution on the final limit set on $T_{1/2}^{0\nu}$. Finally, assuming the worst activity is reached for the internal Bismuth isotope, we would set a limit on the $T_{1/2}^{0\nu} > 3.6 \times 10^{24}$ years, a decrease of 35 % compared to the specified activities result. This corresponds to $\langle m_{\beta\beta}\rangle < [0.31-0.59]$ eV. Finally, the limit on $T_{1/2}^{0\nu}$ could be enhanced by using a multivariate analysis, similarly to what is done in other double beta decay experiments, taking advantage of the several topological variables offered by SuperNEMO.

Recent studies have shown that the 25 Gauss magnetic field would be distorted by detector materials, especially the calorimeter magnetic shields. In this context, we studied the influence on the demonstrator sensitivity of the presence of magnetic field. Switching-off the field would decrease the sensitivity, but can be compensated by the topological cut-offs, useful with such a level of background.. Finally, the absence of magnetic field would slightly increase the limit set on the sensitivity to $T_{1/2}^{0\nu} > 3.7 \times 10^{24}$ years, taking into account the measured activities, and $\langle m_{\beta\beta}\rangle < [0.30-0.58]$ eV. Simulations with a mapped field shown that the signal

---

[6]The real mass of isotope is 6.23 kg, then to achieve a 17.5 kg.y exposure, the demonstrator should run a little more than two years and a half.

and background selection efficiencies would be degraded by a non-uniform field. A more complete study would also take into account the possible impacts on the calorimeter energy resolution.

Like its predecessor, the SuperNEMO demonstrator was designed to study several isotopes, such as the ^{150}Nd. Assuming the target background activities are reached for ^{150}Nd sources, the SuperNEMO demonstrator would achieve a $T_{1/2}^{0\nu} > 2.2 \times 10^{24}$ years, and $\langle m_{\beta\beta} \rangle < [0.15 - 0.50]$ eV.

Finally, assuming we reach the target background levels, the SuperNEMO final detector would achieve an unprecedented limit of $T_{1/2}^{0\nu} > 5.4 \times 10^{25}$ years for ^{82}Se sources, corresponding to $\langle m_{\beta\beta} \rangle = [0.079 - 0.15]$ eV. For ^{150}Nd sources, the half-life $T_{1/2}^{0\nu} > 2.4 \times 10^{25}$ years would be reached, with $\langle m_{\beta\beta} \rangle = [0.046 - 0.15]$ eV, better than for ^{82}Se sources, thanks to its higher $G^{0\nu}$ factor.

To go further in this study, the SuperNEMO collaboration would study the influence on the sensitivity of external backgrounds, coming from detector materials as well as the laboratory. Also, more realistic perfomances of the detector, as well as field variations have to be implemented in the software for the simulations to reproduce more accurately the data.

Improvement of the rejection of the internal Thallium-208 background

At the end of September 2018, the 34 enriched-Selenium source foils were installed on the demonstrator. At this time, the internal ^{208}Tl and ^{214}Bi activities had already been measured by the BiPo detector, as well as the ^{222}Rn concentration inside the tracker chamber. The ^{222}Rn targeted level is reached, and an upper limit have been provided for the internal ^{214}Bi. However, the activity of ^{208}Tl was revealed higher than expected.

We described in the previous chapter the impact of these activities on the final detector sensitivity to the $0\nu\beta\beta$ decay, and optimised topological selections allowed to improve it. In the current chapter, we focus on rejection techniques peculiarly adapted to reject internal ^{208}Tl events, while selecting a significant proportion of $0\nu\beta\beta$ signal.

- parler du fait que le Tl est emmerdant même à haute énergie, même pour un Qbb élevé, à cause de l'électron de conversion à haute E : As explained in Chapter 2, the 2.615 MeV γ-ray produced in the decay of ^{208}Tl is a troublesome source of background.

4.1   Motivations

In Chapters 2 and 3, we presented the specifications set on the background activities, in order to reach an unprecedented limit on the $0\nu\beta\beta$ process half-life in 5 years, with 100 kg of the ^{82}Se isotope, with the final SuperNEMO detector. Tab. 2.1 summarise the target ^{208}Tl, ^{214}Bi and ^{222}Rn activities, and give a comparison with those measured by the collaboration. We achieve the specified level of ^{222}Rn isotope inside with an air flow rate of 2 m^3/h inside the wire chamber. The BiPo detector was only capable of giving an upper limit on the ^{214}Bi level of $\mathcal{A}^{\mathrm{Bi}}$ < 290 μBq/kg, and future precise measurements with SuperNEMO demonstrator will constraint this value. The BiPo measurements also showed that the ^{208}Tl contamination is about 30 times greater than expected. This level of activity has no implications for the demonstrator, as only one ^{208}Tl event
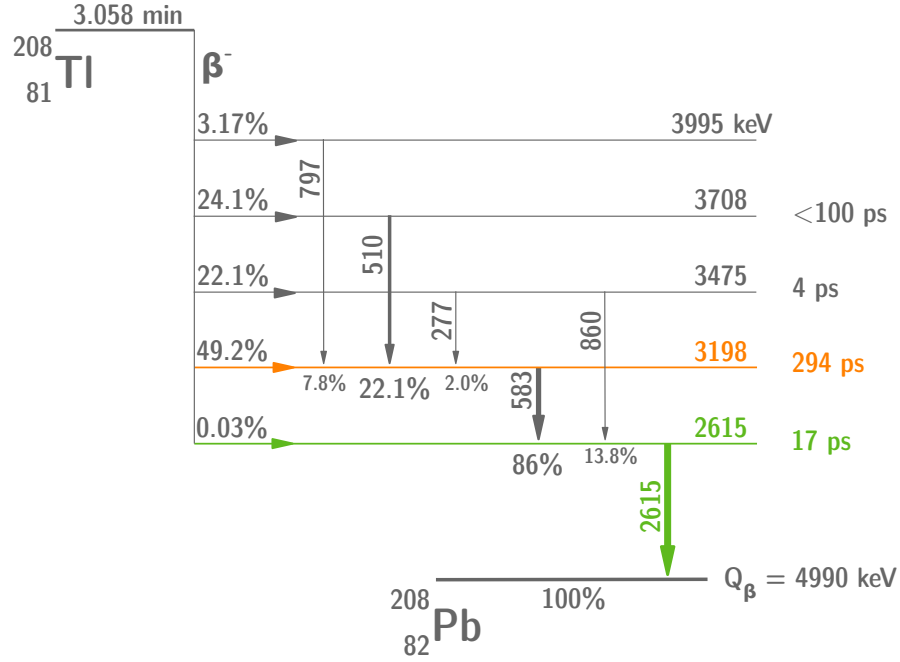
Figure 4.1: A simplified disintegration scheme for the ^{208}Tl isotope. 81 % of the disintegration pass through the 294 ps metastable energy level (orange). All disintegration go through the 2.615 MeV energy level (green), where an orbital electron is ejected in 0.246 % of the cases through the internal conversion process.

is expected in the [2.7;3.15] MeV energy region, after cut-off optimisations, with a 17.5 kg.y exposure. On the other hand, this background could be harmful for the final detector, with 21 ^{208}Tl events expected in the region of interest [2.6,2.95] MeV, for a 500 kg.y exposure. To overcome this effect, it is interesting to set a specific method designed to reject ^{208}Tl events.

In the next section, we describe the specific features of the Thallium internal background. We develop a new technique of rejection, especially designed to identify internal ^{208}Tl events, based on electron Time-Of-Flight computation.

4.2   The internal ^{208}Tl background

Trace quantities of naturally-occurring radioactive isotopes inside the source foils can occasionally produce two-electron events, and thus can mimic $\beta\beta$-decay events. The ^{208}Tl, a progeny of ^{232}Th, is one of the largest contribution to the internal background. In fact, as explained in Chapter 2, two electrons can be produced via β-decay followed by a Møller scattering, β-decay to an excited state with the subsequent internal conversion, or due to Compton scattering of the de-excitation photon (Fig. 2.1).

All the possible transitions for the ^{208}Tl isotope are presented in Fig. 4.1. This shows that ^{208}Tl always β-decays to an excited state of the ^{208}Pb daughter nuclei. In more than 99 % of the decays, at least 2 γ's are expected after the β emission.

For $0\nu\beta\beta$ detection, the most dangerous mode of $\beta\beta$-like events production comes from the internal conversion of the 2.615 MeV-γ, resulting in two electrons emitted with a high energy sum.

4.2.1 The internal conversion process

An excited nucleus will practically constantly achieve a transition to a lower state by one of two processes: the emission of a γ-ray, or the ejection of one of the orbital electrons. The latter, called *internal conversion* (frequently abbreviated IC), is a second-order process, where one electron couples to one of the nucleon inside the excited nucleus. After bringing the energy of the nuclear transition, the electron is ejected from the atom. Thus, in such a radioactive decay, the de-excitation energy of the nucleus is transferred *directly* to a j-shell electron ($j = K, L, M...$). The high-energy electron is therefore emitted not from the nucleus, but from the atom, and carry off the energy

$$E_{IC} = E_\gamma - E_j \qquad (j = K, L, M...) , \tag{4.1}$$

where E_j is the binding energy of the electron in the j-shell, and E_γ is the energy of the γ-ray.

This mechanism is possible because there is a non-zero probability of finding the electron within the nucleus, that is to say, the wave-function of the electron can penetrate the volume of the nucleus. Consequently, due to their high nuclear penetration, electrons coming from the $1s$ state are more likely to be ejected (this transition is called K internal conversion). Although electrons coming from $2s$, $3s$ and $4s$ states (L, M or N internal conversions) have also a non-zero probability to undergo this process. After the electron ejection, the hole in the corresponding shell is filled by an electron from a higher energy level, emitting characteristic X-rays, Auger electrons, or both.

For a given transition, the internal conversion coefficient of the electron in the j-shell, is defined by

$$\alpha_j = \frac{P_{IC,j}}{P_\gamma} , \tag{4.2}$$

where $P_{IC,j}$ is the j conversion electron emission probability, and P_γ is the γ-ray emission probability. The total coefficient is

$$\alpha_T = \sum_{j=K,L,M\cdots} \alpha_j . \tag{4.3}$$

These coefficients are given in Tab. 4.1, for the 2.615 MeV energy level of the ^{208}Tl decay scheme. Therefore, in 0.246 % of the cases, the ^{208}Pb excited nucleus will

Emission probability (%)	α_K (%)	α_L (%)	α_M (%)	α_T (%)
100	0.1708	0.0292	0.00685	0.246

Table 4.1: Internal conversion coefficients for the 2.615 MeV γ-ray of the ^{208}Tl decay scheme.

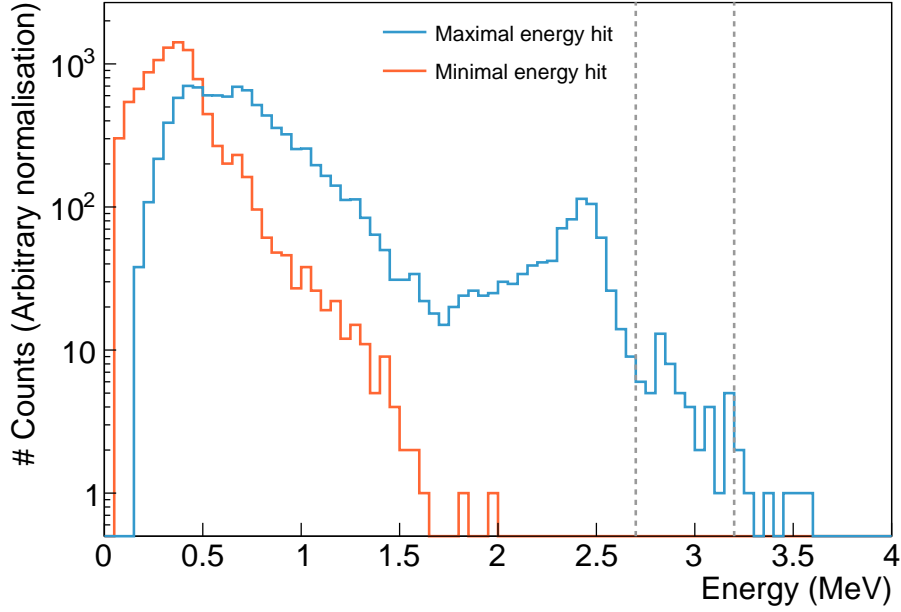undergone an internal conversion corresponding to the 2.615 MeV energy level.

Figure 4.2: Individual energy spectra for selected 2e topologies of ^{208}Tl decays simulated inside the source foils. Calorimeter hit of minimal energy (red) and maximal energy (blue). Spectra are arbitrarily normalised. The [2.7;3.2] ROI is represented by grey dashed lines.

4.2.2 Selection of ^{208}Tl disintegrations in the 2e channel

The ^{208}Tl can present a 2e electrons topology, when after the β emission, an electron is ejected from the atom through internal conversion. Especially, when this energy transfer corresponds to the 2.615 MeV γ-ray, the ejected electron carry off a significant energy, depending on its initial binding energy with the nucleus. An orbital electron from the K-shell is ejected with an energy $E_{IC,K} = 2.526$ MeV, for instance. In such a case, the ^{208}Tl disintegration can be identified in the 2e topology. As one of the two electrons measured with a high energy, this decay is likely to contribute to the background of the $0\nu\beta\beta$ of ^{82}Se, or even ^{150}Nd. In Fig. 4.2 is presented the individual energy spectra for 2e topologies for ^{208}Tl simulations inside the source foils. An usual technique to reject ^{208}Tl background consists in distinguishing 2e topologies for which one of the two calorimeter hits have an energy greater than 2.7 MeV. The energy resolution of the demonstrator being improved compared with the one of NEMO-3, this selection is efficient. This cut-off allow to reject 0.61 % of the ^{208}Tl internal events, while rejecting only 0.11 % of $0\nu\beta\beta$ events.

In the 2e channel, optimised topological cut-offs, based on time-of-flight computation and the distance between vertices, were presented in the previous chapter. They are mostly efficient in rejecting the non-internal ^{222}Rn events. In the next section, we remind and precise the internal probability computation, and present a new selection, also based on the time-of-flight computation, to reject the ^{208}Tl background.

4.3 Rejection of ^{208}Tl with a time-of-flight criterion

- Un des deux gamma est retardé de 294 ps, puis conversion interne -¿ donner le proportion (nb d'ev attendus, dans la ROI). proportion déjà donnée, je pense que tu veux dire le nombre d'événements attendus pour une contamination fixée.

- Avant d'entrer dans le détail préciser le principe de la réjection par temps de vol. L'électron de plus haute énergie est en retard, avec un retard en moyenne de 294 ps pour la plupart des niveaux (discuter un peu le schéma de désintégration, dans quel cas il sera en retard). Ensuite dire que tu as quantifié le pourcentage d'électrons de haute énergie en retard avec une simulation "parfaite" i.e. avec une résolution en temps nulle. A comparer avec le chiffre donné précédemment (issu d'une étude du schéma de désintégration.)

4.3.1 The internal probability

This tool, which aims to reject non-simultaneous events, is presented in detail in Chapter 2. As part of the analysis pipeline, it is widely employed in NEMO-3 and SuperNEMO, for background rejection purposes. We examine an example of its usefulness in Chapter 3. Nevertheless, for reasons to be given latter, in the current chapter, we need to perform our own calculation of internal probability, after the reconstruction pipeline. This is, therefore, an opportunity to come back to this tool and to clarify certain points. The calculation of the internal χ^2 is reminded in Eq. (4.4), for two detected electrons, as a function of the expected times, t^{exp}, the experimentally measured times, t^{meas}, as well as the total uncertainty on the time measurement:

$$\chi^2_{int} = \frac{((t_1^{\text{meas}} - t_1^{\text{exp}}) - (t_2^{\text{meas}} - t_2^{\text{exp}}))^2}{\sigma_{t_1}^2 + \sigma_{t_2}^2 + \sigma_{\beta_2}^2 + \sigma_{\beta_1}^2 + \sigma_{l_1}^2 + \sigma_{l_2}^2} \,. \tag{4.4}$$

The compenents of the total time uncertainty are bring by the calorimeter performance (σ_{t_i}), the uncertainty on particle energies (σ_{β_i}) and the uncertainty on track lengths (σ_{l_i}). In the official SuperNEMO reconstruction pipeline, $\sigma_l = \sigma_{l_1} = \sigma_{l_2} = 0.07$ ns for electrons. As, therein chapter, we are predominantly focusing on the 2e channel to reject the ^{208}Tl background, we would optimise this parameter to describe accurately the internal events.

One way to examine if σ_l is well-evaluated is to look at the flatness of the internal probability distribution for $0\nu\beta\beta$ events in the 2e topology, for which a flat distribution is expected. Indeed, the slope of this distribution provides pertinent information to check the estimation of uncertainties. The flatter the distribution, the more correctly uncertainties are estimated. We perform a lineal fit of the P_{int} distribution on]0.1; 1], to avoid the peak at low internal probabilities, and we define the *flatness parameter* a_F as the slope of this fit. The optimisation then consists in finding the value of σ_l for which the parameter a_F is cancelled. We compute the
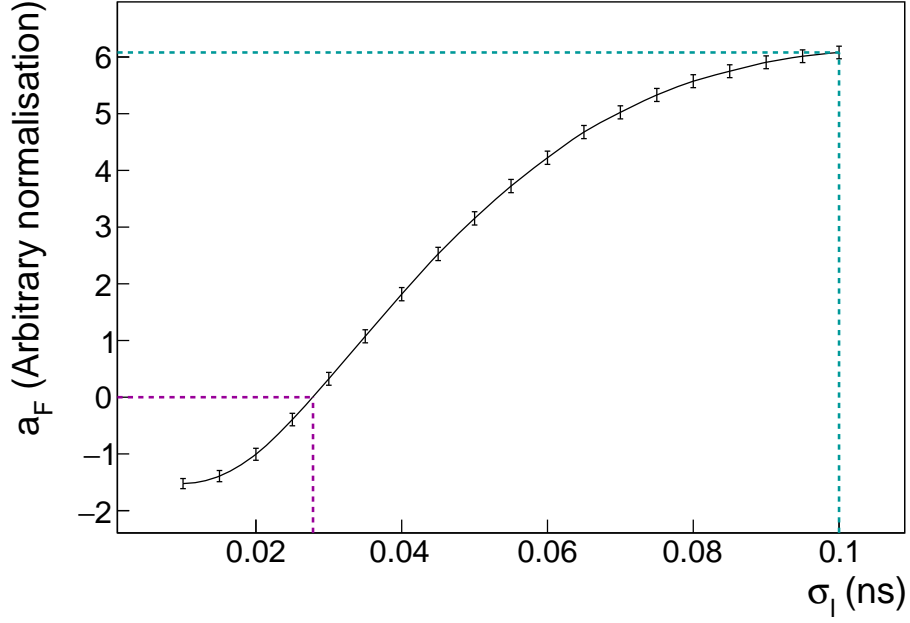
Figure 4.3: Slope a_F as a function of the time uncertainty due to the reconstructed track length σ_l. The former value used in the SuperNEMO reconstruction pipeline is pointed out by blue dashed lines. The value kept for σ_l is the one for which $a_F = 0$, $\sigma_l = 0.0278 \pm 0.0008$ ns, showed by purple dashed lines. The errors made on the a_F fit parameter are represented by the grey filled area. P_{int} is calculated for $0\nu\beta\beta$ decays simulated inside the source foil, with first order cut-offs applied.

P_{int} distribution for simulations of $0\nu\beta\beta$ decays inside the source foils. We select merely $2e$ topologies by using the first order cuts, presented in Chapter 3, such that the internal hypothesis is almost certain to be verified. In Fig. 4.3 is given the slope a_F as a function of σ_l. For $\sigma_l = 0.07$ ns, $a_F > 0$, revealing an overestimation of uncertainties in the computation of the internal χ^2. The optimised value, kept for the further analysis, is $\sigma_l = 0.0278 \pm 0.0008$ ns. In Fig. 4.4 is displayed the internal probability distributions for two values of the σ_l parameter: for the former value $\sigma_l = 0.07$ ns and for the optimised value $\sigma_l = 0.0278$ ns. A more complete analysis would compare the simulated track lengths with the reconstructed ones, for different energy sets of mono-kinetic electrons. Nevertheless, our optimisation is good enough for the current analysis. We use this optimisation for the rest of this analysis, and discussion is in progress to modify this parameter in the SuperNEMO software.

The internal probability is principally designed to reject non-simultaneous events coming from the source foil. Therefore, it is extremely effective in rejecting ^{222}Rn events produced far from the source foils. The internal probability is however not suited for ^{208}Tl disintegrations occurring within the foils, because of the metastable state could delay significantly the electron with higher energy. So we would set up a new law of probability that would express the hypothesis that a given event is an internal ^{208}Tl event.
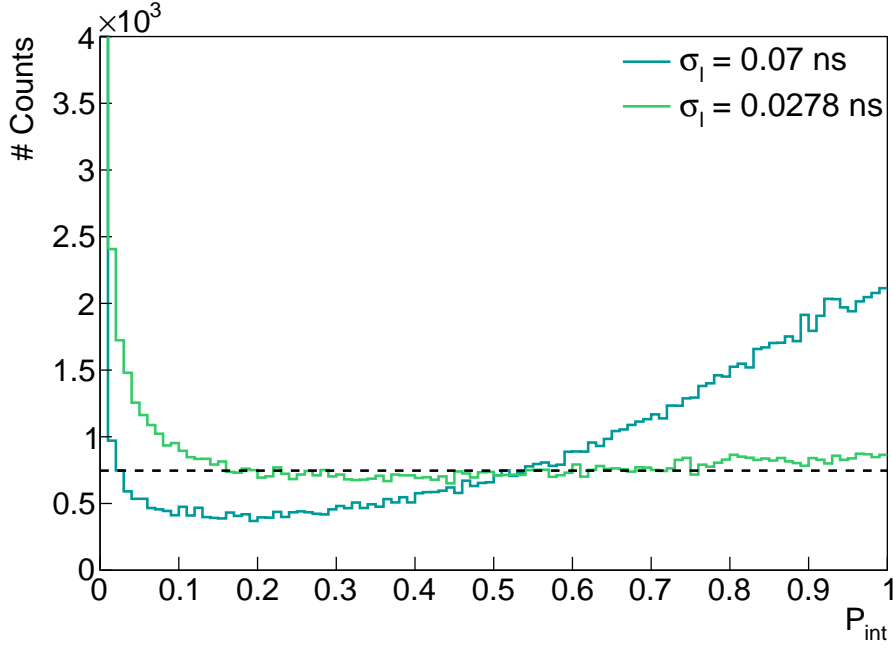
Figure 4.4: Internal probability distributions for $\sigma_l = 0.07$ ns (blue) and $\sigma_l = 0.0278$ ns (green). P_{int} is calculated for $0\nu\beta\beta$ decays simulated inside the source foil, with first order cut-offs applied.

4.3.2   The exponential probability for ^{208}Tl events

According to the disintegration scheme of the ^{208}Tl isotope (Fig. 4.1), there is an 81 % probability of passing through the 294 ps metastable level. After that, to attain the ground state of ^{208}Pb, the excited nucleus has 100% of probability to decay through the 2.615 MeV energy level. At this occasion, in 0.246% of cases (Tab. 4.1), one of the orbital electrons is ejected from the atom following the internal conversion process. To summarise, for 0.16 % of the total ^{208}Tl decays, a β particle is emitted, and a delayed orbital electron is ejected through internal conversion of the 2.6 MeV-γ. We aim to use this delayed electron to discriminate ^{208}Tl internal background from the $0\nu\beta\beta$ signal.

4.3.2.1   Exponentially modified Gaussian

For a given ^{208}Tl disintegration, we define the Δt parameter as the difference of arrival time between the firstly emitted β particle and the delayed IC electron. Supposing SuperNEMO would perfectly measure the particles' times and energies, the Δt probability density function would be an exponential, with the decay parameter $\tau = 294$ ps. We introduced in Chapter 2 the internal probability analysis tool. At this occasion, let us described the components entering in the computation of the total uncertainty on time measurement for the SuperNEMO calorimeter. To take into account measurement uncertainties, we define a Gaussian distribution centred around $\mu = 0$, with a width set up by the $\sigma = \sigma_{tot}$ parameter, detailed in Eq. (2.4). Therefore, to properly describe the β+IC delayed ^{208}Tl events, we have to convolve the exponential and the Gaussian distributions.
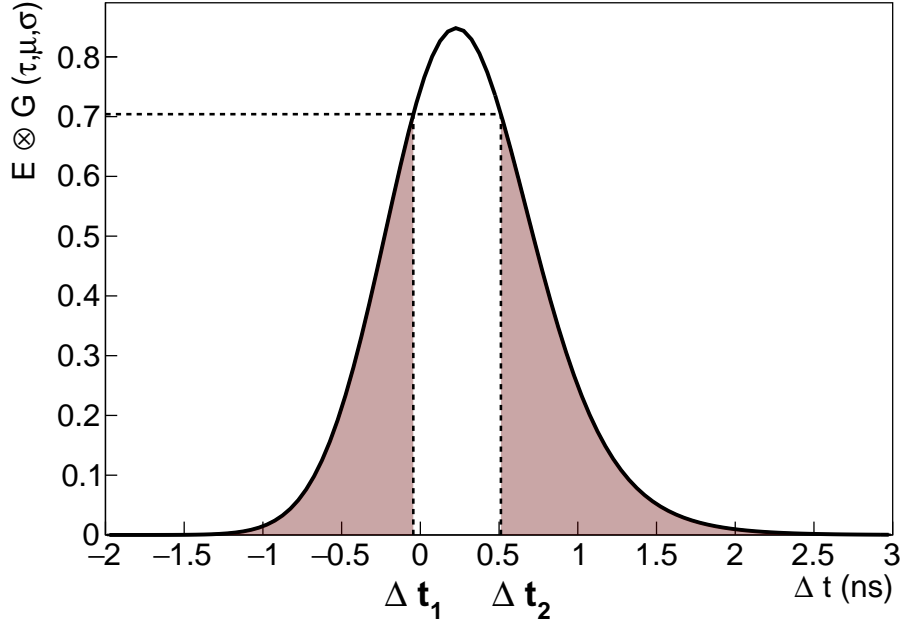
Figure 4.5: Normalised convolution distribution $E \otimes G(\tau, \mu, \sigma)$. The parameters are $\tau = 0.294$ ns, $\mu = 0$ ns and $\sigma = \sigma_{tot}$, computed with $\sigma_l = 0.0278$ ns and $\sigma_t = 0.400$ ns.

4.3.2.2 Probability density function

In Fig. 4.5 we show $E \otimes G(\tau, \mu, \sigma)$, the convolution of an exponential function and a Gaussian function. This density probability distribution corresponds to the case where the two detected electrons were emitted through the β+IC delayed process, given a certain total uncertainty σ_{tot} on the arrival time measurement. For our purpose, the parameter τ corresponds to the decay-time of 0.294 ns of the ^{208}Tl metastable energy level. The two parameters μ and σ correspond to the mean and total uncertainty of the Gaussian function, respectively. In our case, $\mu = 0$ and the total uncertainty is calculated with $\sigma_l = 0.0278$ ns and $\sigma_t = 0.400$ ns. Each probability density function is unique and depends on the value of the measured energies for the two particles detected in the $2e$ topology. In the given example, we considered two particles interacting inside the calorimeter with an energy of 1 MeV each. The $E \otimes G(\tau, \mu, \sigma)$ distribution is normalised.

4.3.2.3 Exponential probability

Once the probability density function is built for a given $2e$ event, we would define the probability P_e that this event comes from a β+IC delayed decay. We want to define the exponential probability following the same principle as for the internal probability, for comparison purposes. Therefore, we would obtain the maximal value $P_e = 1$ when the value of Δt is the most favourable, i.e. when Δt is of the order of the mean of the $E \otimes G(\tau, \mu, \sigma)$ distribution. On the other hand, minimal values for P_e would be reached for unfavourable values of $|\Delta t|$, so $P_e \xrightarrow[|\Delta t| \to +\infty]{} 0$.
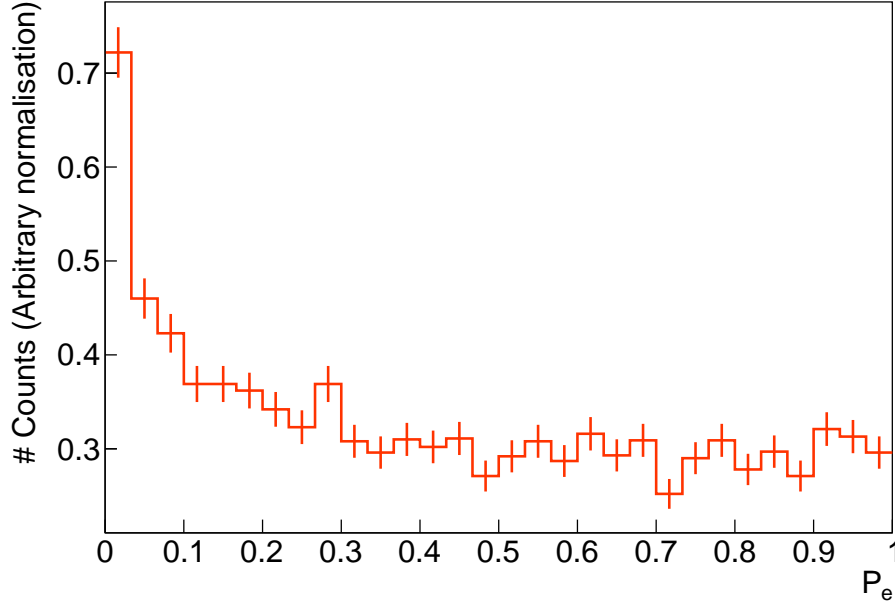
Figure 4.6: Exponential probability distributions for ^{208}Tl (red) and $0\nu\beta\beta$ (green) simulations, after first-order cut-offs applied. $\sigma_t = 0.400$ ns, $\sigma_l = 0.0278$ ns.

Following these two requirements, the exponential probability is defined as

$$P_e = \int_{-\infty}^{\Delta t_1} E \otimes G(\tau, \mu, \sigma) \, dx + \int_{\Delta t_2}^{-\infty} E \otimes G(\tau, \mu, \sigma) \, dx \,, \qquad (4.5)$$

where Δt_2 is one of the two primitives of $E \otimes G(\tau, \mu, \sigma)$ as $f(\Delta t_1) = f(\Delta t_2)$.[à changer] These two integrals are represented by coloured areas in Fig. 4.5. The same way as internal probability, exponential probability distribution is expected to be flat for ^{208}Tl simulations on $]0; 1]$.

In fig. 4.6 is presented an exponential probability distribution for ^{208}Tl and $0\nu\beta\beta$ simulations inside the source foils, after first-order cut applied. The

4.4 Event selection

4.4.1 Selection on particle detection times

After an event is tagged as a $2e$ topology, we consider the two arrival times of the electrons inside the calorimeter. The time t_1 defines the arrival time of the highest energy particle, and the time t_2 designates the other. The time difference between the two arrival times is then defined as

$$\Delta t = t_1^{\mathrm{meas}} - t_2^{\mathrm{meas}} \,. \qquad (4.6)$$

The time t_i^{meas} it takes for a particle to reach the calorimeter depends on how long it took for it to exit the source foils after emission, as well as how long it took for

it to travel through the wire chamber. In order to remove from Δt the dependency on travel time in the tracker, we define the corrected time difference as

$$\Delta t^{\mathrm{corr}} = (t_1^{\mathrm{meas}} - t_1^{\mathrm{exp}}) - (t_2^{\mathrm{meas}} - t_2^{\mathrm{exp}}), \qquad (4.7)$$

where t_i^{exp} is the expected arrival time, calculated with the particle energy and track length.

The two distributions Δt and Δt^{corr} are presented in Fig. 4.7, for $0\nu\beta\beta$ and ^{208}Tl simulations inside the source foils. For $0\nu\beta\beta$ simulations, the Δt distribution is centred around zero, as expected. Indeed, the two electrons of highest and lowest energy are not expected to be delayed. Then, the correction on time difference only lowers the standard deviation of the distribution. However, the mean of the Δt distribution for ^{208}Tl events is slightly shifted towards negative values to -0.218 ± 0.013 ns. This is an indication of the existence of β+IC events, delaying the arrival time t_1^{meas} of the particle of highest energy.

A simple way of rejecting ^{208}Tl delayed events consists in considering the sign Δt^{corr}. We want to select $2e$ topology arising from β+IC delayed decays. These events are more likely to present $t_1 < t_2$, and therefore $\Delta t < 0$.

- cut Pint/Pexp

- Montrer un biplot Pint/Pexp pour les evts Tl208 en représentant la coupure.

- Optimisation of event selection: cut on delta t

- 208Tl cut efficiency

- cut efficiencies on 0nubb and other backgrounds

- Donner le nb d'ev rejeté sur le nb d'ev total, puis sur le nb d'ev retardés

- relier coupure sur proba avec coupure sur delta t (¡0,¿0)

4.5 Impact of ^{208}Tl rejection on the experiment's sensitivity

Reprendre l'analyse de sensibilité faite avec Axel en rajoutant les cuts Pint/Pexp et delta t pour le final detector

4.5.1 Influence of the calorimeter time resolution

- Se servir des résultats de σ_t trouvés au chap. **??**

- Mais dire que ces sigmas peuvent être améliorés

- donc présenter l'évolution des résultats (efficacité de réjection et sensibilité) sur la réjection en fonction de la valeur de sigma t, à faire varier dans un certain range.

(a) $0\nu\beta\beta$ simulations.
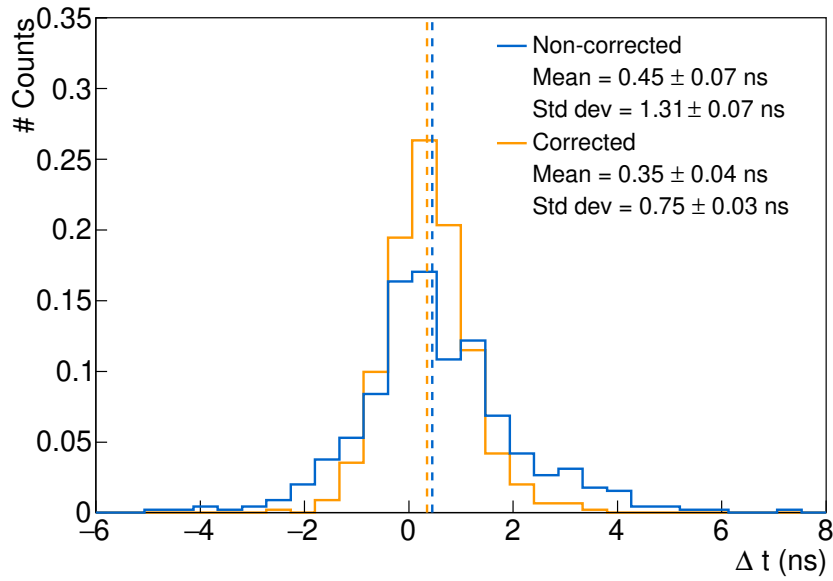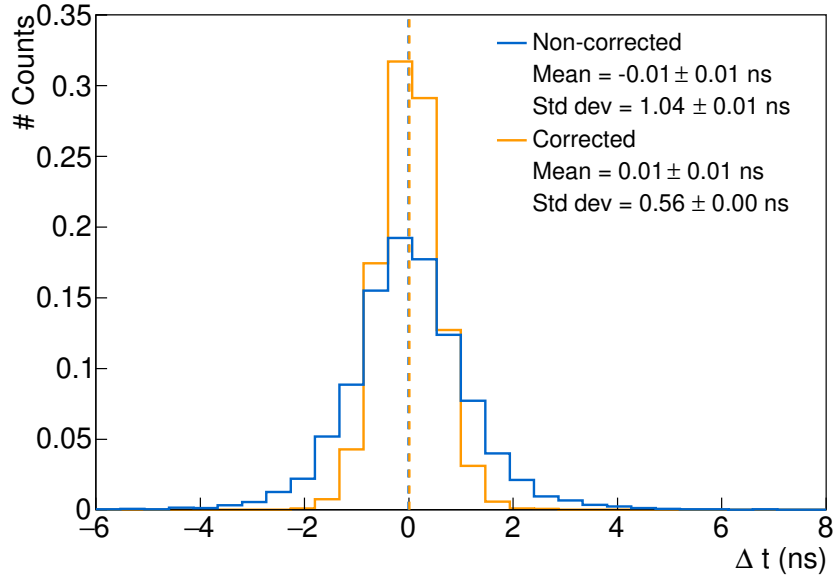

(b) ^{208}Tl simulations.

Figure 4.7: Corrected (orange) and non-corrected (blue) arrival time difference between the two electrons. (a) $0\nu\beta\beta$ simulations inside the source foils. (b) ^{208}Tl simulations inside the source foils. The first-order selections have been applied. The two distributions are normalised. $\sigma_t = 0.400$ ns and $\sigma_l = 0.0278$ ns.

- Tu pourrais avec une figure à 2D où tu montres l'efficacité relative 0nu (égale à 100% avant cette coupure temporelle) en fonction de la réjection du Tl208 -¿ cela donne une courbe que tu parcoures et tu cherches à optimiser ton point de fonctionnement.
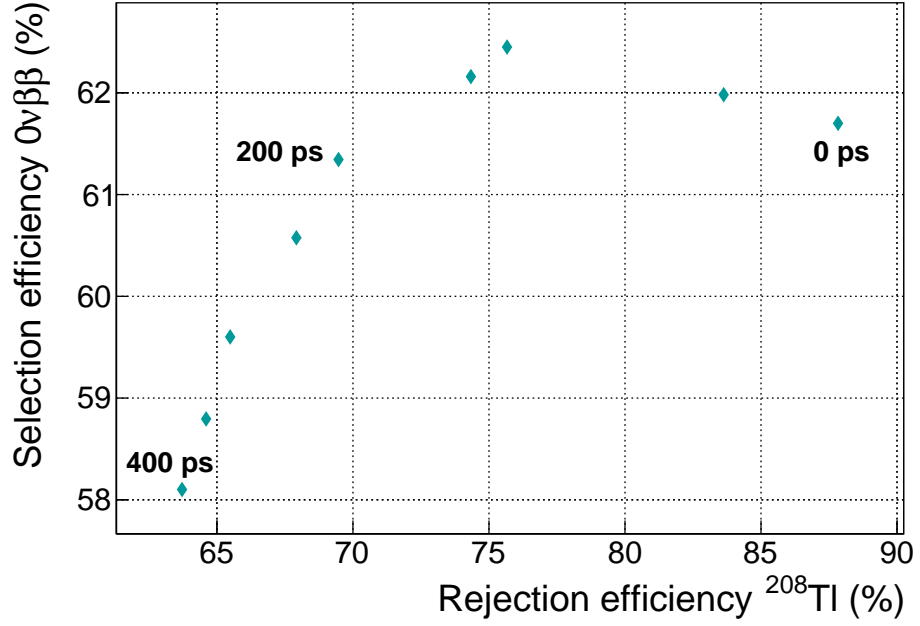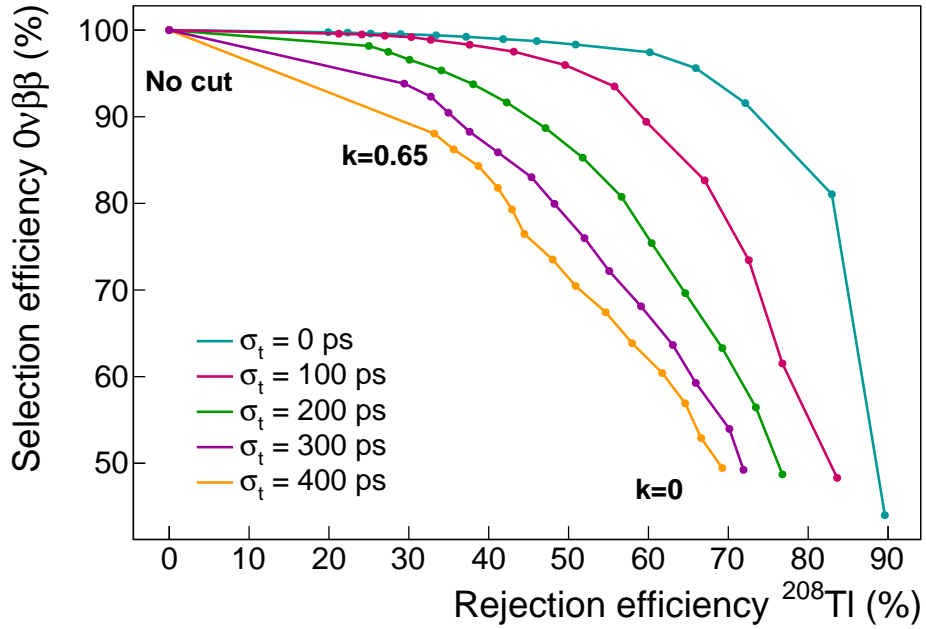
Figure 4.8: $0\nu\beta\beta$ selection efficiency as a function of ^{208}Tl rejection efficiency. Each data point corresponds to a given value of σ_t, decrementing in 50 ps steps. First order selections applied on $0\nu\beta\beta$ and ^{208}Tl simulations. $\sigma_l = 0.0278$ ns.
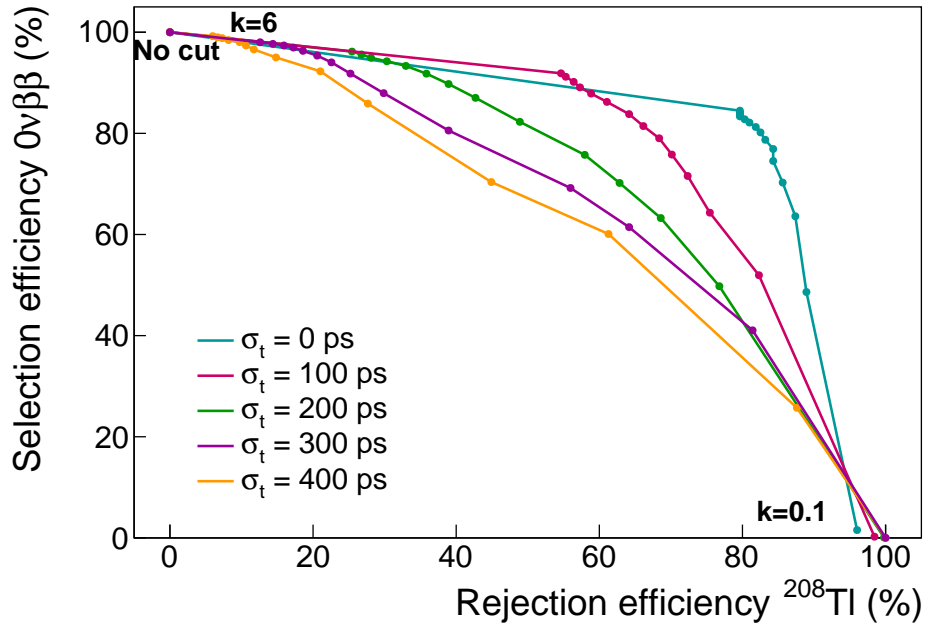

Figure 4.9: $0\nu\beta\beta$ selection efficiency as a function of ^{208}Tl rejection efficiency. Each data point corresponds to a given value of σ_t, decrementing in 50 ps steps. First order selections applied on $0\nu\beta\beta$ and ^{208}Tl simulations. $\sigma_l = 0.0278$ ns.

Figure 4.10: $0\nu\beta\beta$ selection efficiency as a function of ^{208}Tl rejection efficiency. Each data point corresponds to a given value of σ_t, decrementing in 50 ps steps. First order selections applied on $0\nu\beta\beta$ and ^{208}Tl simulations. $\sigma_l = 0.0278$ ns.

4.6 Conclusions

- On peut éventuellement mettre une source de 232U dans le détecteur (un des parents de 208Tl) pour tester la réjection.

- ajout sélection énergie

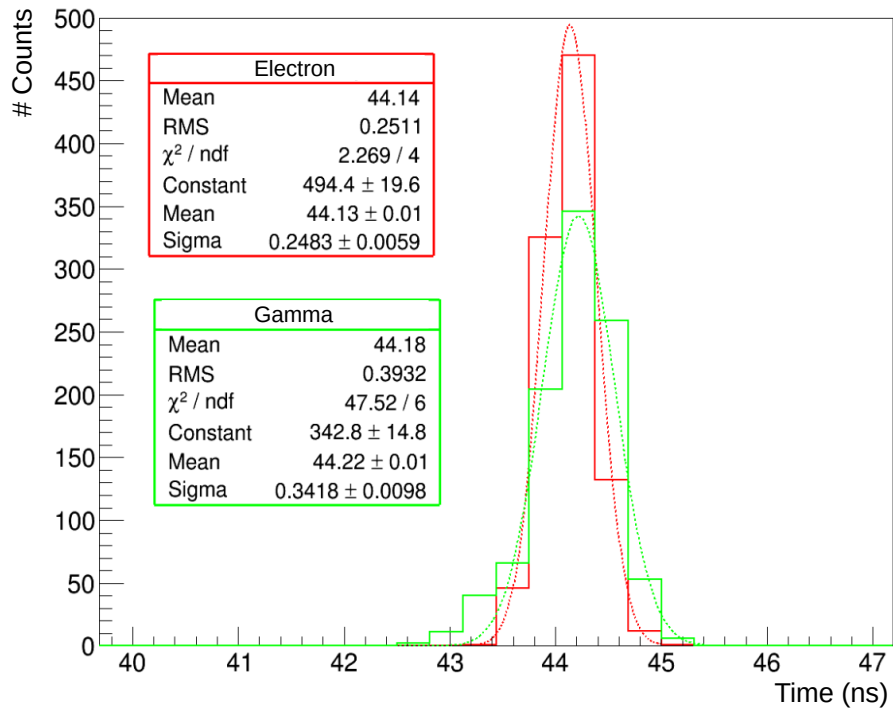- plus correct de couper sur Pexp que sur delta t car on tient compte des erreurs

Figure 4.11: Time distribution of the trigger time of an optical module in the case of electrons (red) and gamma radiation (green) depositing an energy of 1 MeV in the scintillator. The trigger threshold is set at 45 mV and corresponds to an energy of 0.150 MeV. Adapted from [?].

Characterisation of the calorimeter time resolution

The precise knowledge of the different particle interaction times in the optical modules of the SuperNEMO calorimeter is important to better understand and reject the background. For example, the study of electron time-of-flight allows us to distinguish internal events (occurring within the source foils) from external events (radioactive decays occurring outside the source foils, for example in the PMTs or in the iron shielding).

During the commissioning phase, a lot of work, presented in Chapter 6, was achieved to calibrate the detector. Following on from this task and completing it, a great part of the present thesis was allocated to determine the time resolution of the SuperNEMO calorimeter, and to provide tools to purchase this analysis.

In this chapter we present different studies conducted in order to characterise the time response of the SuperNEMO optical modules. Although the goal of the presented studies is to characterise the time resolution of the SuperNEMO calorimeter, some detector adjustments were still ongoing at the time of the acquisition, that could influence the presented results. Especially, the energy calibration described in Sec. 6.3 was not complete, and the Light Injection System presented in Sec. 5.3 was not yet fully operational. However, all the work presented here is necessary in the framework of the first calorimeter calibration. Moreover, I provide all the analysis tools for the collaboration, with a view to doing a possible update, once the whole demonstrator construction will be complete.

The first study presented in this chapter focuses on the characterisation of the time resolution of the SuperNEMO calorimeter, using a calibration source made of Cobalt 60. In the second part of this chapter, we study the possibility to gather informations on the calorimeter time resolution using the Light Injection System, a set-up initially designed to calibrate in energy the calorimeter.

5.1 Interaction of particles in the SuperNEMO scintillators

Understanding how particles interact in the SuperNEMO scintillators is essential. The calorimeter part of the demonstrator mainly aims to detect electrons and photons. In this section, we review ***.

5.1.1 Interaction of electrons

Electrons interact with matter through one of two processes: elastic scattering on a nucleus, or inelastic scattering from an atomic electron. Inelastic scatterings are dominant for polystyrene scintillators and occur through two different forms: coherent scattering with the electron cloud, and radiative energy losses (the so-called bremsstrahlung effect). In Fig. 5.1a is displayed the stopping power of electrons in polystyrene for these two processes. Electrons detected in
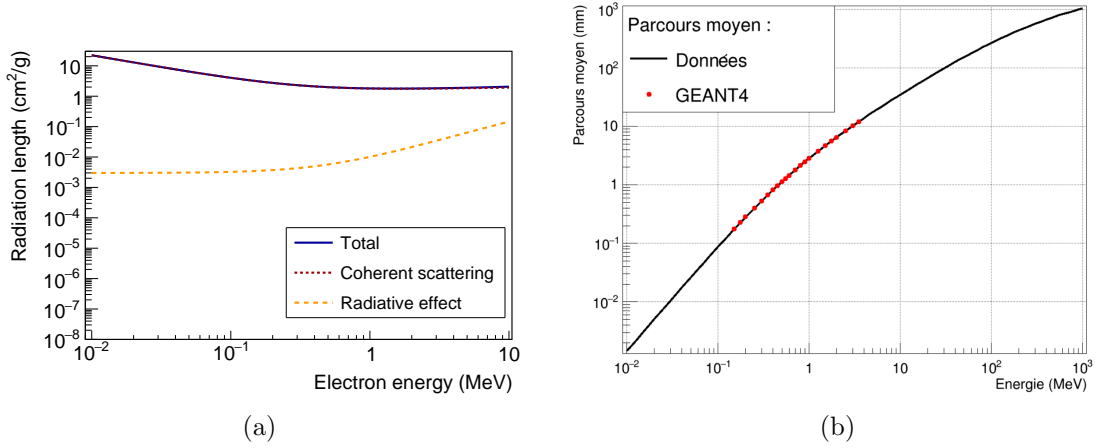

(a)   (b)

Figure 5.1: Stopping power (a) and mean free path (b) for electrons in polystyrene. (a) Energy losses through radiative effect (orange dashed line) and coherent scattering (red dashed line), which is the dominant process for the considered energy range. (b) At 1 MeV, the mean free path of an electron is about 3 mm.

the SuperNEMO calorimeter should deposit a minimal energy of 50 keV (the acquisition low energy threshold) and a maximal energy of few MeV (depending on the $2\nu\beta\beta$ isotope). In this energy range, collisions with the electron cloud are preponderant compared with radiative energy losses. In Fig. 5.1b, we give informations about the mean free path of an electron in polystyrene. In particular, we observe that an electron of 1 MeV penetrates, in average, several millimetres into a polystyrene scintillator.

5.1.2 Interaction of photons

Photons travelling in matter can interact with the electronic cloud, through 3 main processes, whose contributions are presented in fig. 5.2a, depending on their energies. Low-energy photons mainly interact with the electron cloud, either
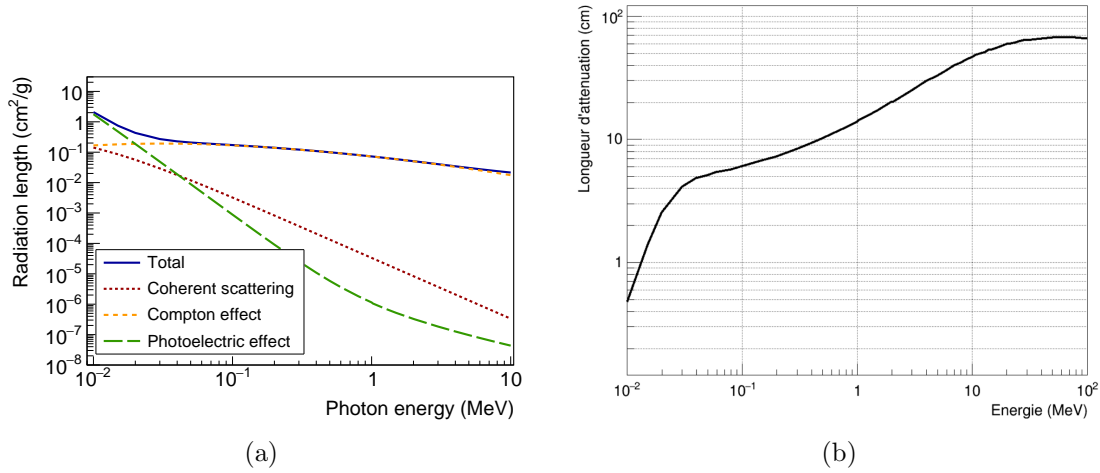
Figure 5.2: Linear attenuation coefficient (a) and attenuation length (b) for γ radiations in a plastic scintillator made of polystyrene. (a) In the considered energy range of $10\,\text{keV} - 10\,\text{MeV}$, γ radiations interact with matter mainly through Compton diffusion. (b) The attenuation length of a γ radiation is about 10 cm at 1 MeV.

through photoelectric effect (γ radiation is fully absorbed by an electron of the cloud), or through coherent (so-called Rayleigh) scattering. But the dominant effect, for energies between 10 keV and 10 MeV, is the Compton inelastic scattering of a γ with an atomic electron. In Fig. 5.2b, we display the mean attenuation length of a γ radiation in polystyrene scintillators, with energy. Thus, most of 1 MeV γ radiations will interact around 10 cm inside the scintillating material.

At the considered energy range ($10\,\text{keV} - 10\,\text{MeV}$), the interaction of photons with matter is dominated by Compton effect, while the electrons interact mainly through coherent scattering. The SuperNEMO scintillators are designed to detect such particles. Photons have a high probability to interact inside the volume of the scintillator, while electrons are stopped in the first few millimetres.

The following two sections are devoted to the study of the time resolution of the SuperNEMO optical modules.

5.2 Measurement of the time resolution with a ^{60}Co source

This section is dedicated to detail the time resolution study performed using a Cobalt 60 source, exploiting the time characteristic of two photons emitted during the radioactive disintegration process of this nucleus. A great proportion of the whole SuperNEMO demonstrator was successfully characterised using this radioactive source.

5.2.1   Description of Cobalt 60 nucleus

The Cobalt 60 is a man-made isotope, with a 5.27 years half-life, of which we provide the main interesting properties in the simplified decay scheme of Fig. 5.3. This unstable nucleus spontaneously decays, through the β^- process, into an
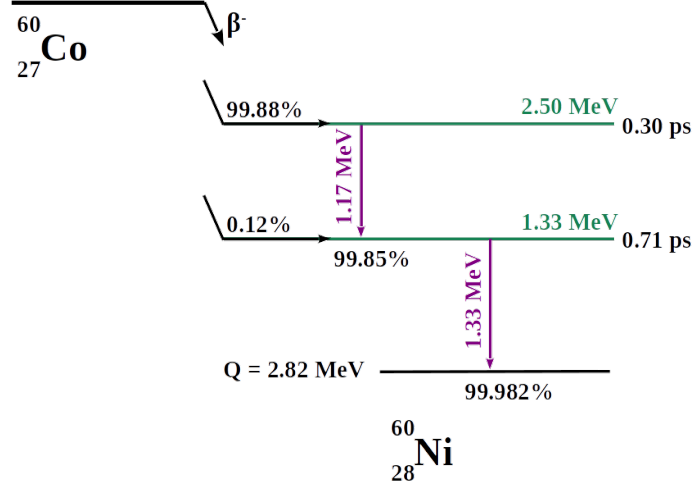

Figure 5.3: A simplified decay scheme for Cobalt 60 [7]. The Cobalt decays, through β^-, predominantly to the 2.50 MeV state. Then, two γ's (whose energy levels are represented in green) are emitted in 99.83% of the cases. The two photons have an energy of 1.17 MeV and 1.33 MeV, respectively. As the life-time of the 1.33 MeV energy level is short (< 1 ps) with respect to the timing precision of the calorimeter, the two photons can be considered as emitted in coincidence. We use this property to calibrate in time the demonstrator optical modules.

excited state of Nickel 60. To reach the ground state of the Nickel 60, the nucleus goes through two successive energy levels, emitting two photons of 1.17 MeV and 1.33 MeV, respectively. The life-time of the second energy level is under the picosecond, thus very short with respect to the expected timing precision of the calorimeter. Therefore, the two photons are considered as emitted in coincidence.

We aim to exploit these two photons emitted after the β^- disintegration to determine the calorimeter time resolution.

5.2.2   Time response of optical modules

In order to characterise incoming charged particles (alphas, electrons), each calorimeter block of SuperNEMO is composed of a scintillator and a photomultiplier. The purpose of the scintillator material is to stop the incoming particles, which will induce the production of the so-called optical photons. The optical photons reaching the photomultiplier photocathode are then converted into electrons, with an efficiency called quantum efficiency. After amplification, electrons are collected by the anode which delivers an electric signal whose charge is proportional to the initial amount of incident photoelectrons. This signal is then transmitted, via the PM voltage divider, to the electronic readout, where the signal is sampled. The particle energy, as well as the time of arrival introduced in

Sec. 6.1.2, can be extracted from the signal waveform analysis. Each step of the charged particle detection process, from the incident particle interaction inside the scintillator, to the signal sampling at the electronic readout, can have an impact on the precise time measurement of the charged particle. We introduce the so-called calorimeter time resolution σ_t, which encapsulates the global uncertainty on the time-arrival measurement of particles into the calorimeter. The squared time-resolution can therefore be expressed as the sum of two contributions: the scintillator resolution $\sigma_{t,\mathrm{sc}}^2$, and the PMT resolution $\sigma_{t,\mathrm{PM}}^2$,

$$\sigma_t^2 = \sigma_{t,\mathrm{sc}}^2 + \sigma_{t,\mathrm{PM}}^2 \,. \tag{5.1}$$

In the following, we detail in depth the physical origins of these terms.

Scintillator time dispersion

The scintillator temporal dispersion $\sigma_{t,\mathrm{sc}}$ in Eq. (5.1) receives contributions mainly from two important characteristics of the scintillator operating principle.

Interaction point: The incoming particle's interaction point location inside the scintillator block highly contributes to the scintillator temporal uncertainty, and depends on the incident particle type. In fact, this effect will not have the same impact on time dispersion, depending on whether the incident particle is a photon or an electron. In Fig 5.4 are schemed the interactions of a photon and that of an electron for the specific case of a SuperNEMO plastic scintillator. In Sec. 5.1, we exposed the different interaction types of photons and electrons. We have also explained the origin of the differences that exist in terms of interaction depth between these two types of particles. To remain consistent with these conclusions, we represent the electron as interacting in the first millimetres, while the photon stops deep inside the scintillator. When a particle (photon or electron) interacts in the scintillating material, the absorbed energy leads to the isotropic emission of scintillation photons: they propagate inside the scintillator, in all directions from the interaction point, at the speed of c/n_{sc}, with n_{sc} the optical index of polystyrene, and c the light speed in vacuum. Depending on their initial direction, some of those photons propagate straight to the PMT (we name them the *direct* photons), while others are at least reflected once on the scintillator surface, before reaching the PM glass. This mechanism leads to time delays between direct and reflected photons.

In order to illustrate, and give an order of magnitude of this delay, let us consider an example where an incoming γ particle enters a scintillator from the front face, and interacts right in the centre of the scintillator volume. After the scintillation emission process, a direct photon will reach the PM glass surface at time

$$t_s = \frac{L}{2c/n_{sc}} \,, \tag{5.2}$$

L being the scintillator width. Now, let us consider another photon, that we name *backward reflected*, emitted in the opposite direction. It will propagate, reflect on
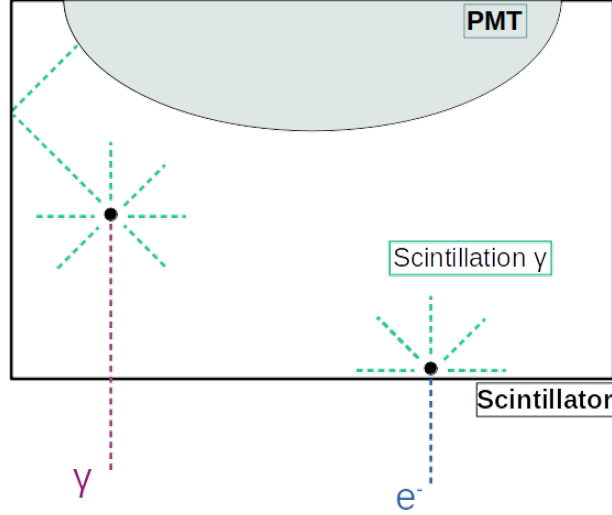
Figure 5.4: A scheme of interaction of particles in a scintillator. The photon case is displayed on the left in pink dotted line, and the electron case is on the right in dark blue dotted line. Both particles enter in the scintillator through the front face. Examples of interaction points inside the scintillator are represented by the black dots. The photons of scintillation emitted isotropically after the interaction are materialised by the bright green dotted lines. Due to different interaction probabilities in matter, the two particles intercat at different depths inside the scintillator. The photon can interact deeply inside the volume, while the electron has a high probability to stop within the first few millimetres.

the front scintillator surface, and finally reach the PM at

$$t_r = \frac{3L}{2c/n_{sc}} \, . \tag{5.3}$$

This reflected photon is therefore delayed compared to the direct photon, with a time-shift of

$$\Delta t^{r,s} = t_r - t_s = \frac{L}{c/n_{sc}} \, . \tag{5.4}$$

In the case of a SuperNEMO scintillator, the length L has been designed to 25 cm, and the optical index is the one of polystyrene with $n_{sc} = 1.5$. Finally, for an incoming particle interacting at the centre of a SuperNEMO scintillator volume, a backward reflected scintillation photon will reach the PM glass 1.25 ns later than a direct photon. And this delay is even more important as the incident particle interacts deep inside the scintillator.

In view of the conclusions given in Sec. 5.1, we know that photons have a higher probability of interacting far into the scintillator block, compared with electrons. Therefore, this time-shift effect is all the more important for incoming photons, while it is quite negligible for incoming electrons, for which reflected photoelectrons reach the PM glass almost as the same time as the direct ones.

This mechanism increases the signal collection rising time at the PM anode, and boosts the scintillator time dispersion $\sigma_{t,\mathrm{sc}}$, with $\sigma_{t,\mathrm{sc}}^{\gamma} > \sigma_{t,\mathrm{sc}}^{e^-}$.

Scintillating light emission: When a particle interacts in a SuperNEMO scintillator, two successive mechanisms of light absorption/re-emission take place. Firstly, the excitation of scintillator molecules leads to the creation of fluorescence photons. Afterwards, those optical photons are absorbed, then re-emitted by the POPOP agent, at higher wavelengths (for more details, we refer to Sec. 2.1.5 of Chapter 2). The characteristic times of these two processes contribute to increase the scintillator time dispersion $\sigma_{t,\text{sc}}$.

Now that two main contributions accounting for the uncertainty on time measurement taken by the scintillator had been developed, we detail the origin of the second term of Eq. (5.1), $\sigma_{t,\text{PM}}$.

Photomultiplier time dispersion

A photomultiplier is a photodetector: after the light is collected and converted at the photocathode, the photoelectrons are multiplied. The transit time for the photoelectrons emitted at the photocathode to reach the anode after being multiplied is not constant for every photoelectron, due to a varying path for electrons emitted by the different dynodes. This results in a timing dispersion. This fluctuation is called transit time spread (TTS). It leads to an uncertainty on the time measurement and so has an influence on the photomultiplier time dispersion $\sigma_{t,\text{PM}}$.

In the following, we describe how we characterised the time dispersion brought by the optical module on the time measurement, using a Cobalt 60 source.

5.2.3 Final experimental design

The idea to use a Cobalt 60 source to characterise the time response of the calorimeter part of SuperNEMO had never been tested before the current analysis. Therefore, all the experimental design had to be implemented.

Setting up the experimental design

The initial activity of the Cobalt source we used for this experimental set-up was 447.4 kBq in February 2014. Given the half-life of this isotope, it was reduced to 232 kBq at the time of the data-taking. In order to determine the best design, and later to monitor and compare the results obtained in the framework of this analysis, I performed simulations of ^{60}Co disintegrations with the source activity at the time of the data-taking, for the demonstrator configuration. The characteristics of those simulations are detailed later in this section.

As the demonstrator was closed at this time, it was impossible to set the Cobalt source inside the detector, at the source foils level. Hence, the calibration source was placed behind the calorimeter, as displayed in Fig. 5.5a, where we can distinguish a side view of the calorimeter.

As described in Chapter 2, the SuperNEMO calorimeter is composed of two main walls (called *French* and *Italian* sides), as well as the so-called X-Walls (on

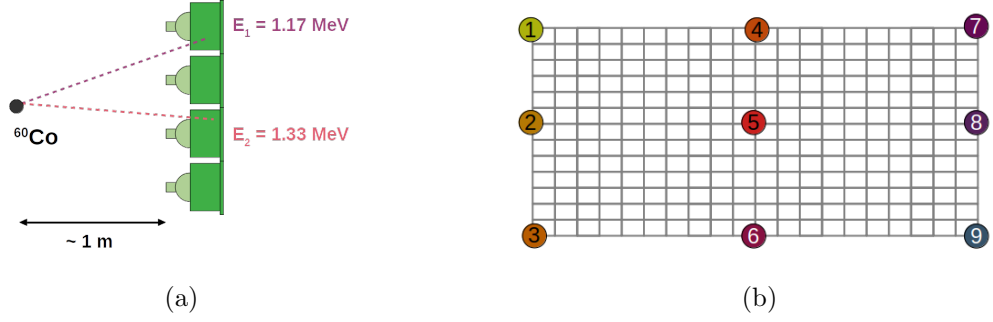(a)   (b)

Figure 5.5: (a) Side view example of the Cobalt source positioning
behind a calorimeter main wall, schemed by 4 optical modules (green).
The emissions of the 2 γ's of interest are displayed in coloured dotted
lines. (b) Front view of the nine source positions behind a main wall.
Each grey box represents an optical module.

the detector sides) and γ-Vetos (on top and below the detector). At the time of
the data-taking, X-Walls and γ-Vetos were not yet operational, hence the current
analysis only applies on the French and Italian main calorimeter walls. In order
for all PMs to detect γ's from Cobalt decays, several bunches of data acquisitions
were taken: the source was placed at 9 different positions on each of the 2 main
calorimeter walls, approximately one meter behind. Therefore, in total, 19 data
acquisitions have been taken, of which:

- 18 with the Cobalt source set behind the wall. The 9 different positions for
  one wall are represented in Fig. 5.5b.

- 1 acquisition have been taken without the Cobalt source, with the Italian
  main wall, to characterise the background detected with the current
  calorimeter settings.

Each data acquisition lasted about 25 minutes, for a total of 10 hours of on-site
activities, taking into account the time needed to move the Cobalt source from
spot to spot.

Currently, the demonstrator is not protected from the laboratory lights
by the anti-radon tent. As laboratory lights would damage the SuperNEMO
photomultipliers, two removable black curtains are deployed on top of the detector,
and acquisitions are taken in dark laboratory. With this way of doing, data
acquisitions can be performed, while eventual necessary repairs remain possible
during the detector commissioning. Nevertheless, taking acquisitions in the dark
is a big constraint. Moreover, the source, initially used for teaching purposes,
was loan by IPN laboratory (Orsay), for only two weeks, mainly because of legal
constraints. Therefore, to not disturb LSM on-site activities (and to make the loan
time profitable), a SuperNEMO team and I performed night shifts to take data.
The acquisition took place during two weeks, at the summer break 2019.

Simulated data

sigma t !!

Cobalt events simulations: As for the data acquisition, the simulated source has been placed behind the calorimeter walls. Hopefully, there was no need to simulate all the 18 positions. In fact, at this time, the detector implemented in simulations is symmetrical in terms of detection performances. Therefore, simulations of ^{60}Co events behind the two main walls are equivalent, and we only need to simulate events from 4 locations (positions 1, 2, 4 and 5, according to the Fig. 5.5b numbering system), other being obtained by symmetry operations. I used the Falaise software to perform these simulations. Four data-taking, for a total of 10^9 Cobalt events, were simulated, using the IN2P3 computing centre platform. A visualisation, provided by the Falaise Software, of a simulated Cobalt event behind the Italian calorimeter main wall, is shown in Fig. 5.6. All the simulations carried

Figure 5.6: Visualisation of a simulated Cobalt event.

out as part of this study have been made available to the collaboration.

Background events simulations: Currently, the Falaise software does not supply a complete set of background events simulations for the demonstrator design. This will be implemented as soon as the final demonstrator performances has been determined. Thus, we did not have at our disposal background events simulations for this analysis.

The entire experimental set-up was designed and carried out by me and a group of physicists from LAL, Orsay and LPC, Caen. I developed a complete set of ROOT codes for data processing and analysis, available on the GitHub platform[1].

5.2.4 Signal events selection

We aim to use the two γ's of 1.17 MeV and 1.33 MeV from Cobalt 60 β^- decay, to characterise the time resolutions of individual optical modules. Thus, the signal we are looking for is two particles detected in coincidence in distinct optical modules. In order to maximise the signal to background ratio, some selections have been applied on data.

- Trigger criteria:
  as we look for two calorimeter hits, we only keep events with exactly two

---

[1]Link to my GitHub page: https://github.com/girardcarillo

triggering electronic channels. Moreover, we are interested in events with two hits which passed both the high amplitude threshold, corresponding to approximately 150 keV. *est-ce que c'est vraiment utile ? pcq on a le cut à 0.7 MeV donc bon ...*

- Coincidence time criterion:
  we define the coincidence time-window by events occurring in a 62.5 ns-long time interval. This allows to avoid accidental coincidence events (interactions of two gammas, produced by different sources, in two optical modules), while keeping events where two γ particles interact at both ends of the wall. This time-window was set for the data-taking and can be improved for eventual future acquisitions.

- Individual energy selection:
  given the two photon energies, we only select individual calorimeter hit energies greater than 0.7 MeV, to reject double Compton interactions of one single photon from Cobalt in different optical modules. This energy selection is sufficient for ^{60}Co γ particles, but not for background such as ^{208}Tl. Moreover, it highly depends on the calibration discussed in Sec. 6.3. We show in Fig. 5.7 the highest energy hit with the lowest one, for simulated data with ^{60}Co source in position 5. The high energy threshold, and the
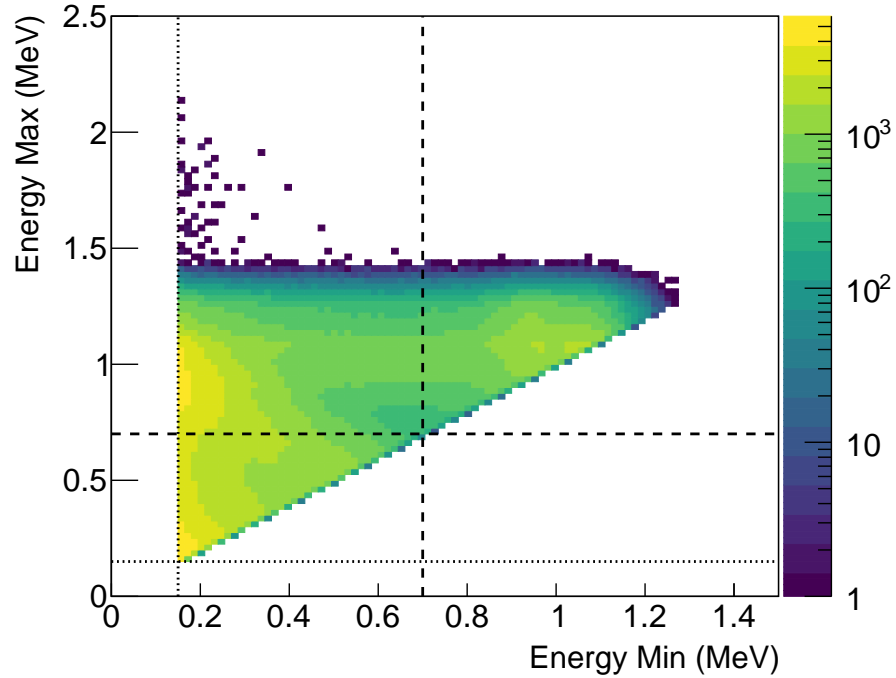

Figure 5.7: Maximal energy with minimal energy, for simulated Cobalt events, with source in position 5 (see Fig. 5.5b). High threshold is represented in black dotted line. Dashed lines materialise the individual energy selection.

individual energy selections, are represented. We observe single γ particles depositing energy successively in two optical modules, characterised by one

high energy hit (~ 0.8 MeV), and low energy hit (~ 0.2 MeV). The individual energy selection allow to reject this type of events.

- Geometrical selection: we want to avoid background events where one single γ interacts in two different scintillators (by two successive Compton interactions). Such events occur predominantly in neighbouring scintillators. With a well calibrated detector, the individual energy selection would have been sufficient to prevent such events to be selected. But, at the time of the data-taking, the detector was not fully calibrated, and the energy for some reconstructed particle hits might be badly estimated. Therefore, some background events could pass this energy selection. Consequently, we reject events where two neighbouring optical modules detect signal in coincidence.

These four selections aim to improve the signal to background ratio. The coincidence time selection is only applied on real data, while others are applied both on simulations and real data. In fact, the signification of an *event* is not the same for simulations as for real data: we simulate one Cobalt disintegration after another. *a réécrire* Each selection have an effiency

$$\varepsilon = \frac{\text{Number of selected events}}{\text{Total number of events}} \ . \tag{5.5}$$

Selection efficiencies are presented in table 5.1.

	Simulations	Data
Trigger	65%	1.8%
Time coincidence	-	test
Individual energy	3.4%	1.2%
Geometrical	3.4%	1.2%

Table 5.1: Selection efficiencies for simulations and real data.

5.2.5 Background estimation

In order to interpret the current analysis results, we aim to estimate and characterise the background detected by the SuperNEMO calorimeter, during the ^{60}Co data-taking time period.

As described previously, we aim to detect two γ's of 1.17 MeV and 1.33 MeV, emitted after Cobalt disintegrations. Therefore, we can mainly distinguish three different types of background, presented in Fig. 5.8.

- Photons coming from the natural radioactive decay chains of ^{238}U, ^{232}Th and ^{40}K isotopes. Typically, the 2.61 MeV-γ, from ^{208}Tl decay, can interact successively in two scintillators through Compton scatterings (see Fig. 5.8a).

- Through a double Compton interaction, a single Cobalt γ particle can deposit energy in two scintillator blocks (see Fig. 5.8b). As described in Sec. 5.2.4, the geometrical and individual energy selections have been set up to reject these background events.

- At the time of the data acquisition, the calorimeter was in commissioning phase, and the iron shielding was not yet installed. Therefore, the calorimeter was not properly protected from external particles, coming from outside the detector (radioactive isotope contamination of laboratory rock). Accidental events where two decorrelated γ particles, can be detected in two scintillator blocks (see Fig. 5.8c).
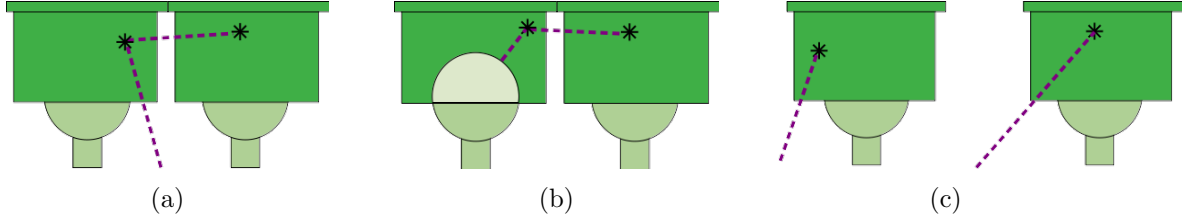

(a) (b) (c)

Figure 5.8: Background types for the Cobalt study. Interactions of photons in scintillators are represented by black stars. (a) Interaction of a single Cobalt photon in two scintillators through double Compton scattering. (b) Interaction of a photon coming from natural radioactive isotopes contamination (PM glass...), through double Compton scattering. (c) Interactions of two uncorrelated photons, coming from the demonstrator outside (natural radioactivity of laboratory rock...), in two scintillator blocks

All these three topologies can mimic the Cobalt two-γ's signal. A background acquisition, without the Cobalt calibration source, has been taken (see Sec.5.2.3). Unfortunately, be owing to energy calibration issues, these data are not usable. However, estimating the amount of background received by optical blocks during the acquisition is essential to assess our results.

We aim to provide an estimation background events, considering events detected by optical modules far from the Cobalt source. Needless to say, the data may contain signal events coming from Cobalt source, as well as background events, whose different origins are decribed above. We choose to modelise the Cobalt data as a linear combination of signal events s and background events b

$$\hat{d} = s + b\,, \tag{5.6}$$

where s and b are considered as uncorrelated. The question is how to extract informations about background, using the Cobalt data acquisitions. We remind the Cobalt source was placed at different positions behind the calorimeter wall (Fig. 5.5b, Sec. 5.2.3). We aim to take advantage of those different configurations to reach our goal. In the following, we make use of the positions 2 and 8 for the Cobalt source. Therefore, depending on whether the source is in one of the two positions, some optical modules are *close* to it, others are *far*. More precisely, we consider as *close*, the optical modules that are separated from the source by less than 10 OMs (i.e. less than half the wall-lenght), the others being *far* from it[2]. Considering that, we distinguish two categories of data, $\hat{d}^{\text{close}}$ and $\hat{d}^{\text{far}}$, defined as

---

[2]For example, an optical module located on the left (right) of the calorimeter wall, is considered as far from (close to) the source, if the source is in position 8.

the estimations of data events detected by an optical module when the source is close, or far to it, respectively. Then, we precise our data modelisation with

$$\hat{d}^{\,\text{close}} = b + s^{\,\text{close}} \, , \tag{5.7}$$

where $s^{\,\text{close}}$ is the number of signal events detected by a given optical module for which $D_{\text{source}} < 10$. In the same way, considering $s^{\,\text{far}}$ as signal events detected by an optical module from which the source is far, we have

$$\hat{d}^{\,\text{far}} = b + s^{\,\text{far}} \, . \tag{5.8}$$

We use ^{60}Co simulations to gather informations on $s^{\,\text{close}}$ and $s^{\,\text{far}}$ estimations. For this purpose, we define the coefficient α as

$$\alpha = \tilde{s}^{\,\text{far}} / \tilde{s}^{\,\text{close}} \, , \tag{5.9}$$

which depends on the distance D_{source}, and we find $0.05\% < \alpha < 5\%$ for ^{60}Co simulated events, meaning that the number of signal events detected by optical modules distant from the source is greatly lower than for close optical modules, for a given source position.

In order to provide a non-biased estimation of b, given the data model in Eq. (5.8), we would remove $\tilde{s}^{\,\text{far}}$ (estimated through simulations) from $\hat{d}^{\,\text{far}}$ (estimated with Cobalt data acquisition). However, qualitatively comparing data and simulations is not straightforward, especially due to detector efficiency considerations, discussed in Sec. 5.2.6. Nevertheless, we can give an order of magnitude of the amount of background events detected. To do so, we display in Fig. 5.9 the number of calorimeter hits, after data selection, counted by each optical module, as a function of the distance to the Cobalt source. The 10 OMs limit is materialised by a vertical dashed line. Calorimeter hits that occurred in coincidence above and below this limit are displayed both for simulated and real data. Therefore, events where the two hits occur in two optical modules, each located in one half of the calorimeter, are not represented. This explains the observable gap at the 10 OMs limit level.

We first focus on simulation results. Calorimeter hits for which $D_{\text{source}} < 10$, represent the estimation of the amount of signal events detected close to the source, $\tilde{s}^{\,\text{close}}$. Similarly, hits for which $D_{\text{source}} > 10$ embed for $\tilde{s}^{\,\text{far}}$, the amount of signal events remaining for optical modules far from the calibration source site. As expected, the number of signal Cobalt events decreases with the distance to the source.

We then compare data events with simulations. Calorimeter hits for which $D_{\text{source}} < 10$ materialise the number of data events estimation $\hat{d}^{\,\text{close}}$. Apart from slight differences, discussed in Sec. 5.2.6, these data events follow the same evolution as signal events with the distance to the source. This leads us to conclude that optical modules close to the source are dominated by Cobalt signal events. Similarly, $D_{\text{source}} > 10$ events stand for $\hat{d}^{\,\text{far}}$. We observe that $\tilde{s}^{\,\text{far}} / \hat{d}^{\,\text{far}} \ll 1$, which is compatible with the α coefficient values, being 5% in the worse case, explaining the few amount of $\tilde{s}^{\,\text{far}}$ events remaining for optical modules far from the source. Moreover, we find that the amount of $\hat{d}^{\,\text{far}}$ events is globally stable
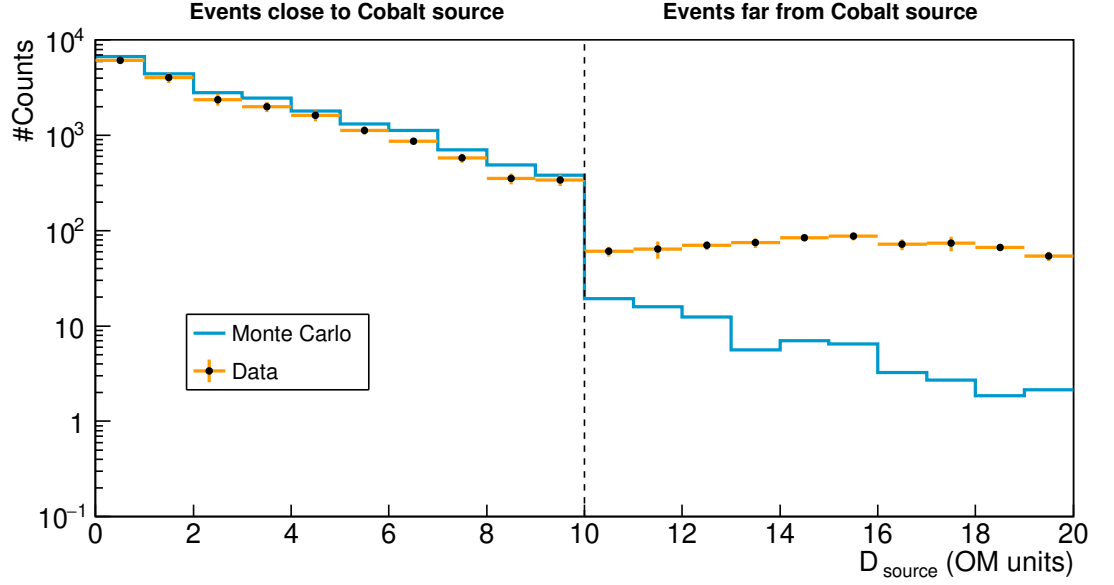
Figure 5.9: Number of events for pairs of OMs on the source side and on the opposite source side, for real data (green) and simulated data (red), as a function the distance to the source (in units of number of OM). The vertical dotted line materialises the distance limit of 10 OMs from the source.

with the distance to the source. Therefore, we assume that optical modules away from the ^{60}Co source by more than 10 OMs are background dominated. As this amount of background is comparable for all optical modules, regardless of their distance to the source, we conclude that these events are decorrelated from the Cobalt source, and come from other sources (as external γ's). Therefore, for a 25 minutes run, each optical module detects around 10^2 external background events.

To sum up these results, calorimeter hits for optical modules close to the Cobalt calibration source are, for the most part, signal events. Besides, hits occurring far from the source are predominantly background events. As we moved the source in different positions, we have access to the estimation of background rate $\hat{b}$ for each optical module (when the source is far), and to the estimation of $\hat{s}$ (when the source is close). Therefore, we can compute the signal to background ratio, as a function of the distance to the Cobalt source, displayed in Fig. 5.10. The number of signal events in each optical module depends on the distance to the source, which is not the case for the number of background events, explaining the decreasing of S/B with D_{source}.

To summarise, in this subsection, we gave informations on background events for the whole French wall, using data taken with the Cobalt source set at different positions. We confirmed our assumption that the more one optical block is far from the source, the less it detects γ particles emitted after Cobalt disintegrations, then the more the signal to background ratio decreases. In the following, in order to properly compare simulated and real data, we give an order of magnitude of the detector efficiency during the data-taking with the Cobalt source.
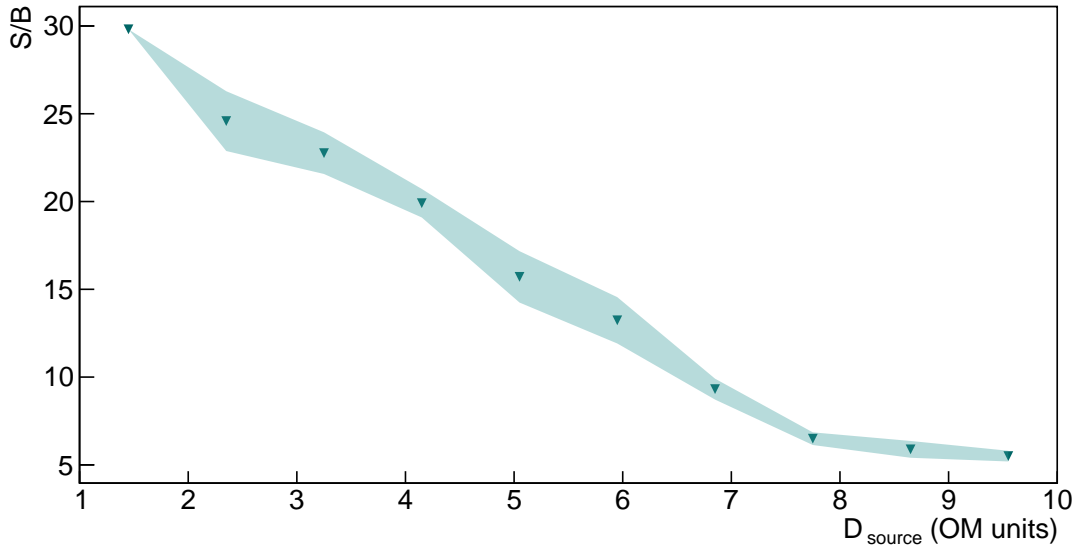
Figure 5.10: Signal to background ratio for each optical module, as a function of the distance to the Cobalt source.

5.2.6 Detector efficiency

The last step before going into detail in optical modules' timing resolution study is to determine the detector efficiency of the SuperNEMO demonstrator, during the Cobalt acquisition week.

Standing as an example, we compare real and simulated energy spectra for a given pair of optical modules detecting events in coincidence. We provide these spectra in Fig. 5.11, where events satisfy to the four criteria described in Sec. 5.2.4, for the Cobalt source in position 5. The simulated data are normalised to the source activity and acquisition time.

Firstly, the energy resolution of the calorimeter blocks. Secondly, at the time of the data taking, optical modules where not equalised in gain. The real data energy spectrum is also characterised by a high energy part. This may be due to external background events, which are not taken into account in the simulated data. In Sec. 5.2.5 is presented a background analysis to investigate the high energy part of the energy spectrum, and better understand the data.

* a finir *

5.2.7 Determination of the individual timing resolution of each optical module

Time difference distributions

The final goal of this analysis is to determine the time resolution of optical modules, due to the scintillator time dispersion. As displayed in Fig. 5.3, the two photons of Cobalt 60 are emitted in coincidence. The selections described in Sec. 5.2.6 aim to maximise the signal to background ratio, the signal being the detection of two γ's interacting in two different optical modules. The two γ's, travelling at
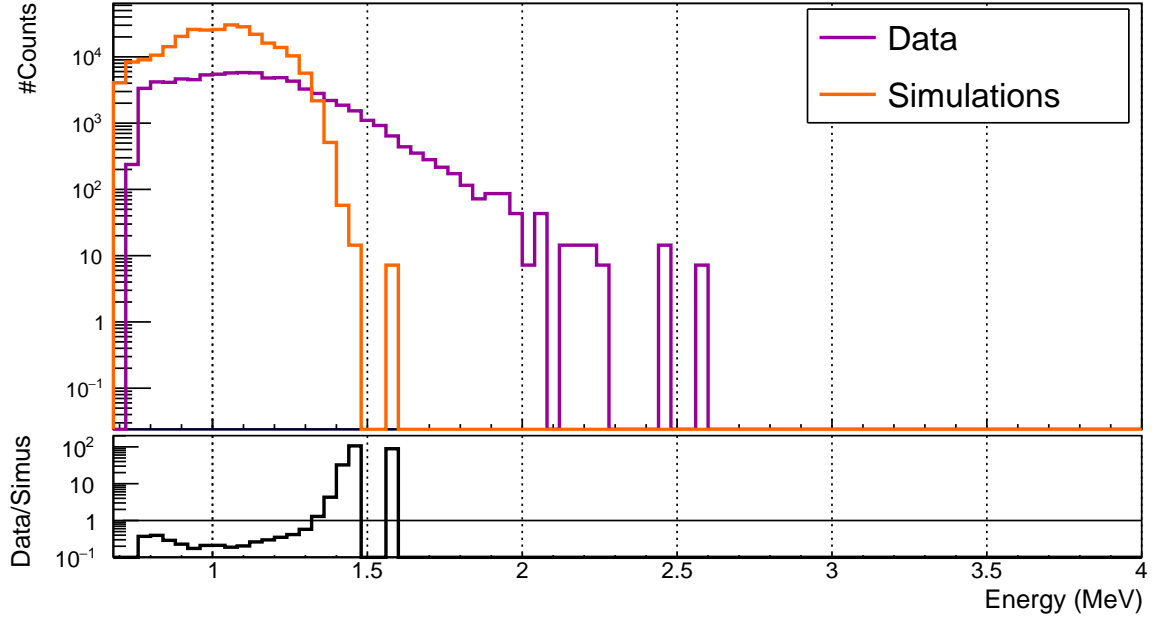
79

Figure 5.11: Top pad: energy spectra for simulated data (orange solid line) and real data (purple solid line) in logarithmic scale. Bottom pad: ratio of real data over simulated data for each bin in logarithmic scale.

speed of light in air, reach the two optical modules at two different times. The time of a calorimeter hit t_i^γ, describes in Fig. 6.3 in Chapter 6, is defined from the collected charge sampling at PM anode and received by the electronic readout. We then look for topologies where two calorimeter hits occurred in a given time window of 62.5 ns. This coincidence time window where chosen to select the two Cobalt γ's coincidence events, avoiding accidentals. A first event occur in one of the scintillator of the wall, meaning the amount of charge is high enough to pass the high amplitude threshold. In the considered coincidence time window, a second particle interacts in another scintillator. This topologies are likely to happen for all combinations of pairs of PMs (given the distance between the two optical modules). Therefore, we can construct a Δt^{pair} distribution for each pair of OM, defined as the time difference between two calorimeter hits $\Delta t^{\mathrm{pair}} = t_A^\gamma - t_B^\gamma$. Here, one of the two optical modules, namely the A, is chosen as reference.

In Fig. 5.12 is presented an example of a Δt^{pair} distribution, for a given pair of optical modules, both for the simulated and real data, with the Cobalt source placed at the central position behind the calorimeter wall. The two distributions present different behaviours in terms of means and standard deviations. This can be explained by two distinct reasons.

Firstly, as exposed in Sec. 5.2.2, in the framework of this study, the calorimeter part of the SuperNEMO demonstrator was considered as perfect in terms of time reconstruction, in the simulation processed. All optical modules' time resolutions, whose main contributions are presented in Sec. 5.2.2, were set to 0 ns. We retrieve such a setting in the Δt^{pair} distribution for simulated data. As a consequence, the standard deviation, for this pair of optical module, is higher for real data than for simulated data. Even though the case presented is just an example for a given
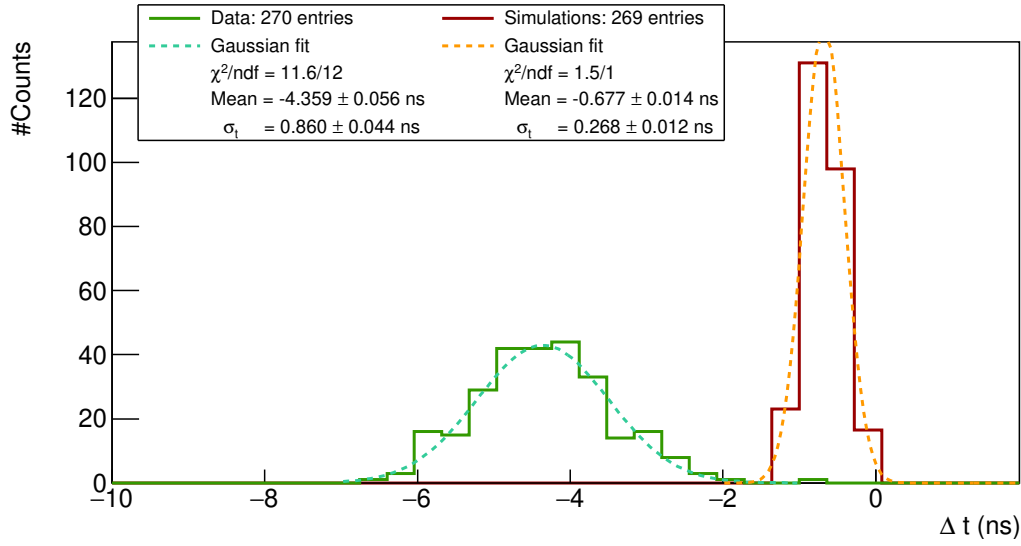
Figure 5.12: Δt^{pair} distributions for real data (green solid line) and simulated data (dark red solid line). Two Gaussian fits (orange and blue dotted line) are displayed and fit parameters are given in the legend. The two distributions do not have the same mean because optical modules are not aligned in time. However, this does not disturb the time resolution measurements.

pair of OM, we will see this is a general result for all pairs of optical modules.

Secondly, at this time, some differences remain between what is simulated and the real demonstrator performances. In fact, as the demonstrator is in commissioning phase, some calorimeter detection characteristics are not yet included in the Falaise simulations, and affect the real data results (characterisation of optical modules' energy resolution, implementation of particle time arrival shifting due to coaxial cables...). We observe such differences in the two distributions means: the data distribution is shifted by 3.7 ns compared to the simulation distribution. This result was expected: for the moment, the Falaise software does not take into account, in the reconstruction process, the time made by the electric signal to travel from a PM divider to the electronic readout, discussed in Sec. 6.1 of Chapter 6. In other words, the time difference distribution for a given pair of optical module is affected by the difference of lengths of the two coaxial cables. This is an important parameter directly affecting the mean time difference between two distinct optical modules detecting particles in coincidence. Although simulations do not perfectly picture the full detector performances, real data and simulation can be compared, since we understand these differences. Moreover, both the real and simulated data are affected by parameters such as the distance from the Cobalt source to the wall, or the distance between the two considered optical modules.

A Δt^{pair} distribution exists for each pair of optical modules detecting two events in the time coincidence window. The least square method is used to fit the distributions, which minimises the difference between the measured value and the fitted value. A mean and a standard deviation is then defined for each pair of optical module whose fitted data has $\chi^2/\text{dof} < 4$. Therefore, each pair of optical

module is characterised by the mean and standard deviation of its corresponding Δt^{pair} distribution. The standard deviation, noted as σ_t^{pair} in the figure legend, corresponds to the uncertainty on time measurement for this peculiar pair of OM. Therefore, a value of the time uncertainty σ_t^{pair} can only be given for a proportion of total optical modules.

As the detector in commissioning phase, the acquisition was taken with 254 optical modules[3]. In this study, we only consider 8 inches PMs, hence this analysis aims to characterise the time resolution of 214 OMs, representing 22791 different possible combinations of pairs. In Fig.5.13 are presented the σ_t^{pair} values, both for simulated and real data. In the first place, we notice the mean σ_t^{pair} value

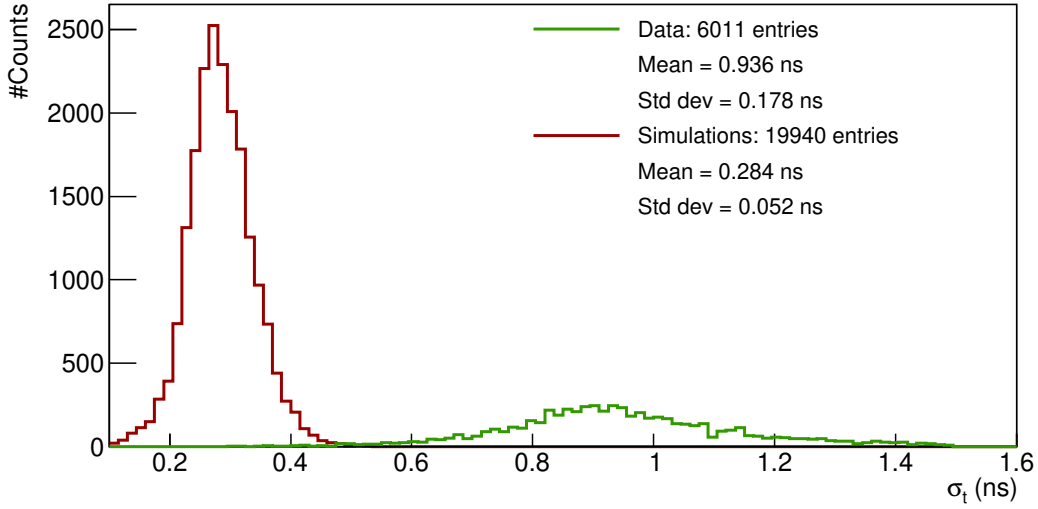Figure 5.13: σ_t^{pair} distribution for pairs of optical modules.

for simulations is lower than for real data. As explained above, this difference is caused by the perfect calorimeter time resolution for simulations on one side, and by the detector characteristics not yet implemented in the simulation software on the other side. This second statement is also behind the larger value of the real data distribution's standard deviation. In fact, for the simulated case, Δt distributions, of which an example is given in Fig. 5.12, have comparable σ_t^{pair} values, for all pairs of optical modules. This is not the case for the real data: the σ_t^{pair} value for a given pair of OM depends on the difference between the two coaxial cable lengths. And this length difference being specific for each pair of optical module.

Moreover, we succeeded characterising σ_t^{pair} values for 26% of pairs of optical blocks for real data, against 87% for simulations. In fact, the more one optical module is from the source, the more it is background dominated. As we explained, such a value is provided for a OM pair only if the fit of the corresponding Δt^{pair} distribution is of high-quality. Therefore, the optical modules for which the fit

---

[3]Three OMs are damaged on the French wall (*ref commissioning*) and three photomultipliers were not well aligned in gain at this time, and had to be removed from the analysis.

successes are the ones around the source. This is not valid for simulations are we only have Cobalt events, and no background is simulated.

In Fig.5.14 is displayed the number of characterised optical blocks, with the distance between the reference block and the Cobalt 60 source, in units of block width. For a given distance from the source, the amount of characterised OM is
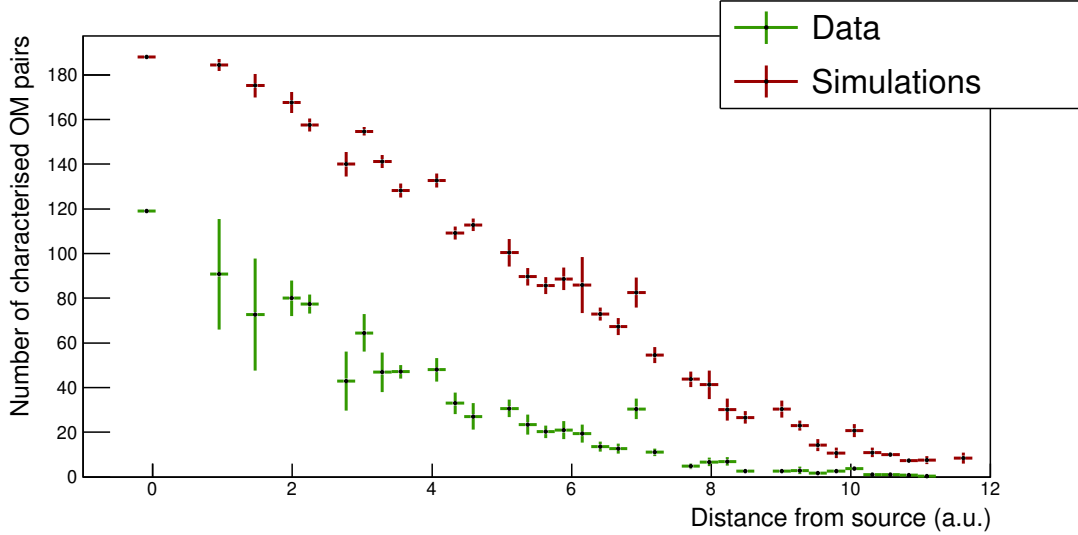

Figure 5.14: Number of characterised OM pairs, as a function of the distance between reference OM and source.

lower for the real data case than for the simulated one. This explains the different amount of characterised OMs for real and simulated data.

We presented results on the uncertainty on time measurement for pairs of optical module, σ_t^{pair}. However, we are interesting in providing such values, independently for each optical modules. Therefore, in the following, we present the algorithm we used to provide $\sigma_t^{\mathrm{indep}}$ values.

Decoupling of σ_t^{pair} values

We have determined σ_t^{pair} for some of the pairs of OMs on the French wall. For example, if we take the source closest OM (OM located at the centre of the French main calorimeter wall), it has coincidence events with a certain number of other optical blocks. Among them, 119 different Δt^{pair} distributions are fitted, therefore 119 values of σ_t^{pair} are stored. And this work is done for each counting optical module taken as reference. All following steps aim to determine the individual $\sigma_t^{\mathrm{indep}}$.

We want to evaluate this value for the closest OM from the source, let us number it 0. We have access to the number of coincidence events this OM has with each other OMs. We pick up the two OM that have the larger number of coincidence events with this reference OM, with their associated $\sigma_t^{\mathrm{indep}}$ and mean energies. We number them as 1 and 2. Therefore, to find the value of $\sigma_t^{\mathrm{indep}}$, we

have to solve a set of 3 linear equations:

$$
\begin{aligned}
(\sigma_t^{0,1})^2 &= \frac{(\sigma_t^0)^2}{\bar{E}_0} + \frac{(\sigma_t^1)^2}{\bar{E}_1} \\
(\sigma_t^{0,2})^2 &= \frac{(\sigma_t^0)^2}{\bar{E}_0} + \frac{(\sigma_t^2)^2}{\bar{E}_2} \\
(\sigma_t^{1,2})^2 &= \frac{(\sigma_t^1)^2}{\bar{E}_1} + \frac{(\sigma_t^2)^2}{\bar{E}_2} \, ,
\end{aligned}
\tag{5.10}
$$

where σ_t^i is the individual uncertainty on time measurement for the block i. Solving simultaneously these equations comes down to diagonalise the matrix S defined as

$$
S = \begin{pmatrix} 1/\bar{E}_0 & 1/\bar{E}_1 & 0 \\ 1/\bar{E}_0 & 0 & 1/\bar{E}_2 \\ 0 & 1/\bar{E}_1 & 1/\bar{E}_2 \end{pmatrix} .
\tag{5.11}
$$

We now generalise this method to all possible combinations of OM pairs for which we have informations on σ_t^{pair}.

Estimating the variance

5.2.8   Conclusion

- il nous faut des simus bkg

- il nous faut un run bkg

- ça marche bien

- il faudrait refaire une manip avec PMs alignés

- On aurait pu décorréler les sigmas en utilisant toutes les combinaisons possibles, mais il aurait fallu faire masse de simus pour déterminer les covariances

5.3   The Light Injection System

The SuperNEMO demonstrator is designed to have a long exposure time. In this context, calibration systems are necessary to control and calibrate the response of the detector. The so called *Light Injection* (LI) System will monitor the stability of the calorimeter response in energy to 1%. It consists in 20 Light Emitting Diodes (LED) at 385 nm, injecting light in each scintillator block via optical fibers. A set of reference optical modules (PMTs coupled with scintillator blocks), receiving light from both LEDs and ^{241}Am sources, monitors the stability of the LEDs. A scheme of the complete LI calibration system is given in Fig. 5.15.

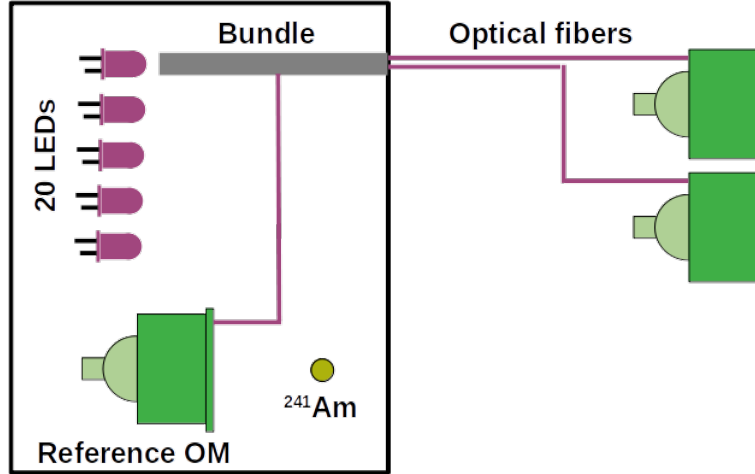First LI commissioning data was taken in March 2019.

Figure 5.15: The Light Infection (LI) calibration system is schematised. More than 1300 fibers, distributed in 20 bundles, carry the light from 20 LEDs to each scintillator block of the demonstrator. Reference OMs coupled with ^{241}Am sources monitor the LED light.

5.3.1 Light injection system commissioning

In the LI system design, the SuperNEMO demonstrator has been segmented in 10 areas. Each area receives light from one given LED
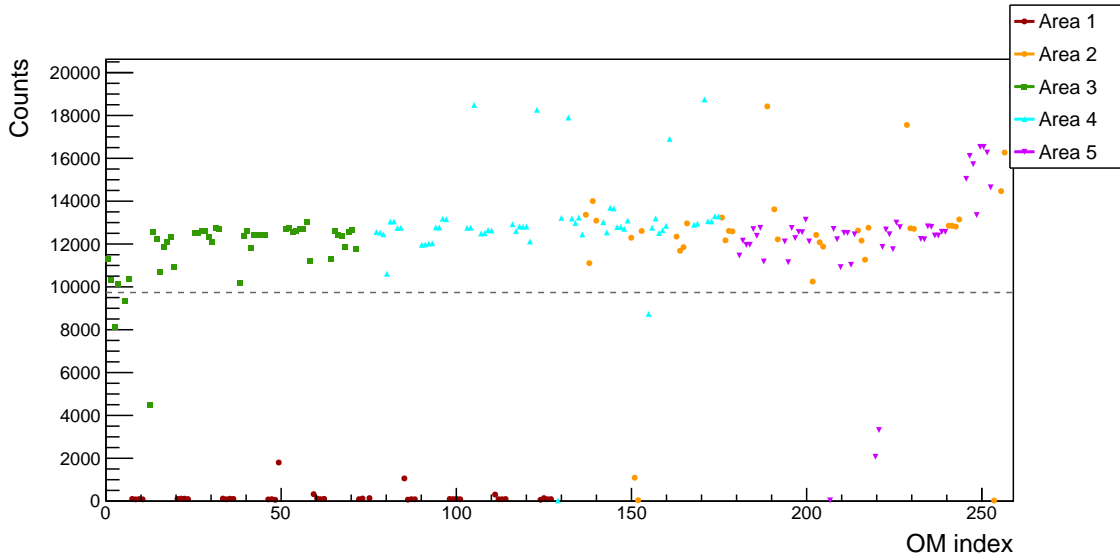
Primary/secondary Each LED lights Group LEDs/area

Figure 5.16: The number of counts is displayed for each optical module, labelled by the *OM index*. Each coloured marker represents counting rates for one area of the detector, that is to say one group of optical modules lighted by the same LED. The area 1 (dark red dots) is not receiving light from its corresponding LED.

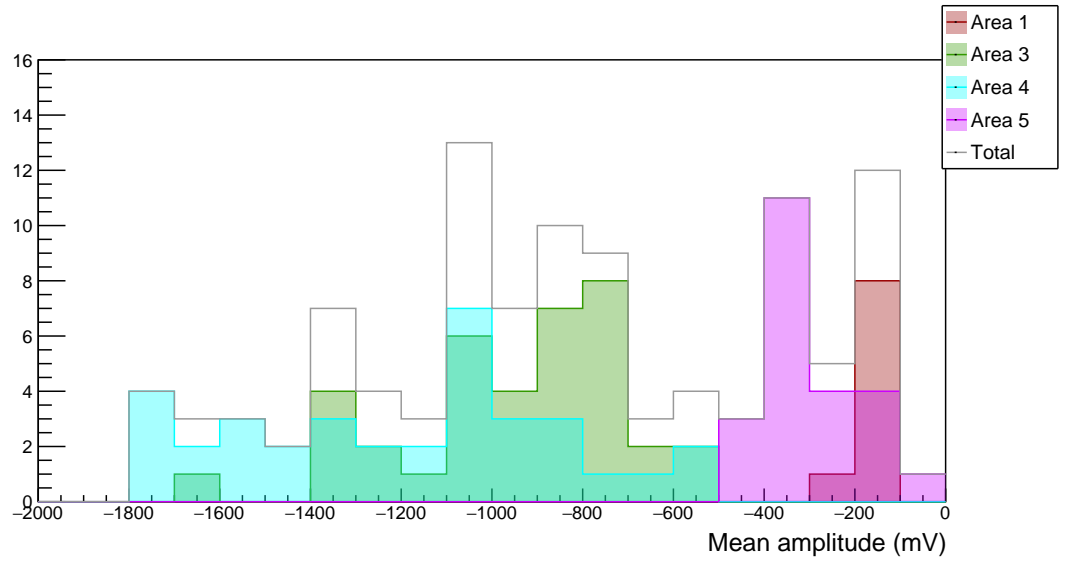## 5.3.2 Time resolution of optical modules

Figure 5.17: The mean signal amplitude distribution for each optical module is presented. One colour stands for one area of the half detector. In Grey is the total mean amplitude distribution.

Detector commissioning

The commissioning of the SuperNEMO demonstrator has begun in 2019 and first calorimeter data was taken.

The calorimeter of SuperNEMO is segmented in 712 optical modules (OM), each composed by a coupling between a photomultiplier tube (PMT) and a polystyrene scintillator bloc (see Sec. 2.1.5.2 for more details). The divider of a PMT is connected to 2 cables, one providing the high voltage (HV), the other one, called signal cable, is a coaxial cable collecting and transporting the charge provided by the PMT.

By the summer 2020, the SuperNEMO demonstrator will be encapsulated in an anti radon tent. The so called *patch panel* will insure passage of cables from the inside, to the outside of the anti radon tent, therefore doubling the amount of cables needed for the calorimeter. We refer to the cables running from detector to patch panel as *internal* cables, and the cables from patch panel to the electronic boards as *external* cables. Consequently, regarding only the calorimeter part, 2848 cables were cut, assembled, connector-mounted, transported and installed at LSM. Then the check of every cable condition is mandatory to control and eventually fix them.

6.1 Reflectometry analysis

6.1.1 Goal of the reflectometry analysis

Taking into account the final demonstrator design, each coaxial length was determined, cables were cut and labelled in LAL, Orsay. All external coaxial cables were designed to be 7 meters-long – the distance between electronic boards and patch panel being the same for all channels at electronic boards – and internal cable lengths have been adapted to fit the distance from the patch panel to each optical module. Then, cutting and labelling all cables lasted several weeks. After all cables were transported and installed at LSM, we had to check each coaxial cable condition, for several reasons:

- check if no cable was damaged during the transport and the installation;

- control if no swap between cables has been made during cable labelling or calorimeter cabling,

- check if the coaxial cable was cut at the right length,

- more importantly estimate the signal time delay due to the cable lengths: knowing that the velocity of electrons in the coaxial cables has a known constant value, the longer is the cable, the more the signal takes time to travel from the PMT to the electronic channel. Therefore, each coaxial cable length has to be characterised, especially if we want to do time coincidences between two signals in two different channels.

To do so, a pulse, called *primary* pulse, is generated at the electronic board readout. The signal will travel all along the coaxial cable, from the electronic board to the PMT divider. Whether the cable is correctly connected to the PMT or not, the signal reflects at the other end. Then the signal travels back from the PMT to

(a) Normal reflection at PMT divider.

(b) Cable not connected at PMT.
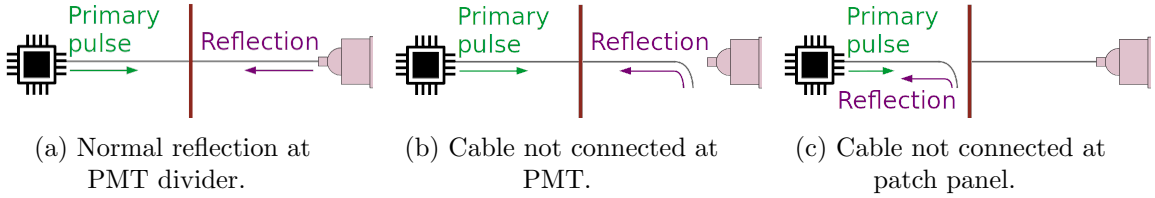
(c) Cable not connected at patch panel.

Figure 6.1: A representation of pulses sent in a cable for the reflectometry analysis is given. The electronic boards are symbolised by the black chip, and the patch panel by the red vertical bar. Three scenario where a primary pulse is sent in one cable (represented in grey), are represented. (a) The cable is well connected at the patch panel and at the PMT. The signal reflects at the PMT divider. (b) The cable is not connected at PMT and the signal is reflected at the end of the cable. (c) The cable is not connected at patch panel and the signal is reflected at the end of the external cable.

the electronic board channel, where it is recorded by the acquisition. We called this recorded reflected pulse *secondary* pulse. An example of the total recorded signal is displayed in Fig. 6.3a. In order to accumulate enough statistics, we send thousands of pulses in each coaxial cable. The analyses of the shape and of the arrival time of those secondary pulses for each channel is called *reflectometry*, and allow us to check the coaxial cable conditions and to control their lengths.

6.1.2 Pulse timing: controlling cable lengths

The first step of this analysis is to experimentally determine the length l_j^m for all signal cables j installed on the demonstrator. This length is defined as

$$l_j^m = 0.5\, t_j\, v_p\,, \tag{6.1}$$

where t_j stands as the time made by the electrons to do a round trip between one electronic channel and one PMT, and v_p is the velocity of electrons in the coaxial

cables, which can be expressed as a fraction of light speed in vacuum, c. The time difference t_j between the primary pulse and the secondary pulse is written as

$$t_j = \langle t_{\text{secondary pulse}} - t_{\text{primary pulse}} \rangle_p \,, \tag{6.2}$$

$\langle \rangle_p$ being the average over all pulses sent in one single cable j. The velocity v_p is supplied by the cable manufacturer as

$$v_p = \frac{c}{\sqrt{\epsilon_r}} \,,$$

with ϵ_r the relative dielectric constant of the material. Therefore, this celerity depends on the components. For the coaxial cables chosen in the demonstrator design, the data sheet of the cable gives $v_p = 0.69\,c$. A study is performed to verify experimentally the value of v_p. Three cables of different lengths are measured with a precision of 1 cm. A thousand of primary pulses are sent in each of the three cables, then the time for each secondary pulse is recorded. At the end, we have three independent measures of the velocity v_p in the used coaxial cables. In Fig. 6.2 is displayed the lengths l_j as a function of the times t_j. The fitted value
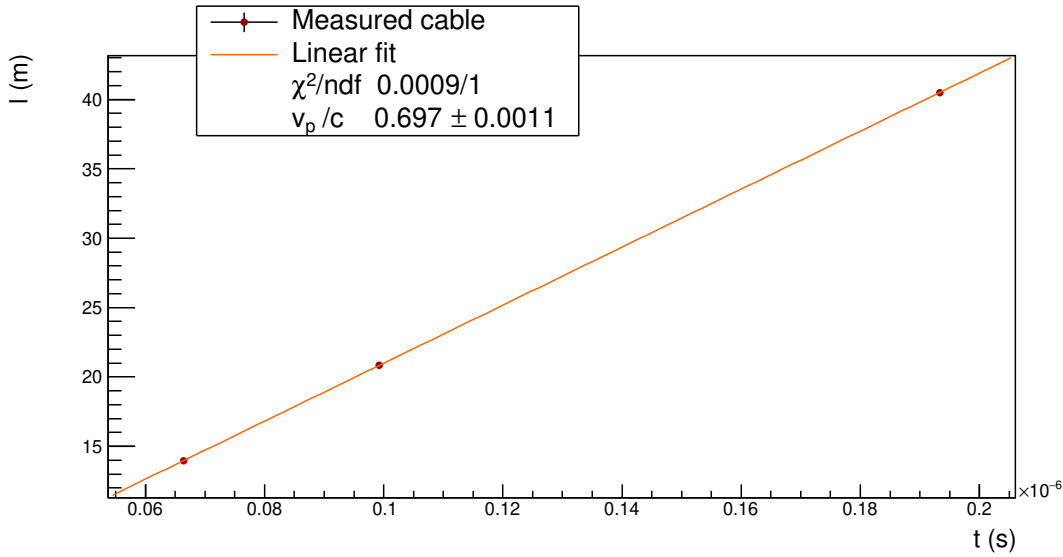

Figure 6.2: Three different lengths l_j of cables are measured. Pulses are sent inside all cables. The lengths l_j are plotted as a function of the time differences t_j between primary and secondary pulses. The value of v_p/c fitted from the data points is displayed. This value of 0.697 ± 0.0011 shows the compatibility with the one supplied by the constructor, of 0.69 c.

of $v_p/c = 0.697 \pm 0.0011$ is displayed and shows a compatibility up to 7σ with the data sheet.

As we want to determine the time interval t_j, we have to define what is the *time* of a pulse. In this analysis, we use a technique called Constant Fraction Discriminator (CFD), providing an amplitude-independent information about time of a pulse. This algorithm aims at tracking a signal and defining its time arrival at a given fraction f of its maximal amplitude. The two main advantages of this

technique is that it provides an efficient rejection of the noise in the acquisition window, and gives a good resolution on the measured time. Nevertheless, the possible influence of the chosen value for the f parameter on this time resolution has to be investigated. We perform such a study in Sec. **??**. We concluded that the highest precision on the time measurement arises for $f = 40\%$, and we adopt this value for the following analysis. A graphic representation of the CFD time search is given in fig. 6.3b. As we want to measure the installed cable lengths l_j^m,

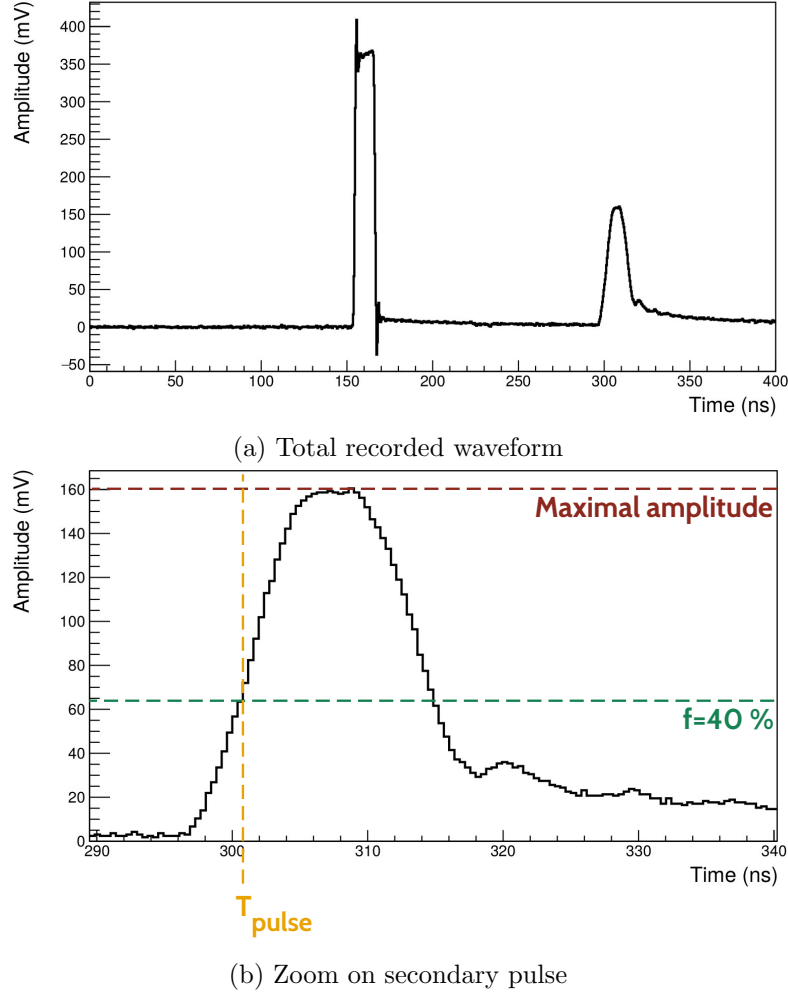(a) Total recorded waveform

(b) Zoom on secondary pulse

Figure 6.3: (a) Total recorded waveform: primary pulse (left) and secondary the pulse (right). (b) Zoom on the secondary pulse. A representation of time computed with a Constant Fraction Discriminator (CFD) is provided. Its maximal amplitude (red dotted line) and its fraction for f = 40% (green dotted line) are displayed. The time T_{pulse} (orange dotted line) represents the time of arrival of the secondary pulse computed with CFD, with the fraction f = 40%.

and compare them to the initially designed ones, l_j^d, we define the length difference ΔL_j as:

$$\Delta L_j = l_j^m - l_j^d . \tag{6.3}$$

In Fig. 6.4 is displayed the distribution ΔL for all the measured lengths. In hypothetical perfect conditions, all the cables should fit the design length, in other
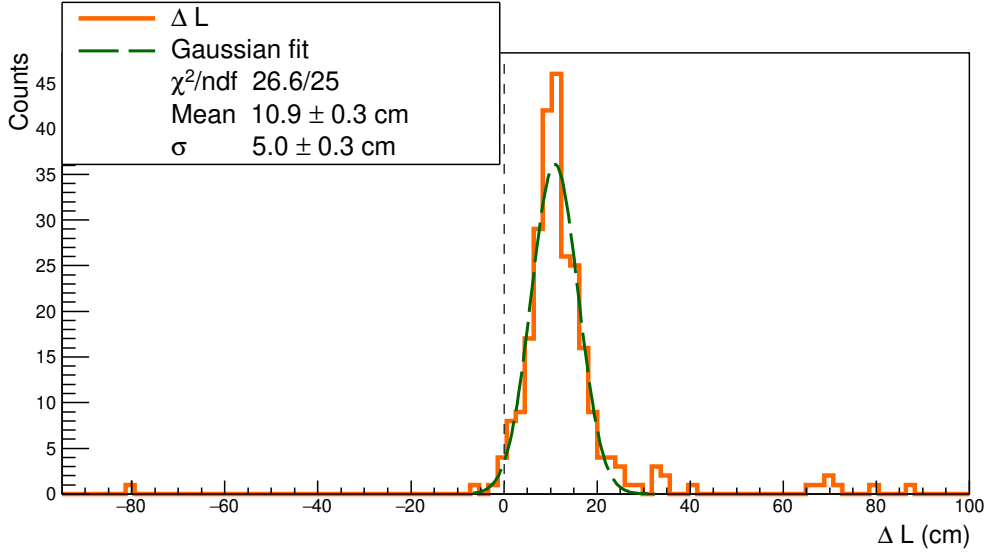
Figure 6.4: The distribution of difference between the measured lengths l^m and the expected lengths l^d is displayed in orange solid line. The black dashed line represents the case where $l_j^m = l_j^d \ \forall j$. The Gaussian fit (green dashed line) presents a mean of 10.9 ± 0.3 cm. Some data points considered as outliers are beyond 3σ.

words, $l_j^d = l_j^m$. Consequently the ΔL distribution should a peak at zero, as materialised by the black dashed line. However, in real conditions, the measured length can be different from the designed one, leading the ΔL distribution plotted in orange solid line. We conclude that the observed cable length l^m differs from l^d by $+10.9 \pm 0.3$ cm, meaning that cables are longer than expected in average. This may reveal a bias coming from the device used to cut the cables. In fact, during cable cutting work, we noticed that the cutting device had a tendency to slip, probably leading to cables with extra lengths. We assumed the cutting device has a given probability to slip for one meter of cable. If this is the case, the probability for the device to give extra length should increase with the cable length.

To verify this assumption, we plot in Fig. 6.5 the length difference ΔL as a function of the initial design length l^d (cyan). From those data points, we compute a linear fit (orange solid line), parameterised as $y = \alpha x + \beta$, revealing that the cutting device presents two different biases. The value of β shows that the cutting device systematically took away 3.4 cm of each cable. Nevertheless, as the shortest cable was designed to be 10 meters long, there are no important consequences of this bias on the length difference ΔL. Besides, the slope $\alpha = 0.010 \pm 0.002$ of the linear fit reveals that the cutting device adds one centimetre for every meter of cable, being compatible with the hypothesis on the cutting device sliding. Hopefully this bias is not problematic as it makes most of the actual cable lengths longer than the design, while shorter lengths could have lead to systematic connection issues to PMTs. However, we notice that a few cables have been cut too short by mistake, the worse of them being 80 centimetres shorter than expected. Fortunately, this cable was successfully connected to PMT despite this deficit. On the contrary, few cables have a large extra length. This probably is due to human punctual mistakes on top of the observed bias, but without any strong
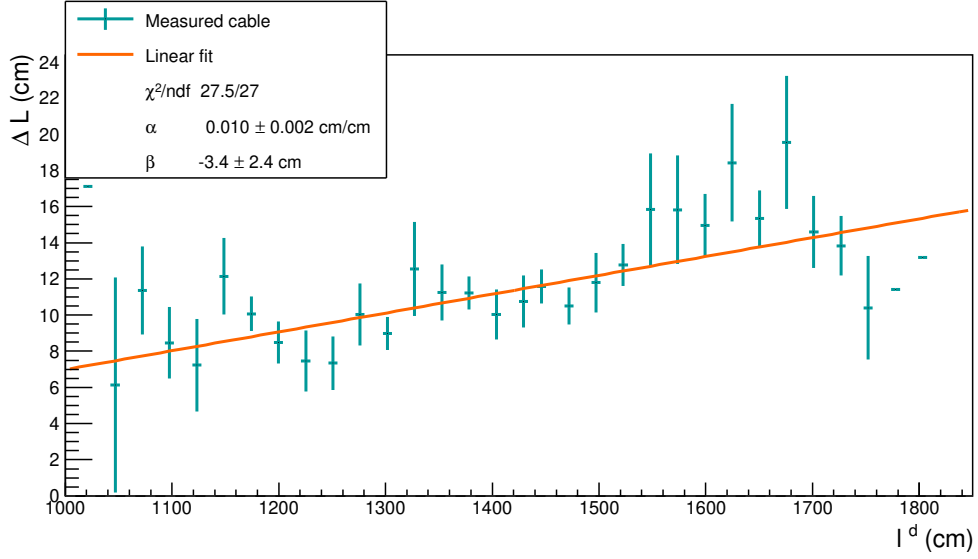
Figure 6.5: ΔL is plotted with l^d (cyan), where l^d is averaged for all the lengths designed to have the same value, being at the origin of vertical error bars. In black dashed line is represented the case where $l^m = l^m$. Data points are fitted by $\alpha x + \beta$, with $\alpha > 0$ and $\beta < 0$, revealing the two biases of the cutting device.

consequences for the calorimeter operation. In conclusion, no important mistakes have been made when cutting cables, and we had no issue for connecting the only problematic cable.

If the main goal of this study is to check the lengths of coaxial cables, it also aims at correcting the time of recorded events, from the time made by the signal to travel from a PMT to an electronic channel. taking into account the time for the signal to travel through cables. This become possible with the reflectometry study we performed. Knowing real lengths of cables and using the celerity of the signal, we deduce the time needed for the signal to travel from one given PMT divider to the electronic boards. Then we can correct event times.

As explained previously, the time t_j gives information about the length of the cable j. We remind the coaxial cables are divided in two parts, one external and one internal, both linked by the so-called patch panel. Thus we can use that travel time to detect possible disconnection of a cable at patch panel. In fact, if one cable is not connected at the patch panel – this case is illustrated in Fig. 6.1c, – the pulse reflects at the end of the external cable part, going back to the electronic board. This very short time, giving information about the location of the reflection, is used to tag a patch-panel disconnection. Then, a simple check onsite can confirm this observation, and the external part of the cable can be connected to the patch panel.

This study allowed us to control and record the lengths of all coaxial cables installed on the SuperNEMO demonstrator at LSM, and gave information on the status of cable connections at patch panel. We also have understood the main results on measured cable lengths and the functioning and biases of the cutting device that we used.

6.1.3   Signal attenuation

The attenuation of an electric signal is a problem common to all electronic fields, and comes from the charge loss of an electromagnetic wave travelling in a medium. For a coaxial cable, this attenuation mainly depends on the signal frequency f in MHz and on the cable characteristics. For the coaxial cables, the theoretical linear attenuation α_{att}^{th}, so be it the attenuation by metre of cable in dB/m, is supplied by the constructor as

$$\alpha_{att}^{th} = f\sqrt{\epsilon}(\frac{a}{\sqrt{f}} + b)\,, \tag{6.4}$$

where the factor a depends on the diameter of the dielectric material on one side, and of the diameter of the conductor material on the other side, and where b is function of the dielectric loss factor, characterising the material's dissipation of electromagnetic energy. For the used coaxial cables, and with a frequency f of few GHz for the signal pulses sent in cables, we calculate this attenuation as $\alpha_{att}^{th} = 1.22$ dB/m. In a more general manner, the attenuation of a signal in dB is defined with the decimal logarithm of a power ratio. We use this definition to determine the attenuation in the framework of the reflectometry analysis, defining the attenuation $\mathcal{A}$, for a given length of cable l, as

$$\mathcal{A} = 10\log_{10}\frac{V_{\text{primary pulse}}}{V_{\text{secondary pulse}}}\,, \tag{6.5}$$

where V_i is a quantity representing the intensity of the signal. V can correspond to the maximal amplitude of the pulse, as well as the *integrated charge* of the pulse, defined as the amount of current received by the acquisition over a given time window. As the provided data sheet does not specify the attenuation of which quantity (amplitude or charge) represents α_{att}^{th}, we decide to investigate both in the following. Then, we define the linear attenuation α_{att}^{R}, measured by reflectometry in dB/m, with

$$\mathcal{A} = f_r + \alpha_{att}^{R}\, l\,, \tag{6.6}$$

with $f_r = -10\log_{10}R$, where R is the reflection factor characterising the pulse reflection on the PMT divider. In fact, as the circuit is opened, the pulse is reflected at the PMT divider, but only partially. A part of the signal is not reflected but lost through the divider. This reflection is characterised by R, which is function of the impedance Z_c of the cable, and of the impedance Z_d at the divider level, where the pulse is reflected. It is written as

$$R = \frac{Z_d - Z_c}{Z_d + Z_c}\,, \tag{6.7}$$

where we have the limit

$$\lim_{Z_d\to\infty} f_r = 0 \text{ and } R = 1\,, \tag{6.8}$$

expressing a total reflection occurring when the impedance at the PMT divider is infinite. The main goal here is to determine the value of α_{att}^{R}, using the reflectometry data, and to compare it with α_{att}^{th}. Moreover, the impedance Z_d

value at PMT divider can be estimated from the determination of f_r. In Fig. 6.6 is shown the linear dependence between the attenuation $\mathcal{A}$ and the cable length l, and two data set are presented. The cyan scattered markers represent the attenuation calculated from the amplitude ratio $A_{\text{primary pulse}}/A_{\text{secondary pulse}}$, and the magenta markers correspond to the attenuation calculated from the charge ratio $Q_{\text{primary pulse}}/Q_{\text{secondary pulse}}$. The amplitude A_i is given in mV and the charge Q_i in mV.ns. The values of $\alpha_{\text{att}}^{\text{R}}$ and f_r, for both amplitude and charge cases, are
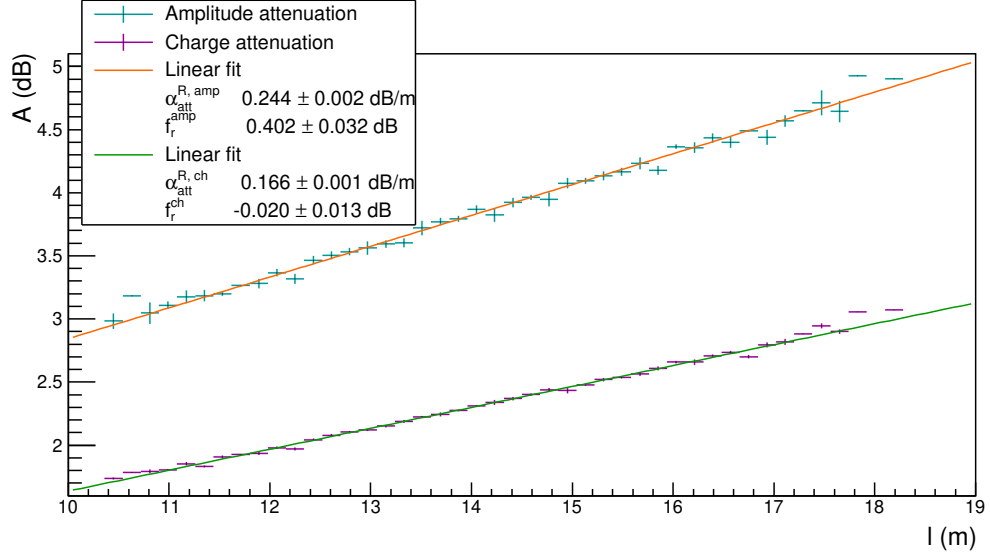

Figure 6.6:   The amplitude $\mathcal{A}$ is displayed as a function of the measured cable length l. The data set calculated with the amplitude (charge) is given in cyan (magenta) and fitted by a linear function in orange (green). The values of the slope, which represent the linear attenuation of the coaxial cables in dB/m, are respectively $\alpha_{\text{att}}^{\text{R, amp}} = 0.241 \pm 0.000\,\text{dB/m}$ and $\alpha_{\text{att}}^{\text{R, ch}} = 0.166 \pm 0.000\,\text{dB/m}$. The two y-intercept values, which represent the reflection of the pulse on the PMT divider, are $f_r^{amp} = 0.402 \pm 0.032$ dB and $f_r^{ch} = -0.020 \pm 0.013$ dB.

displayed in the legend. Firstly, the two linear fits reveal that, whether calculated with the amplitude, or with the charge, the linear attenuation $\alpha_{\text{att}}^{\text{R}}$ is smaller than the calculated one $\alpha_{\text{att}}^{\text{th}}$ (for the amplitude case, $\alpha_{\text{att}}^{\text{th}} \simeq 5 \times \alpha_{\text{att}}^{\text{R, amp}}$, and for the charge case $\alpha_{\text{att}}^{\text{th}} \simeq 7 \times \alpha_{\text{att}}^{\text{R, ch}}$). That means the signal is less affected, when transmitted by the cable, than expected. Secondly, the attenuation in charge is less important that the attenuation in amplitude. This can be easily explained: as it is integrated over time, the charge is a quantity less affected by amplitude variations that the amplitude itself. For the same reason, the charge data set points are less spread than the amplitude ones, meaning that we are less sensitive to cable length variations when using the charge quantity.

This work achieved, we want to verify if no cable was damaged after installation. Reflectometry also aimed at checking cable conditions by performing waveform shape analysis on secondary pulses.

6.1.4 Pulse shape analysis

In Fig. 6.3 is displayed an example of *normal* pulse, which corresponds to the case represented in Fig. 6.1a. In this case, the pulse sent in the cable travels to the PMT, and goes back to the acquisition after reflection on the divider.

6.1.5 Comparison with ^{60}Co

6.1.6 Conclusion

A faire : regarder le rising time en fonction de la longueur du cable
Regarder la différence de temps de montée du signal sur deux PMs très éloignés

6.2 Calibrating the electronic boards

6.2.1 Principle

6.2.2 Measuring the time offset of front end boards

6.2.3 Results

6.3 Energy calibration of optical modules

thèse Arnaud page 103

As described in Sec. 5.2.2, the collected charge at PM voltage divider is proportional to the amount of incident photoelectrons, and then to the initially deposited energy inside the scintillator. Once optical modules were assembled (optical coupling, packing, shielding integration), they were individually tested at Bordeaux laboratory, CENBG, with an electron spectrometer [ref]. Their energy resolutions for 1 MeV-electrons at the centre of scintillator front face were determined. High voltages were set to optimal values, to obtain an amplitude of 300 mV for 1 MeV electrons. However, after calorimeter integration, due to different environment, amplitude spectra of each optical block have to be re-aligned. This work was performed by Axel Pin, PhD student at CENBG. We give in this section a summary of this energy calibration study.

*A finir

6.4 Baseline studies

6.5 Light Injection System

Conclusion

Bibliography

[1] M. Agostini et al. Probing majorana neutrinos with double-β decay. *Science 365*, 1445, 2019.

[2] S.I. Alvis et al. Search for neutrinoless double-beta decay in ^{76}ge with 26 kg-yr of exposure from the majorana demonstrator. *Phys. Rev. C*, 100, 2019.

[3] O. Azzolini et al. First result on the neutrinoless double-β decay of ^{82}Se with cupid-0. *Phys. Rev. Lett.*, 120:232502, Jun 2018.

[4] C. Alduino et al. First results from cuore: A search for lepton number violation via $0\nu\beta\beta$ decay of ^{130}Te. *Phys. Rev. Lett.*, 120:132501, Mar 2018.

[5] J. B. Albert et al. Search for neutrinoless double-beta decay with the upgraded exo-200 detector. *Phys. Rev. Lett.*, 120:072701, Feb 2018.

[6] A. Gando et al. Search for majorana neutrinos near the inverted mass hierarchy region with kamland-zen. *Phys. Rev. Lett.*, 117:082503, Aug 2016.

[7] Nucleid database.

[8] R. Arnold et al. Probing new physics models of neutrinoless double beta decay with supernemo. *Eur. Phys. J. C*, 2010.

[9] S. Clavez. *Development of reconstruction tools and sensitivity of the SuperNEMO demonstrator*. PhD thesis, Université Paris Sud, 2017.

[10] Garrido X. Bongrand M. Hamamatsu 8" pmt test in magnetic shield. Internal presentation, 2014.

[11] Gomez-Cadenas et al. Physics case of supernemo with ^{82}se source. Internal presentation, 2008.

[12] R. Arnold et al. Final results on ^{82}se double beta decay to the ground state of ^{82}kr from the nemo-3 experiment. *Eur. Phys. J. C*, 2018.

[13] Tretyak V.I. Ponkratenko O.A. and Zdesenko Yu.G. The event generator decay4 for simulation of doublebeta processes and decay of radioactive nuclei. *Phys. At. Nucl.*, 63:1282–1287, Jul 2000.

[14] R. Arnold et al. Results of the search for neutrinoless double-β decay in ^{100}mo with the nemo-3 experiment. *Phys. Rev. D*, 2015.

[15] Perrot F. Radiopurity measurements for 8" pmts and preliminary budget for the sn demonstrator. Internal presentation, 2017.

[16] Cousins D. Feldman G. A unified approach to the classical statistical analysis of small signals. *Phys.Rev.*, pages 3873–3889, 1999.

[17] J. Kotila and F. Iachello. Phase-space factors for double-β decay. *Phys. Rev. C*, 85:034316, Mar 2012.

[18] J. Menéndez et al. Disassembling the nuclear matrix elements of the neutrinoless $\beta\beta$ decay. *Nuclear Physics A*, 818(3):139 – 151, 2009.

[19] Y. Iwata et al. Large-scale shell-model analysis of the neutrinoless $\beta\beta$ decay of ^{48}Ca. *Phys. Rev. Lett.*, 116:112502, Mar 2016.

[20] J. Barea, J. Kotila, and F. Iachello. $0\nu\beta\beta$ and $2\nu\beta\beta$ nuclear matrix elements in the interacting boson model with isospin restoration. *Phys. Rev. C*, 91:034304, Mar 2015.

[21] J. Hyvärinen and J. Suhonen. Nuclear matrix elements for $0\nu\beta\beta$ decays with light or heavy majorana-neutrino exchange. *Phys. Rev. C*, 91:024613, Feb 2015.

[22] F. Šimkovic et al. $0\nu\beta\beta$ and $2\nu\beta\beta$ nuclear matrix elements, quasiparticle random-phase approximation, and isospin symmetry restoration. *Phys. Rev. C*, 87:045501, Apr 2013.

[23] Tomás R. Egido J. Luis Vaquero López N., Rodríguez. Shape and pairing fluctuation effects on neutrinoless double beta decay nuclear matrix elements. *Phys. Rev. Lett.*, 111:142501, Sep 2013.

[24] J. M. Yao, L. S. Song, K. Hagino, P. Ring, and J. Meng. Systematic study of nuclear matrix elements in neutrinoless double-β decay with a beyond-mean-field covariant density functional theory. *Phys. Rev. C*, 91:024316, Feb 2015.

[25] P. K. Rath, R. Chandra, K. Chaturvedi, P. K. Raina, and J. G. Hirsch. Uncertainties in nuclear transition matrix elements for neutrinoless $\beta\beta$ decay within the projected-hartree-fock-bogoliubov model. *Phys. Rev. C*, 82:064310, Dec 2010.

[26] Dong-Liang Fang, Amand Faessler, Vadim Rodin, and Fedor Šimkovic. Neutrinoless double-β decay of deformed nuclei within quasiparticle random-phase approximation with a realistic interaction. *Phys. Rev. C*, 83:034320, Mar 2011.

[27] Loaiza P. Source foils measurement with bipo. Internal presentation, 2017.

[28] Xin Ran Liu. Radon mitigation strategy and results for the supernemo experiment. IoP APP / HEPP Conference, 2018.

[29] A. Chapon. *Mesure des processus de double désintégration bêta du Mo vers l'état excité 0_1^+ du Ru dans l'expérience Nemo3, Programme de R&D SuperNEMO : mise au point d'un détecteur BiPo pour la mesure de très faibles contaminations de feuilles sources.* PhD thesis, Université Caen Basse-Normandie, 2011.

[30] Snow S. A magnetic field map for the tracker. Internal presentation, 2015.

[31] A. Pin. *Recherche de la nature du neutrino via la décroissance double bêta sans émission de neutrinos. Caractérisation et optimisation du calorimètre SuperNEMO et impact sur la recherche de la décroissance du 82Se Développement du premier prototype LiquidO.* PhD thesis, Université Bordeaux-Gradignan, 2020.

[32] A. H. Wapstra G. Audi. The 1995 update to the atomic mass evaluation. *Nucl. Phys. A*, 595:409–480, feb 1995.

[33] Dassié D. et al. Two-neutrino double-β decay measurement of ^{100}Mo. *Phys. Rev. D*, 51:2090–2100, Mar 1995.

[34] R. Arnold et al. Measurement of the $2\nu\beta\beta$ decay half-life of ^{150}nd and a search for $0\nu\beta\beta$ decay processes with the full exposure from the nemo-3 detector. *Phys. Rev. D*, 94, oct 2016.